UNIVERSITY OF OKLAHOMA

GRADUATE COLLEGE

SPECTRUM FORMATION AT LATE TIMES IN TYPE Ia SUPERNOVAE

A DISSERTATION

SUBMITTED TO THE GRADUATE FACULTY

in partial fulfillment of the requirements for the

Degree of

DOCTOR OF PHILOSOPHY

By

BRIAN CHRISTOPHER FRIESEN
Norman, Oklahoma
2015

SPECTRUM FORMATION AT LATE TIMES IN TYPE Ia SUPERNOVAE

A DISSERTATION APPROVED FOR THE
HOMER L. DODGE DEPARTMENT OF PHYSICS AND ASTRONOMY

BY

Dr. Edward Baron, Chair

Dr. Mukremin Kilic

Dr. Ronald Kantowski

Dr. Xinyu Dai

Dr. Richard Henry

Dr. Trina Hope

To Mom and Dad.

Acknowledgements

Many people have been integral to my success as a graduate student, to whom I am grateful:

Locals: To Eddie, for showing me not only how to do good science, but how to be a good scientist. To David, for helping me write my first paper. To my many office mates over the years, who have made our crowded offices fun places to work. To Roseanna, for the knitted change basket, the cookbooks, and all the food.

Others: To Jerod, for being a great friend, collaborator, and confidant. To Peter, for hosting me at the Hamburger Sternwarte, and for all the beer and apple juice. And to Rollin, for always challenging me to do better.

Table of Contents

List of Tables

List of Figures

Abstract

I present a study of radiative transfer effects in type Ia supernovae ranging from 3-4 months to nearly 2 years post-maximum light. I explore several components of spectrum formation, beginning with a semi-analytic model which examines the behavior of line scattering in an optically thin medium, reminiscent of SN Ia ejecta at late times, and compare such behavior with the effects of line scattering at early times in SNe Ia, when the ejecta are optically thick. The model shows that line scattering produces spectral features similar to P Cygni profiles found near maximum light in SNe, but with subtle wavelength shifts which may lead to misidentified lines in observed spectra if these effects are not taken into account. Next, I present near-infrared synthetic spectra from numerical calculations with the general-purpose radiative transfer code `PHOENIX`, and compare them to observations obtained of four normal type Ia supernovae several months post-maximum light, including the recent and nearby SN 2014J. Such comparisons reveal that, even this late in a supernova's life, permitted lines of iron-peak elements comprise most of the near-infrared spectrum. In addition, an emission feature from [Ni II] near 2 µm indicates that electron-capture during high-density nuclear burning likely takes place in a significant fraction of type Ia supernovae. Such high-density burning is difficult to obtain in explosions of sub-Chandarsekhar-mass progenitors, e.g., white dwarf mergers. Finally I perform spectrum calculations at even later

epochs, from 100 to 578 days after maximum light, and compare the results to the observed optical and ultraviolet spectra of the nearby SN 2011fe. I find that, contrary to much of the literature, our models fit SN 2011fe at day +100 without accounting for any forbidden atomic lines; the optical spectrum consists primarily of permitted Fe II and Ca II. Including forbidden lines and repeating the same calculation yields similar optical spectra, but with quite different atomic lines contributing to most of the features, leading to a curious degeneracy among interpretations of spectra at this epoch. At later epochs, forbidden emission from Fe II and Fe III form most of the optical spectrum, although the H & K doublet of Ca II continues to play a role in the emission near 4000 Å. In the ultraviolet spectrum at day +360, the SED is optically thick, and most of the spectrum consists of permitted lines of various iron-peak species. These results show that the transition to the "nebular" phase in type Ia supernovae is more complicated than frequently assumed in the literature, and is highly wavelength-dependent.

Chapter 1

Overview of type Ia supernovae

Type Ia supernovae (SNe Ia) are among the brightest and most energetic transient events in the observable universe, reaching typical magnitudes of $M_V \simeq -19.1$ (e.g., Hamuy, Phillips, et al. 1996). In addition, their spectral energy distributions (SEDs) are remarkably homogeneous over a broad range of wavelengths. These two properties render SNe Ia ideal "standard candles" for precision cosmology. The High-z Supernova Search Team (Riess et al. 1998) and the Supernova Cosmology Project (Perlmutter et al. 1999) leveraged this feature to measure the cosmological constant Λ, whose non-zero value indicates that the expansion of the Universe is accelerating.[1]

Despite their utility as cosmological distance indicators, a discomforting degree of mystery enshrouds quantitative SN Ia science, in that no progenitor system has been directly detected (Branch, Livio, et al. 1995; Pritchet et al. 2008). It is generally believed that a SN Ia is the explosive death of a carbon-oxygen (C/O) white dwarf (WD) near the Chandrasekhar mass limit $M_{\rm Ch} \simeq 1.4\ M_\odot$ (Shu 1982). How the WD acquires so much mass remains unknown, and as a result, several theories have been proposed to explain this process. One explanation is that the WD accretes matter, presumably hydrogen, from a non-degenerate companion

[1]For this discovery, Adam Riess, Brian Schmidt, and Saul Perlmutter were awarded the Nobel Prize in Physics in 2011 (*The Nobel Prize in Physics 2011* 2013).

star, which burns stably to C/O on the WD surface (Whelan and Iben 1973). Another is that two co-orbiting WDs in a binary system lose angular momentum via gravitational wave emission, and eventually merge (Iben and Tutukov 1984; Webbink 1984). Other scenarios involve violent WD mergers (Pakmor et al. 2012), detonations of a thin layer of accreted helium which in turn detonates the central carbon ("double-detonation;" Woosley and Weaver 1994; Woosley and Kasen 2011; Shen and Bildsten 2014), the merger of a WD with the hot, exposed core of an AGB star ("core-degenerate;" Soker 2013), and more exotic scenarios such as a magnetic field which funnels material from a main-sequence star onto its highly magnetized WD companion ("magnetic bottle;" Wheeler 2012). Recently, Chiosi et al. (2014) even proposed a scenario in which an *isolated* WD could explode via pycnonuclear reactions. Furthermore, some theories for SN Ia explosions do not even agree that the 1.4 $M_\odot$ mass of a WD is necessary (van Kerkwijk et al. 2010).

Although the radiative properties of SNe Ia are uniform enough to show that $\Lambda \neq 0$, they nevertheless exhibit some diversity which precludes a precise measurement of the dark energy equation of state parameter $\omega \equiv P/\rho$, since the Hubble constant H_0 varies weakly with w (Frieman et al. 2008). Fortunately, some of this diversity is correlated, thanks to a likely common physical origin, and therefore the errors in measurements of the absolute magnitudes of SNe Ia can be reduced considerably. The first-order correlation is between the absolute brightness of a SN Ia and its so-called Δm_{15} value, or the amount by which it dims in the Johnson-Cousins photometric band B (Bessell 1990) between maximum light and 15 days layer (Phillips 1993; Phillips, Lira, et al. 1999). Neglecting this

correction, the 1σ uncertainty in optical photometric bands is ~ 0.4 mag (Branch and Tammann 1992); applying the correction reduces the scatter to $\lesssim 0.2$ mag (Hamuy, Phillips, et al. 1996).

There may be second-order correlations in addition to the brightness-decline relation which, if identified, could allow the uncertainty in SN brightness (and therefore distance) measurements to be reduced further. For example, variations in the C/O mass distribution in the WD or the central density ρ_c of the WD prior to explosion, both functions of the progenitor star while on the main sequence, could lead to systematic variations in SN light curves and spectra (Höflich, Krisciunas, et al. 2010; Krueger, Jackson, Townsley, et al. 2010; Seitenzahl, Ciaraldi-Schoolmann, et al. 2011; Krueger, Jackson, Calder, et al. 2012; Ohlmann et al. 2014). Another possible source of variation in peak brightness is the degree of primordial metallicity in the progenitor WD (Timmes, Brown, et al. 2003).

While the photometric dispersion of SNe Ia in optical bands can be reduced to 0.2 mag by correcting for various correlated variations, in the near-infrared (NIR) bands the dispersion is already this low after applying corrections only for extinction (Krisciunas et al. 2004; Phillips, Garnavich, et al. 2006; Wood-Vasey et al. 2008; Y. Wang 2010). SNe Ia are therefore often described as being "standard*izable* candles" in the optical, but very nearly "*standard* candles" in the NIR. Furthermore, extinction and reddening due to dust along the line of sight to the SN, which conspire with the intrinsic SN diversity to introduce further uncertainties in measurements of SN absolute magnitudes, are almost non-existent in the NIR (Cardelli et al. 1989). In addition, Mandel et al. (2011) showed that

photometric information such as $M_{B,\max}$ and Δm_{15} tends to be highly correlated in optical filters, but weakly correlated in the NIR: the "information density" is higher in the NIR than in the optical. These factors, together with the dearth of NIR data in the literature, inspired the observations and modelling efforts we undertook with regard to SN 2014J (see Chapter 3). Indeed, the relatively recent proliferation of NIR instruments and observatories, especially the James Webb Space Telescope (Gardner et al. 2006), set to launch toward the end of this decade, should yield a rich harvest of new data and constraints on SNe Ia which have been inaccessible in the optical.

From measurements of SNe Ia at early times – before and near maximum light – one may constrain various properties in their outer layers, such as asymmetry and degrees of metallicity and mixing (Lentz et al. 2000; Kasen, Nugent, et al. 2003; Nugent, Sullivan, et al. 2011; Parrent, Howell, et al. 2012; Maund, Spyromilio, et al. 2013). However, measurements at later epochs – months and years after maximum light – provide nearly orthogonal constraints by probing the innermost regions of the ejecta (Kozma, Fransson, et al. 2005; Leloudas et al. 2009; Maeda, Leloudas, et al. 2011; Mazzali, Maurer, et al. 2011; Mazzali and Hachinger 2012). Deriving characteristics of the inner regions of SNe Ia is critical for validating explosion models of SNe Ia, since many find (or assume) that the explosion begins at or near the center of the WD (Nomoto et al. 1984; Nonaka et al. 2012; Malone et al. 2014). It is to this end that we have performed analytic calculations of radiative transfer processes in SNe (Chapter 2), as well as numerical simulations (Chapter 3 and Chapter 4) with the radiative transfer code `PHOENIX`. Translating

results from radiative transfer calculations into physical constraints requires a deep understanding of the processes which drive spectrum formation in SNe. In Chapter D we explore other applications of the PHOENIX code, as well as some novel numerical methods for solving the radiative transfer equation.

1.1 Physics of spectrum formation in SNe

A number of physical processes compete and collude to generate the SED of a SN Ia. Their relative influence varies wildly with the age of the SN, leading to considerable variation in the shape of the SED over time, and to difficulty in disentangling the information contained therein. In the following sections we outline the most important of these processes.

1.1.1 Non-thermal processes

The thermonuclear fusion of the C/O in a WD during its disruption releases more than enough energy to unbind it ($\sim 10^{51}$ erg), and one might intuit that the excess energy from this fusion process would be the source of SN Ia luminosity. This is not the case, however, because the nuclear energy released in the explosion is spent performing the work necessary for the adiabatic expansion of the WD long before any of it can be emitted as radiation (Colgate and McKee 1969). The source of SN Ia luminosity must then lie elsewhere. The exponential decline of SN Ia light curves after maximum light suggests radioactive decay as the energy source, and Burbidge et al. (1957) suggested radioactive ^{254}Cf as the source. However, cosmological abundances of this isotope are much too low to support

this hypothesis; instead, it is now widely believed that ^{56}Ni is the source (Hoyle and Fowler 1960; Truran et al. 1967). ^{56}Ni decays to radioactive ^{56}Co and finally to stable ^{56}Fe. After a half-century, the first direct evidence to support this theory has emerged, in the form of the detection of ^{56}Co γ-ray lines in the nearby SN 2014J (Churazov, Sunyaev, Isern, Knödlseder, et al. 2014).

Analyses of SN Ia light curves indicate that several 0.1 $M_{\odot}$ of ^{56}Ni are produced during the explosion of a WD (e.g., Arnett 1982; A. Khokhlov et al. 1993; Woosley, Kasen, et al. 2007). The ^{56}Ni, a radioactive isotope with a half-life of ~ 6 d, and its daughter nucleus ^{56}Co with a half-life of 77 d, power SNe Ia luminosity through the thermalization of γ-rays and positrons produced during nuclear decay. The transport properties of these two decay products are quite different, especially at late times in SNe Ia. A γ-ray born from a decaying ^{56}Ni or ^{56}Co nucleus has a typical energy of ~ 1 MeV, and undergoes Compton scattering with both free and bound electrons in the ejecta, imparting roughly half of its energy to the incident electron during each scattering event (Chan and Lingenfelter 1991).[2]

The behavior of positrons is more complicated than that of γ-rays, due primarily to their interaction with magnetic fields. It is known that positrons, once emitted, will deposit their energy in the gas either kinetically or through annihilation with electrons to produce two 511 keV γ-rays (Axelrod 1980; Chan and Lingenfelter 1993). However, the distance a positron travels before interacting with the gas remains a mystery because the magnetic field structure of the exploding WD is

[2]The optical depth to γ-rays is relatively small even at early epochs in a SN Ia, and many escape without having thermalized in the SN ejecta; in principle, then, one can measure the spectra and light curves of SNe in MeV bands to determine properties of, e.g., the asphericity of the explosion (Höflich et al. 1992, 1994; Höflich, Wheeler, et al. 1998; Höflich 2002).

largely unknown. One argument is that even a weak magnetic field with a modest amount of "turbulence" will lead to a positron cyclotron radius which is orders of magnitude smaller than the radius of the WD; consequently one can assume that positrons deposit their energy (or produce two γ-rays) at the same point where they are first emitted (Colgate and McKee 1969; Axelrod 1980). However, another possibility is that the magnetic field, if present, will be radially "combed", in which case positrons will follow the field lines and have a mean free path which is comparable to or even larger than the WD radius (Colgate, Petschek, et al. 1980). Work on the problem of positron transport in SNe Ia is sparse, although recent work has introduced methods for constraining the nature of the magnetic field (Diamond et al. 2014; Penney and Höflich 2014). Overall the nature and influence of the magnetic field in SN Ia progenitor and explosion scenarios remains a largely unsolved problem.

The lives of both γ-rays and positrons end the same way: they both impart their energy to electrons in the SN ejecta. Prior to $\sim$ 150 d, γ-rays dominate the energy deposition; after this time the optical depth to γ-rays becomes low and most escape the SN ejecta, at which point positrons become the dominant energy source (Höflich et al. 1994; Telesco et al. 2014). The first electron with which a γ-ray or positron interacts is called a "primary" electron and receives several 0.1 MeV of energy during the interaction; it then collides with more electrons ("secondary," "tertiary," etc.), transferring a fraction of its energy with each collision. After a few collisions a high-energy electron thermalizes and its energy is described by a Maxwellian distribution.

1.1.2 Thomson scattering

At early times in supernovae of all types, the primary opacity source at most wavelengths is Thomson scattering from free electrons (Höflich, Wehrse, et al. 1986; Höflich, Mueller, et al. 1993). Thus, while the scattering optical depth to the center of the ejecta is large,

$$\int_R^0 dr\sigma(r) \gg 1 \tag{1.1}$$

the *true absorption* optical depth remains small:

$$\int_R^0 dr\kappa_\lambda(r) < 1. \tag{1.2}$$

The hegemony of Thomson scattering over true absorption in supernova atmospheres leads to curious radiative phenomena. For example, the "Balmer jump" at 3464 Å (Carroll and Ostlie 2007) is absent in spectra of type II supernovae (SNe II), despite the copious amount of neutral hydrogen in the ejecta (Shaviv et al. 1985). In SNe Ia, Thomson scattering produces the "spectrum" (H_λ) in the deepest layers of the ejecta, but despite the high optical depths ($\tau \gtrsim 3$), H_λ remains distinctly non-blackbody-like. The reason for this is that, because the opacity is dominated by scattering, even at large optical depth the radiation field remains stubbornly decoupled from the gas, i.e., $S(\tau \gg 1) \neq B$. At higher velocities in SNe Ia near maximum light, the relative strengths of scattering and line optical depths are highly wavelength-dependent; generally in the UV, strong

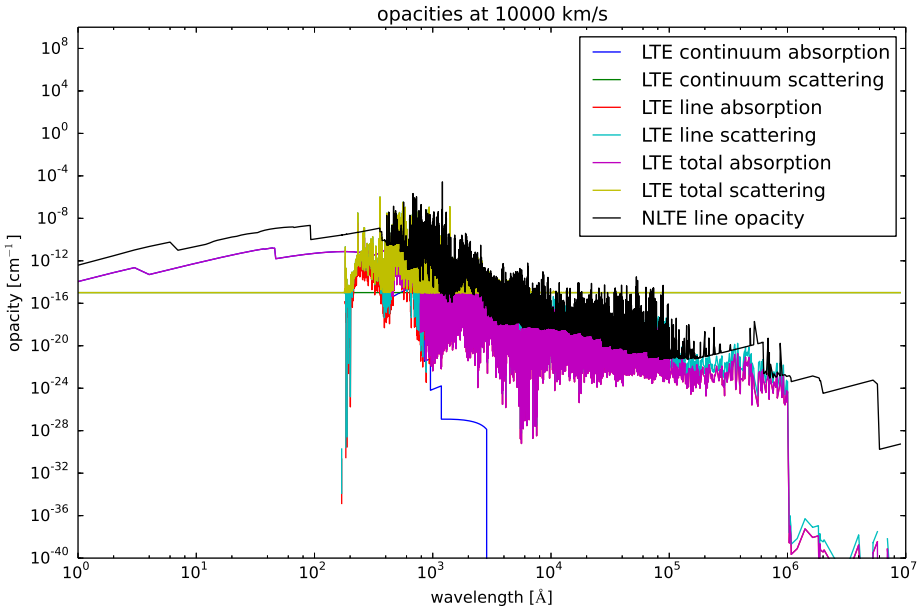

Figure 1.1: Various opacities measured at 10 000 km s^{-1} as a function of wavelength in a `PHOENIX` calculation of a DD explosion model at day 18. This velocity corresponds roughly to the location of the photosphere at maximum light in SNe Ia. The corresponding synthetic spectrum is shown in Figure 1.2.

resonance lines dominate the opacity, but in much of the optical and NIR, Thomson scattering continues to be the largest opacity source. Figure 1.1 illustrates the competition among the various types of opacity near maximum light in a standard delayed-detonation (DD) explosion model. The corresponding synthetic spectrum, compared to SN 2011fe at roughly maximum light, is shown in Figure 1.2.

Because the Thomson opacity scales with the free electron density n_e, it decreases roughly in proportion to the geometric dilution of the gas: $n_e \propto \rho \propto t^{-3}$ (ionization changes notwithstanding). Consequently, after maximum light, line absorption overtakes Thomson scattering as the dominant opacity in supernova atmospheres. The continuum (or psuedo-continuum; see Section 1.1.5) fades over

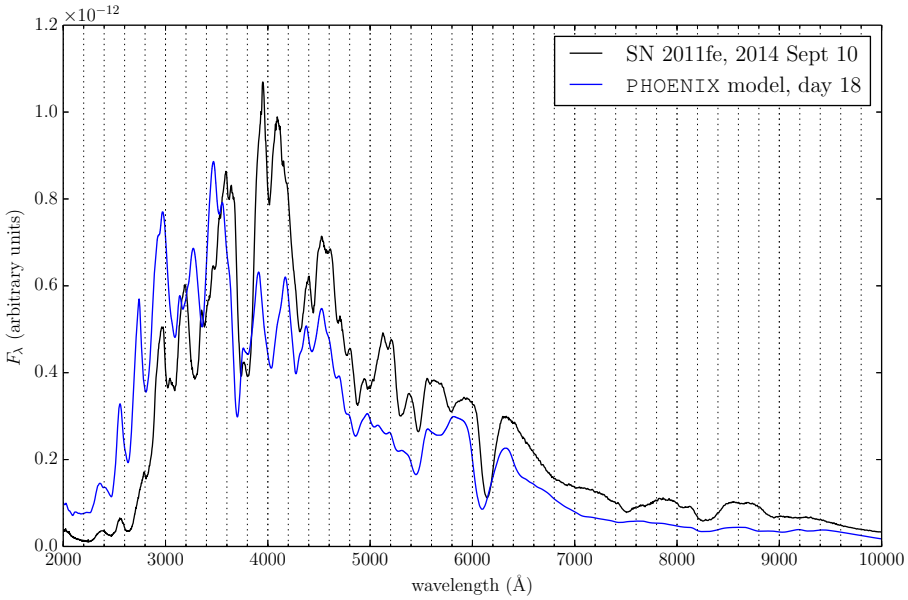

Figure 1.2: PHOENIX synthetic spectrum at 18 days post-explosion compared to SN 2011fe at maximum light. The opacities in this model are shown in Figure 1.1. The observed spectrum was obtained from WISeREP (Yaron and Gal-Yam 2012).

time, eventually resulting in a spectrum consisting almost exclusively of lines (see, e.g., the spectroscopic time series of SN 2011fe, Pereira et al. 2013).

1.1.3 Permitted lines

The early spectra of SNe Ia consist almost entirely of broad and blended P Cygni profiles arising from absorption and re-emission of strong permitted lines ("line scattering") of a variety of atomic species, in the homologously expanding ejecta (Filippenko 1997; Branch, Baron, et al. 2005; Parrent, Friesen, et al. 2014). Unlike forbidden lines (see Section 1.1.4), line scattering at a microphysical level does not affect the thermal pool of the SN ejecta, since it only redirects photons. However, the *global* effects of line scattering can affect the temperature structure profoundly

by coupling distant regions together (Mihalas 1978). An isolated P Cygni profile consists of an emission peak centered at the rest wavelength of the line, and a blueshifted absorption trough, the minimum of which which one can use to trace the location of the photosphere of the SN (Jeffery and Branch 1990). However, the high characteristic velocities of line-forming regions in the ejecta ($\sim 10\,000$ km s^{-1}) and the enormous number of strong permitted lines of intermediate-mass and iron-peak elements render quantitative analysis of SN Ia spectra difficult (Baron, Hauschildt, Nugent, et al. 1996).

It is generally assumed that permitted lines cease line scattering as the SN ages, and that eventually all emission peaks in a SN spectrum are formed through emission of collisionally excited forbidden lines (Kirshner and Oke 1975). However, it is possible to obtain good fits to relatively old SN Ia spectra assuming that line scattering remains the dominant radiative transfer process (see Section 1.1.4). Many studies of late-time spectra of SNe Ia assume that features are optically thin emission lines, and they thus infer from the apparent Doppler shifts of such features the asymmetric bulk motion of the inner regions of SNe (e.g., Maeda, Benetti, et al. 2010). However, if permitted lines continue to play a role in spectrum formation at late times then these interpretations may not be correct, as it is possible for permitted scattering lines to exhibit wavelength shifts as well, even in spherically symmetric distributions (see Chapter 2 and Friesen, Baron, Branch, et al. 2012).

1.1.4 Forbidden lines

The role of collisionally excited emission lines ("forbidden lines") in SN Ia spectrum formation is not clear, and in fact has driven the majority of the work presented in this thesis. Kirshner and Oke (1975) presented one of the first identifications of forbidden lines in SN Ia optical spectra, focusing on SN 1972E several hundred days post-maximum light, and arguing that the lack of continuum emission deactivates the line scattering mechanism which produces the P Cygni features which characterize early SN Ia spectra (Branch, Baron, et al. 2005). Similarly, Axelrod (1980) found that spectra dominated by forbidden emission lines fit reasonably well to SN 1972E. On the other hand, Branch, Lacy, et al. (1983) obtained good fits to the optical spectra of SN 1981B (similar to SN 1972E) during the first 100 days post-explosion, assuming pure resonance-scattering on top of a blackbody continuum. Several following studies identified optical and NIR features at moderately late times as forbidden emission (Ruiz-Lapuente and Lucy 1992; Bowers et al. 1997; Mazzali, Maurer, et al. 2011; Mazzali and Hachinger 2012; Churazov, Sunyaev, Isern, Bikmaev, et al. 2015). Dessart, Hillier, et al. (2014) explored the cooling effects of forbidden lines in SNe Ia: a forbidden line photon almost always escapes the ejecta without being reabsorbed, thereby removing energy from the thermal pool. They argued that [Co III] is present even as early as maximum light in SN Ia spectra, and that it affects the ejecta temperature profoundly, even at early epochs. Others, however, continued to identify many of the same features as permitted resonance-scattering lines (Branch, Baron, et al.

2005; Jha et al. 2006; Branch, Jeffery, et al. 2008).

In Friesen, Baron, Branch, et al. (2012) (see also Chapter 2) we approached this problem from a different direction, performing analytic calculations of a simple radiative transfer model of resonance-scattering lines embedded in optically thin continuum emission. The impetus for this work was to discover how scattering lines manifest in spectra at late times in SNe Ia (assuming they are indeed active). We followed this work with detailed calculations using the `PHOENIX/1D` code in order to identify features at late times in both optical and UV spectra of SN 2011fe (see Chapter 4). In addition, we tentatively identified an emission feature at 1.98 microm as the 1.939 µm forbidden line of [Ni II] in four core-normal SNe Ia at several months post-maximum light.

1.1.5 Fluorescence

Fluorescence plays an influential role during a wide range of a SN Ia's lifetime. At early times it obscures the underlying Thomson scattering continuum by shifting the flux redward, producing a psuedo-continuum which has an apparent blackbody temperature significantly cooler than the physical temperature of the gas (Bongard et al. 2008). In the UV, metal-rich regions of the ejecta undergo *reverse* fluorescence in order to produce many spectral features in that region (Lentz et al. 2000; Mazzali 2000; Sauer et al. 2008).

At later times, fluorescence also drives spectrum formation in the NIR. For example, Gall et al. (2012) found that their synthetic spectrum fits in the NIR to the core-normal SN 2005cf as late as day +42 were shaped primarily by fluorescence

of iron-peak elements. In Friesen, Baron, Wisniewski, et al. (2014) we found a similar result, identifying nearly all NIR features in spectra of four core-normal SNe Ia with high-excitation lines of Fe II and Co II (see also Chapter 3). It is likely that this process is in turn driven by recombination from Fe III and Co III, since the upper levels of most NIR lines of iron-peak elements are too energetic to excite by collisions with thermal electrons.

1.2 Numerical methods for radiative transfer calculations in supernovae

We performed all numerical calculations presented in this thesis with the `PHOENIX` code. `PHOENIX` is a multi-purpose radiative transfer code which has been applied to a variety of astrophysical environments, including both core-collapse supernovae (Baron, Hauschildt, Branch, Wagner, et al. 1993; Baron, Hauschildt, and Branch 1994; Hauschildt and Ensman 1994; Baron, Hauschildt, Branch, Austin, et al. 1995; Baron, Hauschildt, Branch, Kirshner, et al. 1996) and thermonuclear supernovae (Nugent, Baron, Hauschildt, et al. 1995; Nugent, Phillips, et al. 1995; Baron, Hauschildt, Nugent, et al. 1996; Nugent, Baron, Branch, et al. 1997), novae (Hauschildt, Starrfield, Austin, et al. 1994; Beck et al. 1995; Hauschildt, Starrfield, Shore, et al. 1995; Hauschildt, Baron, et al. 1996; Schwarz et al. 1997), cool stars (Allard, Hauschildt, Miller, et al. 1994; Allard and Hauschildt 1995; Jones, Longmore, Allard, Hauschildt, et al. 1995; Allard, Hauschildt, Baraffe, et al. 1996; Jones, Longmore, Allard, and Hauschildt 1996; Leggett et al. 1996; Schweitzer

et al. 1996; Alexander et al. 1997; Allard, Hauschildt, Alexander, et al. 1997; Baraffe, Chabrier, Allard, et al. 1997; Hauschildt, Allard, et al. 1997), quasars (Stoerzer et al. 1994), and planets (Baraffe, Chabrier, Barman, et al. 2003). It solves the radiative transfer equation under a variety of circumstances, including 1-D and 3-D; Cartesian, cylindrical, and spherical geometries; and flows which are static, monotonic, non-monotic, relativistic, or contain shocks (e.g., Buchholz et al. 1994; Chen, Kantowski, et al. 2007). It also takes into account the effects of non-local thermodynamic equilibrium (NLTE) (Hauschildt 1993; Hauschildt and Baron 2014). Recent work has incorporated explicit time-dependence in the NLTE rate equations (De et al. 2010a,b), as well as in the radiative transfer equation itself (Jack et al. 2009, 2011, 2012a,b, 2013).

1.2.1 Non-thermal physics

One way to simulate directly the transport of γ-rays and to follow this energy deposition is to use Monte Carlo methods (Ambwani and Sutherland 1988). This framework lends itself naturally to radiative transfer phenomena which undergo highly anisotropic scattering events (such as Compton scattering), since photon interactions are calculated in the scattering frame. A second method exploits the relationship between the scattering angle and the amount of energy transferred during the scattering event (Weinberg 1995), rendering it more amenable to formal, grid-based radiative transfer methods. Descriptions of this scheme are in Sutherland and Wheeler (1984), Young et al. (1993), Young (1994), Swartz et al. (1995), Young et al. (1995), and Nugent, Baron, Branch, et al. (1997). In order to

test the accuracy of the latter method, which is used by default in PHOENIX/1D, we wrote a code which simulates γ-ray transport using the Monte Carlo method of Ambwani and Sutherland (1988). We found both formalism yield similar results and give rise to almost identical synthetic spectra.

Besides the transport of non-thermal particles and photons, one must also follow the energy cascade upon interaction with a thermal particle in the gas. The most sophisticated calculations of this transfer of energy follow the cascade of only the primary and secondary electrons (Xu and McCray 1991; Kozma and Fransson 1992). Such calculations also determine the fractions of non-thermal electrons which ionize, excite, and heat the gas. The non-thermal ionization rates can be estimated with the convenient semi-empirical fits provided by Lotz (1967), although no such fits exist currently for non-thermal excitation and heating rates. However, its effects are likely more influential in SNe II than in SNe Ia, since in SN II environments have a large mass of H and He, whose first excited states have energies of 10.1 eV and 19.8 eV, respectively, far out of range for excitation by collisions with thermal electrons (Kozma and Fransson 1992; C. Li et al. 2012). In addition, electron-impact excitation rates are subject to large uncertainties (Kozma and Fransson 1992), rendering suspect the purported advantage of including this piece of "extra physics".

1.2.2 The radiative transfer equation

For the work presented here, we used PHOENIX exclusively in its 1-D, spherically symmetric, time-independent mode. Under these conditions the radiative transfer

equation (RTE) can be written in the "mixed frame" coordinates of Mihalas (1980), where space-time variables are measured in the Eulerian (laboratory) frame, while gas and radiation quantities are measured in the Lagrangian (co-moving) frame. This unusual choice of coordinates allows one to capture relativistic effects to all orders in $\mathcal{O}(v/c)$, and also simplifies the RTE considerably when the radiative sources and sinks are isotropic. The time-independent RTE in the mixed frame is then (Hauschildt 1992a)

$$a_r \frac{\partial I_\lambda}{\partial r} + a_\mu \frac{\partial I_\lambda}{\partial \mu} + a_\lambda \frac{\partial \lambda I_\lambda}{\partial \lambda} + 4 a_\lambda I_\lambda = \eta_\lambda - \chi_\lambda I_\lambda \tag{1.3}$$

where

$$a_r \equiv \gamma(\mu + \beta) \tag{1.4}$$

$$a_\mu = \gamma(1-\mu^2)\left[\frac{1+\beta\mu}{r} - \gamma^2(\mu+\beta)\frac{\partial \beta}{\partial r}\right] \tag{1.5}$$

$$a_\lambda = \gamma\left[\frac{\beta(1-\mu^2)}{r} + \gamma^2\mu(\mu+\beta)\frac{\partial \beta}{\partial r}\right] \tag{1.6}$$

$$\tag{1.7}$$

where $\mu \equiv \cos\Theta$ is the direction cosine of the photon, $\beta \equiv v/c$ and $\gamma \equiv (1-\beta^2)^{-1/2}$.

The difficulty in solving Equation (1.3) for $I_\lambda(r,\mu)$, besides the already high dimensionality, is that η_λ and χ_λ are functions of integrals of I_λ, rendering the entire equation an integro-partial differential equation. `PHOENIX` tames this complicated nature of Equation (1.3) using the "operator perturbation" scheme devised by Cannon (1973a,b) and developed further by Olson and Kunasz (1987),

Hauschildt (1992a), and Hauschildt and Baron (2006). In this scheme, all radiation field quantities are calculated along a series of rays which traverse the radiating medium. Along a given ray the transfer equation takes the form (Mihalas 1980; Hauschildt 1992a)

$$\frac{\partial I_\lambda}{\partial s} + a_\lambda \frac{\partial(\lambda I_\lambda)}{\partial \lambda} = \eta_\lambda - (\chi_\lambda + 4a_\lambda) I_\lambda \tag{1.8}$$

Each ray represents a beam of radiation travelling along a null geodesic, subtending a solid angle element $d\Omega$, and one constructs a sufficient number of such rays such that the entire medium is sufficiently sampled.[3] As long as one can establish a relationship between the coordinates along each ray and the coordinates of the hydrodynamical grid (a challenging task when the fluid velocities are relativistic; Mihalas 1980; Chen, Kantowski, et al. 2007; Baron, Hauschildt, and Chen 2009), one can apply the operator perturbation method to effectively any type of radiating flow.

To understand how and why operator perturbation works, one must first understand why the *un*perturbed operator in question, the so-called Λ-operator, does *not* work, at least in media with large optical depth. The Λ-operator is the matrix representation of the *formal solution* of the radiative transfer equation, which, given the source function S, takes the form

$$\frac{dI}{d\tau} = S - I \tag{1.9}$$

[3]In the calculations presented in this work, we used 128 rays to sample a representative hemisphere of a spherically symmetric hydrodynamical model.

where $d\tau \equiv \chi ds$ is the optical depth along the ray with path coordinate s. The formal solution gives the value of I at optical depth τ:

$$I(\tau) = I(0)e^{-\tau} + \int_0^\tau S(\tau')e^{-(\tau-\tau')}d\tau'. \tag{1.10}$$

However this step does not complete the solution to the problem of radiative transfer, because S at one point depends implicitly on I at *all* points. The evaluation of $S(\tau')$ in the formal solution is weighted by the factor $e^{-(\tau-\tau')}$, which is largest when $\tau' = \tau$, and decreases exponentially as $\tau - \tau'$ increases. Therefore, the formal solution provides $I(\tau)$ with significant information about $S(\tau)$ only within the range $\tau \pm 1$. One could in principle apply the formal solution repeatedly to get new $I(\tau)$, which one could then use to obtain new values for $S(\tau)$ and so on; this process is called Λ-iteration, and because each iteration transports information only about 1 mean free path, it converges exponentially slowly in media with $\tau \gg 1$ (Mihalas 1978).

Because in the formal solution $I(\tau)$ is linear in S, one can rewrite Equation (1.10) as a matrix operation:

$$I(\tau) = \Lambda[S(\tau)] \tag{1.11}$$

In this context, one can see that repeated use of the Λ-operator will converge slowly because the spectral radius of the Λ matrix is very close to 1 for large τ (Hauschildt and Baron 1999). One can accelerate convergence by splitting Λ

according to

$$\Lambda = \Lambda^* + (\Lambda - \Lambda^*) \tag{1.12}$$

In principle one can choose any value for Λ^* as it is both added and subtracted from Λ. However, only judicious choices lead to rapid convergence of the radiative transfer equation. Olson and Kunasz (1987) found that using elements of the actual Λ matrix yielded swift convergence. Specifically, they found that using only the diagonal of Λ led to a computationally cheap construction of Λ^* but required many iterations to converge (although far fewer than actual Λ-iteration); using more bands of Λ to fill in Λ^* required more expense, but required fewer iterations to converge. `PHOENIX` allows the user to choose an arbitrary "bandwidth" (number of diagonals) of the Λ^* operator (called the "approximate Λ operator or ALO") so that the user may find an optimum balance between speed in construction of Λ^* and the number of iterations to converge the radiative transfer equation.

1.2.3 The statistical equilibrium equations

The stability and speed of the operator perturbation algorithm for solving the equation of transfer inspired an analogous method for solving the NLTE rate

equations, which yield the populations of each atomic level n_i:

$$\begin{aligned}\frac{dn_i}{dt} &= \sum_{j<i} n_j(R_{ji} + C_{ji}) \\ &\quad - n_i \left\{ \sum_{j<i} \left(\frac{n_j}{n_i}\right)^* (R_{ij} + C_{ij}) + \sum_{j>i} R_{ij} + C_{ij} \right\} \\ &\quad + \sum_{j>i} n_j \left(\frac{n_i}{n_j}\right)^* (R_{ji} + C_{ji})\end{aligned} \tag{1.13}$$

where R_{ij} and C_{ij} are the radiative and collisional rates, respectively, from level $i \rightarrow j$, n_i is the LTE population of level i as defined by Mihalas (1978), n_κ is the NLTE population density of the ground state of the next higher ionization stage, and n_e is the NLTE free electron density. The NLTE rate equations are non-linear in the level populations n_i and are also "non-local" in the sense that the population of a particular level depends sensitively on the populations of all other levels through collisional and radiative transitions. Furthermore, they exhibit a circular dependence on the radiation field: the rates of atomic processes depend on the intensity I_λ (or J_λ for isotropic atomic processes), which in turn depends on those rates. To combat this mathematical formidability Rybicki and Hummer (1991) devised an "approximate rate operator" scheme (Rybicki and Hummer 1991, 1992, 1994) (which underwent further development by Hauschildt 1993; Hauschildt and Baron 2014) whose perturbation on the "true rate operator" accelerates convergence of the rate equations. However, given the circular dependence of the RTE and the rate equations, one often must converge each piece separately, and iterate between the two until simultaneous and global convergence of both is

achieved.

1.2.4 The equation of state

The rate equations determine the populations of atoms in each level of each ionization stage. However they do not determine the population of atoms in each ionization stage, and in fact require as input the results of such a calculation, specifically through the free electron density n_e. Calculation of n_e is relegated to the equation of state (EOS), which determines the rate of ionization and recombination of atoms (and molecules, if necessary), and determines n_e by charge conservation. The simplest example of a stellar EOS is the Saha equation, which is an extension of the Boltzmann equation to continuum states (Mihalas 1978). However, the Saha equation is by construction an LTE EOS, and is valid only in regimes where collisional rates dominate radiative rates. Given the rarefied nature of the ejecta in SNe Ia, this is rarely the case. Rather, one must calculate the ionization of the gas with a NLTE EOS, which generally proceeds by minimizing the Helmholtz free energy (see, e.g., W. Smith and Missen 1982; Hummer and Mihalas 1988; Timmes and Swesty 2000). `PHOENIX` captures NLTE effects in the EOS by modifying the partition function Z of each ion such that

$$Z \equiv \sum_i g_i \exp\left[-\frac{E_i}{k_B T}\right] \tag{1.14}$$

is generalized to

$$Z_{\mathrm{NLTE}} \equiv \sum_i b_i g_i \exp\left[-\frac{E_i}{k_B T}\right] \tag{1.15}$$

where $b_i \equiv n_i/n_i^*$ is the departure coefficient of level i as determined by the solution to the NLTE rate equations (Hauschildt and Baron 1999). The partial pressures of each ion are computed using the chemical equilibrium method of W. Smith and Missen (1982) (see also Husser et al. 2013). This is a more stable numerical approach than the "occupation probability" formalism developed by Hummer and Mihalas (1988), which consists of a high-dimensional linearization scheme. However, the introduction of b_i adds a circular dependence between the EOS and the rate equations, so they must be iterated back and forth to achieve global convergence.

1.2.5 Temperature calculation

Perhaps the most influential (and difficult) quantity to calculate in spectrum synthesis of supernovae is the gas temperature. The thermal energy of the gas is determined by following the complex interplay of microphysical processes which transfer energy between the gas and the radiation field. Tracing the energy transfer into and out of the gas is challenging because the temperature, being coupled to the highly non-local RTE, becomes itself an implicitly non-local quantity, i.e., the temperature at one point in the ejecta depends sensitively on the temperatures at all other points in the ejecta.

In principle, then, determining the temperature of a radiating gas requires a full radiation-hydrodynamical calculation (e.g., Castor 2007). Fortunately, however, we are afforded some luxury in the case of SN atmospheres, in that they are stable against convection, such that the energy in the ejecta is transported entirely

through radiation. This is the condition of *radiative equilibrium* (Mihalas 1978), and its validity in SN atmospheres has inspired the development of a variety of algorithms for calculating the gas temperature.

Historically `PHOENIX` has used the so-called Unsöld-Lucy scheme (Mihalas 1978; Hauschildt 1992b; Hauschildt and Baron 1999) to calculate the gas temperature. This scheme was first developed by Unsöld (1951, 1955) to enforce radiative equilibrium in grey atmosphere models. Recognizing that many types of stellar atmospheres exhibit large deviations from greyness, Lucy (1964) generalized it to the non-grey case by introducing wavelength-integrated, moment-weighted opacities which are insensitive to temperature and thus change little during temperature correction iterations. Hamann and Gräfener (2003) provide an excellent discussion of the development of this procedure, which we summarize briefly here:

In radiative equilibrium, a given parcel of gas neither creates nor destroys energy; all of the energy it absorbs is re-emitted, albeit not necessarily with the same energy distribution. The energy absorbed by a parcel of gas is

$$A(r) = \int_0^\infty d\lambda \oint d\Omega \chi_\lambda(r) I_\lambda(r) = 4\pi \int_0^\infty d\lambda \chi_\lambda(r) J_\lambda(r) \tag{1.16}$$

and the energy emitted is

$$E(r) = \int_0^\infty d\lambda \oint d\Omega \eta_\lambda(r) = 4\pi \int_0^\infty \chi_\lambda(r) S_\lambda(r) \tag{1.17}$$

where we have assumed all microphysical processes are isotropic. In RE, these two quantities are equal *at every point* $\vec{r}$:

$$A - E = \int_0^\infty d\lambda \chi_\lambda (S_\lambda - J_\lambda) \equiv 0. \tag{1.18}$$

Suppose a model atmosphere with a particular temperature distribution does not satisfy Equation (1.18) at every point; it is not in radiative equilibrium. The goal of all temperature-correction procedures is to perturb T until the integral in Equation (1.18) vanishes simultaneously at every point in the model atmosphere.

One of the earliest devised temperature-correction schemes consisted of perturbing $S_\lambda(T)$ directly such that Equation (1.18) was satisfied, i.e.,

$$\int_0^\infty d\lambda \chi_\lambda [S(T_0) - J_\lambda] \neq 0 \tag{1.19}$$

$$\int_0^\infty d\lambda \chi_\lambda [S(T_0 + \Delta T) - J_\lambda] = 0. \tag{1.20}$$

Expanding S to first-order in T yields

$$\int_0^\infty d\lambda \chi_\lambda \left(S_\lambda(T_0) + \Delta T \left. \frac{\partial S_\lambda}{\partial T} \right|_{T_0} - J_\lambda \right) = 0 \tag{1.21}$$

$$\Delta T = \frac{\int_0^\infty d\lambda \chi_\lambda [J_\lambda - S_\lambda(T_0)]}{\int_0^\infty d\lambda \chi_\lambda \left. \frac{\partial S_\lambda}{\partial T} \right|_{T_0}}. \tag{1.22}$$

Without an *a priori* prescription for $S(T)$, the denominator cannot be evaluated.

We can subvert this problem slightly by assuming LTE:

$$\Delta T = \frac{\int_0^\infty d\lambda \kappa_\lambda^* [J_\lambda - B_\lambda(T_0)]}{\int_0^\infty d\lambda \kappa_\lambda^* \left.\frac{\partial B_\lambda}{\partial T}\right|_{T_0}} \tag{1.23}$$

where B_λ is the Planck function, we have set $\chi_\lambda \rightarrow \chi_\lambda^* = \kappa_\lambda^* + \sigma_T n_e$, and the asterisk adornment indicates an LTE value. Although numerically tractable in LTE, this method, confusingly also called "Λ-iteration," nevertheless fails in several physical regimes, for a variety of reasons which are described in Mihalas (1978). At large optical depth, $J \simeq B$, leading to a negligible temperature correction regardless of how badly the solution violates the radiative equilibrium condition. Similarly, any strong lines within the wavelength integrals will overwhelm contributions from all other frequencies, again leading to a nearly zero temperature correction.

Eventually it was discovered (Unsöld 1951, 1955; Lucy 1964) that a more robust scheme for calculating temperature corrections is to use information from the radiative transfer equation itself, as well as information from the *errors* in the perturbed moments (especially the flux H). This approach departs radically from Λ-iteration, since the latter takes no notice of the problem of transfer itself and focuses exclusively on the thermodynamic relationship between J and S (or B).

The family of so-called Unsöld-Lucy methods consists of the following logic:

1. Derive the zeroth and first moment equations from the radiative transfer equation.

2. Assuming the radiative equilibrium condition is not already satisfied, perturb the two moment equations with a new vector of temperatures $T(\vec{r})$, chosen

such that the radiative equilibrium condition *is* satisfied. Take advantage of the insensitivity of moment-weighted mean opacities to changes in temperature in order to reduce the number of new perturbed quantities (this was the critical contribution of Lucy (1964) which makes this procedure tractable).

3. Subtract the pair of perturbed moment equations from the original pair in order to derive a pair of equations which describe the necessary corrections to the various radiation moments.

4. Use known constraints or closure relations to reduce the number of unknown moments to 2, such that a unique solution can be found from the pair of perturbed moment equations.

5. Use the condition of radiative equilibrium to translate the moment perturbations into temperature perturbations, and solve for the temperature correction ΔT.

Below we demonstrate this procedure in the context of a spherically symmetric, homologously expanding medium.

In the mixed-frame formalism of Mihalas (1980), the bolometric zeroth moment of the radiative transfer equation is, to order $\mathcal{O}(v/c)$,

$$\begin{aligned} \frac{\rho}{c}\left[\frac{D}{Dt}\left(\frac{J}{\rho}\right) + K\frac{D}{Dt}\left(\frac{1}{\rho}\right) - (3K-J)\frac{v}{\rho r}\right] \\ = \int_0^\infty [\eta_\nu - \chi_\nu J_\nu] d\nu - \frac{1}{r^2}\frac{\partial[r^2 H]}{\partial r} - \frac{\dot{S}}{4\pi} \end{aligned} \tag{1.24}$$

where $\dot{S}$ is the instantaneous deposition of non-thermal or mechanical energy, and D/Dt represents the advective (co-moving) time-derivative:

$$\frac{D}{Dt} = \frac{\partial}{\partial t} + \vec{v} \cdot \vec{\nabla}. \tag{1.25}$$

In our calculations we neglect time-dependence in the radiation field, but because in the mixed-frame formalism of Mihalas (1980) spacetime quantities are measured in the Eulerian frame, this amounts to setting $\partial/\partial t = 0$, not $D/Dt = 0$. Therefore, the advective derivative terms in the zeroth moment equation are

$$\frac{DJ}{Dt} = v\frac{\partial J}{\partial r} \tag{1.26}$$

$$\frac{D\rho}{Dt} = -\frac{3\rho}{t} \tag{1.27}$$

$$\frac{D[\rho^{-1}]}{Dt} = \frac{3}{\rho t}. \tag{1.28}$$

Then the radiation energy equation becomes

$$\frac{1}{r^2}\frac{\partial[r^2 H]}{\partial r} = \int_0^\infty d\lambda[\eta_\lambda - \chi_\lambda J_\lambda] - \frac{\dot{S}}{4\pi}, \tag{1.29}$$

where we have now dropped all terms of order $\mathcal{O}(v/c)$. The first moment equation is

$$\frac{\partial K}{\partial r} + \frac{3K - J}{r} = -\int_0^\infty d\lambda \chi_\lambda H_\lambda. \tag{1.30}$$

To avoid numerical misbehavior at small radii, we introduce a modified version of

the "sphericality factor" defined originally by Auer (1971),

$$q(r) \equiv \frac{r_c^2}{r^2} \exp\left[\int_{r_c}^{r} dr' \frac{3f(r') - 1}{f(r')r'}\right] = \frac{r_c^2}{r^2} q_{\rm Auer}(r). \tag{1.31}$$

where $f(r) \equiv K(r)/J(r)$ is the Eddington factor, and r_c is an arbitrary reference radius which is generally chosen to make q close to unity in order to minimize numerical truncation,[4] and $f \equiv K/J$ is the variable Eddington factor. With this term we can re-write the first moment equation as

$$\frac{\partial[r^2 q f J]}{\partial r} = -\int_0^\infty d\lambda \chi_\lambda H_\lambda r^2 q. \tag{1.32}$$

We also define the flux-weighted mean opacity,

$$\chi_F \equiv \frac{\int_0^\infty d\lambda \chi_\lambda H_\lambda}{\int_0^\infty d\lambda H_\lambda} \tag{1.33}$$

such that

$$\frac{\partial[r^2 q f J]}{\partial r} = -\chi_F H r^2 q. \tag{1.34}$$

where $H \equiv \int_0^\infty d\lambda H_\lambda$. We can define similar weighted mean opacities for the zeroth moment equation:

$$\kappa_P \equiv \frac{\int_0^\infty d\lambda \kappa_\lambda B_\lambda}{\int_0^\infty d\lambda B_\lambda} \tag{1.35}$$

$$\kappa_J \equiv \frac{\int_0^\infty d\lambda \kappa_\lambda J_\lambda}{\int_0^\infty d\lambda J_\lambda} \tag{1.36}$$

[4] In `PHOENIX` r_c is set to the inner radius of the grid, $r_{\rm in}$. However the choice of r_c makes no difference in the calculations presented below, as all factors of r_c cancel analytically.

such that

$$\frac{1}{r^2}\frac{\partial[r^2 H]}{\partial r} = \kappa_P B - \kappa_J J - \frac{\dot{S}}{4\pi} \tag{1.37}$$

where we have set

$$\chi_\lambda = \kappa_\lambda B_\lambda + \sigma_T J \tag{1.38}$$

We now assume that, with a given temperature structure, the above two equations do *not* also satisfy the condition of radiative equilibrium at every point:

$$\kappa_P B = \kappa_J J. \tag{1.39}$$

We then assume that a temperature distribution exists which *does* satisfy this condition. We adorn quantities evaluated at the "target" temperatures with an apostrophe:

$$\frac{\partial[r^2 q f J']}{\partial r} = -\chi_F H' r^2 q \tag{1.40}$$

$$\frac{1}{r^2}\frac{\partial[r^2 H']}{\partial r} = \kappa_P B' - \kappa_J J' - \frac{\dot{S}}{4\pi}. \tag{1.41}$$

Because Unsöld's method is perturbative, we assume we are not too far from the temperature distribution which satisfies the condition of radiative equilibrium. We therefore have left unadorned those quantities which are relatively insensitive to temperature changes. Furthermore, because $\dot{S}$ is decoupled from the thermal pool, temperature changes leave it unaffected.

We now subtract the unperturbed moment equations from the perturbed ones:

$$\frac{\partial[r^2 q f(J'-J)]}{\partial r} = -\chi_F (H'-H) r^2 q \tag{1.42}$$

$$\frac{\partial[r^2 (H'-H)]}{\partial r} = r^2[\kappa_P (B'-B) - \kappa_J (J'-J)]. \tag{1.43}$$

Now we integrate the first moment equation from the outside inward and obtain

$$r^2 q f(J'-J) - R^2 q(R) f(R)[J'(R) - J(R)] = \int_R^r d\tilde{r} \chi_F q \tilde{r}^2 (H - H') \tag{1.44}$$

and make the Eddington approximation at the surface (Mihalas 1978):

$$J(R) \simeq 2H(R) \tag{1.45}$$

such that

$$r^2 q f(J'-J) = \int_R^r d\tilde{r} \chi_F q \tilde{r}^2 (H - H') - 2R^2 q(R) f(R)[H(R) - H'(R)]. \tag{1.46}$$

Now we plug this result for J into the zeroth moment equation and solve for $B' - B$:

$$\kappa_P r^2 (B'-B) = \frac{\partial[r^2 (H'-H)]}{\partial r} + \kappa_J \left\{ \frac{1}{qf} \left[\int_R^r d\tilde{r} \chi_F q \tilde{r}^2 (H - H') - 2q(R) f(R) R^2 (H - H') \right] \right\}. \tag{1.47}$$

The condition of radiative equilibrium allows us to eliminate the flux derivative

term:

$$\frac{\partial[r^2 H']}{\partial r} + \frac{\dot{S}}{4\pi} = r^2(\kappa_P B' - \kappa_J J') \equiv 0 \tag{1.48}$$

so

$$\kappa_P r^2(B' - B) = \kappa_J \left\{ \frac{1}{qf} \left[\int_R^r d\tilde{r} \chi_F q \tilde{r}^2 (H - H') - 2q(R) f(R) R^2 (H - H') \right] \right\} + (\kappa_J r^2 J - \kappa_P r^2 B) + \frac{\dot{S}}{4\pi}. \tag{1.49}$$

Finally we can translate this into a temperature perturbation:

$$B' - B = \Delta B = \frac{dB}{dT} \Delta T = \frac{4B}{T} \Delta T. \tag{1.50}$$

This procedure yields a new value of ΔT at the end of each temperature iteration. The only unknown in this equation is the target flux $H'(r)$ at each point. We can calculate this by prescribing as an outer boundary condition the emergent flux in the observer's frame, $H_{\rm obs}(R)$. This can be derived from measured photometry of a particular SN:

$$H_{\rm obs} = \frac{F_{\rm obs}}{4\pi} = \frac{L_{\rm obs}}{(4\pi)^2 D_L^2} \tag{1.51}$$

where D_L is the luminosity distance to the SN. `PHOENIX` assumes $D_L = 10$ pc such that its synthetic photometry automatically yields absolute magnitudes. Conveniently, the Lorentz transformations between Lagrangian and Eulerian forms of the *bolometric* radiation moments take simple forms; see eq. (9) of

Hauschildt (1992a).[5] One then can write a simple form for the "target" emergent flux measured in the co-moving frame (see eq. 11 of ibid.).[6] This choice of boundary condition requires the model to find the temperature vector $T(\vec{r})$ which *both* satisfies the condition of radiative equilibrium at every point, *and* yields a requested emergent luminosity. However in doing so it also introduces the complication that often the bolometric luminosity of most supernovae is poorly constrained since it requires simultaneous measurements of the SED across a broad range of wavelengths. One then transforms the observer's-frame $H(R)$ to the co-moving frame to obtain $H'(R)$. To obtain the target fluxes at all interior points, we integrate first moment equation from the outside inward this boundary condition (Hauschildt 1992b).

One may be tempted to conclude that the assumption of LTE for the final step of the temperature-correction procedure represents a flaw which is perhaps fatal, especially since NLTE effects in supernova atmospheres only grow with time. However this is likely not the case. Although we go to great lengths to incorporate as much physics as possible in the formation of temperature-correction procedures, the only truly useful information these algorithms provide is the *sign* of the temperature perturbation in each zone which will lead the model atomsophere closer and closer to satisfying the condition of radiative equilibrium. Rarely is the full value of ΔT, as derived above, applied after each iteration of the transfer equation; doing so generally leads to numerical instabilities and

[5]There is an error in the published version of this equation; it should say $H_{\rm obs} = \gamma^2[(1 + \beta^2)H + \beta(J + K)]$.

[6]Note that the Eddington factors defined in this equation are not the same ones used elsewhere.

negative temperatures during calculations. Instead, the results are frequently (and arbitrarily) damped, but *the sign of the perturbation is preserved*. Therefore, as long as $\partial B/\partial T$ and $\partial S_{\rm NLTE}/\partial T$ share the same sign, the scheme remains robust. After all, convergence of temperature-correction algorithms is determined not by the magnitudes of the corrections falling below some threshold value, but rather by the value of $\int_0^\infty d\lambda(\eta_\lambda - \chi_\lambda J_\lambda)$ becoming sufficiently small at every point.

This procedure works well near maximum light in supernova calculations, but less so at later times in SNe Ia. For this reason we explored a variety of alternative schemes for enforcing radiative equilibrium. We discuss these various schemes in Chapter 3 and Chapter 4.

There is a potential problem with tracking non-thermal rates in the way described above. Specifically, the quantity $\dot{S}/(4\pi)$ is the total rate of energy deposition by γ-rays and positrons, as described in Nugent, Baron, Branch, et al. (1997). This energy is in turn divided among the three non-thermal channels: ionization, excitation, and heating. By applying all of $\dot{S}$ to heating, while also including it in the calculation of non-thermal ionization, we are to some degree "double-counting." However, by how much we are in error is not clear, and indeed requires a full solution of the Boltzmann transport equation for these non-thermal electrons to discern (Kozma and Fransson 1992). Furthermore, there are likely larger uncertainties in the calculation of SN Ia spectra than this.

1.2.6 Atomic data

The accuracy of atomic data, e.g., line oscillator strengths, recombination rates, collisional rates, etc., is critical for producing physically consistent synthetic spectra. The robustness of the numerical methods discussed in Section 1.2 is of no value if the resulting spectrum, which is the only observable quantity in supernovae, is generated with inaccurate atomic data. Recent works such as Bautista et al. (2013) and Loch et al. (2013) have begun to quantify the propagation of these uncertainties as far through numerical calculations as possible, although this becomes difficult when such calculations use iterative scheme as does `PHOENIX`.

Probably the most reliable atomic data used in `PHOENIX` calculations are oscillator strengths of permitted atomic lines. The database of calculations by Kurucz (2011) is quite modern for most atoms and ions. These are supplemented by data from various sources listed in Lundqvist and Fransson (1996).

Rates of collisional processes are much more difficult to calculate, as they amount to solving many-body quantum scattering problems. As a result, the resulting formulae for collisional rates are quite approximate and valid only in certain regimes. For example, in previous `PHOENIX` calculations, which explicitly neglect forbidden lines, the collisional excitation/de-excitation rates for permitted transitions are taken from van Regemorter (1962):

$$q_{ji} = 20.6\lambda^3 T_e^{-1/2} A_{ji} \int_0^\infty d\left[yx^2\right] \bar{g}(x) e^{-yx^2} \tag{1.52}$$

where $y \equiv \Delta E_{ji}/k_B T$, and $\Delta E_{ji} \equiv E_j - E_i$ is the energy difference of the transition. In this result, the collisional rate q_{ij} is proportional to the Einstein coefficient A_{ij}; for permitted lines A is of order 100 MHz (Kramida et al. 2013). It is also exclusive to permitted transitions and, due to the proportionality to A, will likely give quite incorrect results for collisionally-induced, forbidden transitions, which have A of order 1 Hz.

Calculations of collisional rates among forbidden transitions are less common than those for permitted transitions. For example, in Seaton (1968, 1976) and Osterbrock and Ferland (2006), the collisional rates (units: $\mathrm{cm^3\,s^{-1}}$) are calculated as

$$q_{ij} = 8.629 \times 10^{-6} T^{-1/2} \Upsilon_{ij} g_i^{-1} \exp\left[\frac{-\Delta E_{ij}}{k_B T}\right] \tag{1.53}$$

$$\Upsilon_{ij} \equiv \int_0^\infty d\left[\frac{E}{k_B T}\right] \Omega_{ij}(T) \exp\left[-\frac{E}{k_B T}\right] \tag{1.54}$$

where Ω_{ij} is the unitless *collision strength* of the transition, which is proportional to the cross-section σ_{ij}, obtained from detailed quantum dynamics calculations. Generally Ω_{ij} is close to 1 and varies weakly with temperature (Osterbrock and Ferland 2006); therefore, if quantum mechanical calculations for Ω_{ij} for a particular transition are unavailable, one can simply set $\Omega = 1$, which is what we have done in the calculations presented here. Although this introduces errors in q_{ij}, it is nevertheless preferable to, e.g., setting $q_{ij} = 0$, which decouples levels i and j.

Formally, permitted and forbidden transitions are distinguished by the quantum selection rules they obey or violate as they transition from one angular momentum configuration to another. However, rather than labeling each transition in the

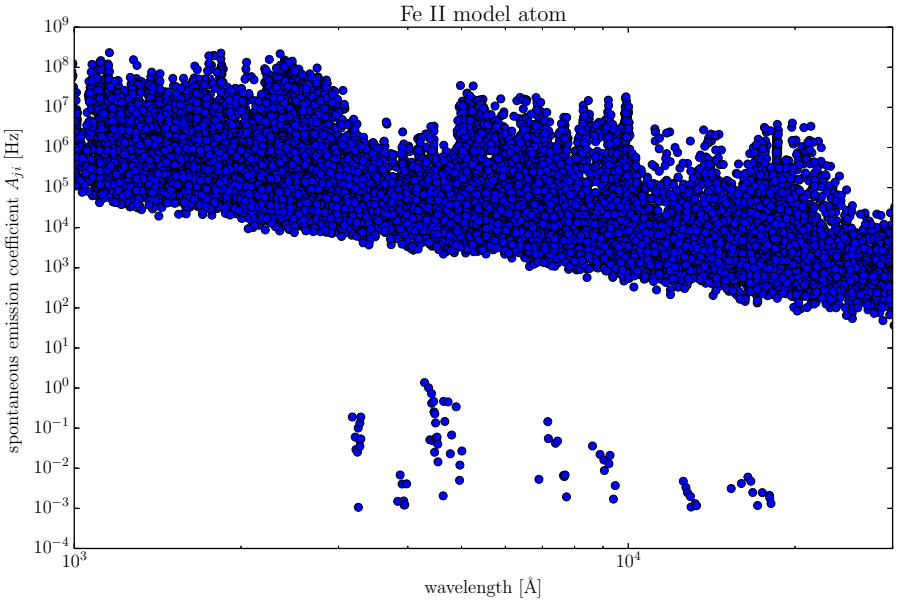

Figure 1.3: Distribution of radiative rate coefficients A_{ji} for the Fe II model atom used in `PHOENIX`.

`PHOENIX` atomic database as "permitted" or "forbidden," we observed trends in the A_{ji} values among the various model atoms and found that a wide and clean gap exists between the radiative rates of permitted and forbidden lines. For example, the distribution of radiative rates A_{ji} for the Fe II model atom is shown in Figure 1.3. From this plot we simply inferred that a cutoff value of $A_{ji} = 10$ Hz divides all transitions correctly into "permitted" or "forbidden" categories. Such a scheme is highly desirable over reconfiguring the entire atomic database to label every radiative transition with its appropriate type.

Chapter 2

Supernova resonance-scattering line profiles in the absence of a photosphere

In supernova SN spectroscopy relatively little attention has been given to the properties of optically thick spectral lines in epochs following the photosphere's recession. Most treatments and analyses of post-photospheric optical spectra of SNe assume that forbidden-line emission comprises most if not all spectral features. However, evidence exists that suggests that some spectra exhibit line profiles formed via optically thick resonance-scattering even months or years after the SN explosion. To explore this possibility, we present a geometrical approach to SN spectrum formation based on the "Elementary Supernova" model, wherein we investigate the characteristics of resonance-scattering in optically thick lines while replacing the photosphere with a transparent central core emitting non-blackbody continuum radiation, akin to the optical continuum provided by decaying ^{56}Co formed during the explosion. We develop the mathematical framework necessary for solving the radiative transfer equation under these conditions and calculate spectra for both isolated and blended lines. Our comparisons with analogous results from the Elementary Supernova code `SYNOW` reveal several marked differences in line formation. Most notably, resonance lines in these conditions form P Cygni-like profiles, but the emission peaks and absorption troughs shift redward and

blueward, respectively, from the line's rest wavelength by a significant amount, despite the spherically symmetric distribution of the line optical depth in the ejecta. These properties and others that we find in this work could lead to misidentification of lines or misattribution of properties of line-forming material at post-photospheric times in SN optical spectra.

2.1 Introduction

Many of the physical processes that contribute to spectrum formation in a SN change dramatically as it ages. Given the difficulty and complexity of including all such processes, as well as their evolution in time, exploration into this computational frontier has begun only very recently (Pinto and Eastman 2000; Höflich 2003; Kasen, Thomas, et al. 2006; Jack et al. 2009; Kromer and Sim 2009; De et al. 2010b; Dessart and Hillier 2010; Hillier and Dessart 2012). Most work in SN spectroscopy has focused on the early "photospheric" phase, comprising the time from explosion to a few weeks post-maximum light, where resonance-scattering from permitted lines dominates the spectrum (Branch, Lacy, et al. 1983; Branch, Doggett, et al. 1985; Jeffery, Leibundgut, et al. 1992; Mazzali and Lucy 1993; Mazzali, Danziger, et al. 1995; Fisher et al. 1997; Hatano, Branch, Fisher, Baron, et al. 1999; Mazzali 2000, 2001; Branch, Baron, et al. 2005; Dessart and Hillier 2005; Mazzali, Benetti, et al. 2005; Hachinger et al. 2006). Considerably less attention has been given to the "nebular" phase, several months or more after explosion, where emission from forbidden lines constitute most of the spectrum (Axelrod 1980; Ruiz-Lapuente and Lucy 1992; Kozma and Fransson 1998a,b;

Mazzali, Cappellaro, et al. 1998; Maeda, Nomoto, et al. 2006; Jerkstrand et al. 2011; Mazzali, Maurer, et al. 2011). Finally, the intermediate phases, that is, a few months post-explosion, have received the least amount of scrutiny (Maurer et al. 2011). One reason so much attention focuses on either very early or very late times is that in these regimes one can reproduce with reasonable fidelity the physical processes that dominate spectrum formation through a number of simplifying assumptions. For example, in the early, photospheric phase the Sobolev approximation (Castor 1970) and a resonance-scattering source function (Jeffery and Branch 1990) are both accurate approximations due to the high densities and steep velocity gradients in the SN ejecta; at late times one typically assumes both that the ejecta are optically thin and that line emission arises exclusively from forbidden lines (Axelrod 1980). However these two groups of assumptions are generally incompatible with each other in the intermediate regime of an SN.

Complicating matters further is the possibility that the evolution of the different types of line-forming processes is asynchronous. Specifically, the emergence of forbidden emission lines in an SN spectrum may not herald the systematic withdrawal of resonance-scattering in optically thick permitted lines. Though this possibility has frequently been acknowledged (Bowers et al. 1997; Branch, Baron, et al. 2005; Jerkstrand et al. 2011), it has to our knowledge never been pursued in detail until now. To illustrate this point we show in Figure 2.1 and Figure 2.2 `SYNOW` fits to the day +87 optical spectrum of SN 2003du and the day +115 spectrum of SN 1994D, respectively. In the SN 2003du fit we use only three ions: Na I, Ca II, and Fe II. The photospheric velocity is 7000 $\mathrm{km\,s^{-1}}$, and the

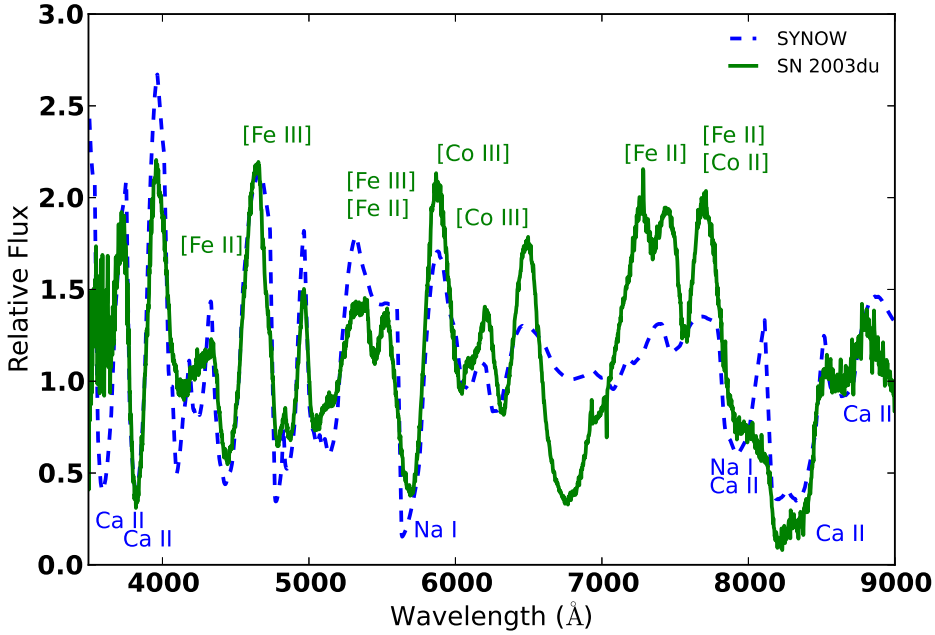

Figure 2.1: SYNOW fit to the +87 day spectrum of SN 2003du. The synthetic spectrum contains Na I, Ca II, and Fe II, each with an excitation temperature of 7000 K. The photospheric velocity is 7000 $\mathrm{km\,s^{-1}}$, and the spectrum has been divided through by the blackbody continuum. The permitted line identifications (in blue) are from the SYNOW fit, with Fe II features unlabeled. The alternative forbidden-line IDs (in green) follow those in other SNe Ia made by Bowers et al. (1997).

photospheric temperature is 8000 K. The excitation temperature of all three ions is 7000 K. In the SN 1994D fit, we include five ions: Na I, Ca II, Cr II, Fe II, and Co II. Here, the photospheric velocity is 6000 $\mathrm{km\,s^{-1}}$ and the temperature is 10 000 K. The excitation temperature of all ions is 7000 K. The observed and synthetic spectra of both SN 1994D and SN 2003du have been flattened using the method of Jeffery, Ketchum, et al. (2007).

The fits to the observed spectra in both of these figures are relatively good, and in both fits only permitted lines were considered. Even among the features that SYNOW cannot reproduce accurately, most of the emission peaks and absorption

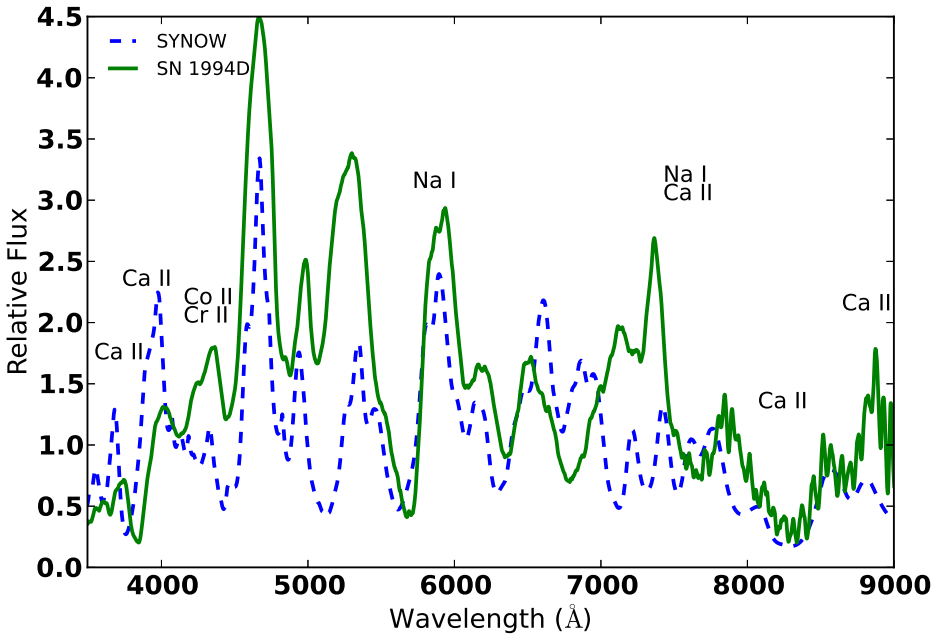

Figure 2.2: SYNOW fit to the +115 day spectrum of SN 1994D. The synthetic spectrum contains Na II, Ca II, Cr II, Fe II, and Co II, each with an excitation temperature of 7000 K. The photospheric velocity is 6000 $\mathrm{km\,s^{-1}}$, and the spectrum has been divided through by the blackbody continuum. As in Figure 2.1 the unlabeled features in the SYNOW spectrum are due to Fe II.

troughs in the synthetic spectra form at the same wavelengths as in the observed spectra, and only the strengths of the features are disparate. (The exceptions to this are the wavelength range 6600-7800 Å in SN 2003du and 6600-7500 Å in SN 1994D, throughout which `SYNOW` fails completely to reproduce the observed features.) It would therefore be a remarkable coincidence if the observed features in these two objects arise from purely forbidden emission (Branch, Baron, et al. 2005).

In addition to the circumstantial evidence for persistent resonance-scattering provided by these reasonably good `SYNOW` fits to several-months-old SNe Ia, calculations by Hatano, Branch, Fisher, Millard, et al. (1999) and Jerkstrand et al. (2011) further defend this claim. Hatano, Branch, Fisher, Millard, et al. (1999) calculated the Sobolev optical depth (Equation (1) of that paper) for the most common ions observed in SN Ia optical spectra. In Figure 9(c) of that work they show the Sobolev local thermodynamic equilibrium (LTE) optical depth for Fe I & II and Co I & II for an iron-rich composition at 80 days post-explosion in an SN Ia model, and find that the optical depths for those ions can be as high as $\tau \sim 50\,000$. Similarly, the simplified form of the Sobolev optical depth shown in Equation (39) of Jerkstrand et al. (2011) shows that the optical depths for some UV resonance lines (e.g., Mg II λ 2798) can still be as high as $\tau \sim 1000$ even 8 *years* post-explosion.

In light of the evidence presented above for resonance-scattering at relatively late times in SNe Ia, we present a geometrical exploration of this phenomenon in the spirit of the Elementary Supernova approach of Jeffery and Branch (1990).

Rather than attempt to discern exactly how late after an SN explosion resonance-scattering continues to contribute significantly to spectrum formation, we assume simply that the photosphere has receded and that the continuum opacity in the core of the SN is negligibly small. We replace the photosphere with a transparent core emitting non-blackbody continuum radiation and distribute ions both inside this "glowing" core and outside the core in a non-emitting shell. We then calculate emergent flux profiles for lines with parameterized optical depths in several different geometrical configurations. We scrutinize line formation and behavior in both isolated and blended cases. Because `SYNOW` inspired this model, the two naturally invite comparison, which we indulge throughout this work.

2.2 A transparent, uniformly emitting core

We begin by assuming the SN is spherically symmetric. Under this circumstance it is natural to work in (p, z) coordinates, where p is the impact parameter of a ray relative to the center of the SN, such that the $p = 0$ ray exactly bisects the SN; and z is orthogonal to p, with the $z = 0$ line also exactly bisecting the SN. We will at times transform to spherical polar coordinates for computational expedience, where the radial coordinate r satisfies

$$r^2 = p^2 + z^2. \tag{2.1}$$

We also assume that the SN undergoes homologous expansion, $v = r/t$, so that surfaces of constant line-of-sight velocity are vertical planes, that is, planes of

constant z. We further assume that the observer is located at $z \to -\infty$, in which case all rays incident on the observer are parallel. Next, we assume that the photosphere has receded and has been replaced by a transparent, spherically symmetric core with outer radius r_c which emits continuum (but not blackbody) radiation. The post-photospheric spectra of many SNe Ia contain a flat and weak continuum which is either thermal in nature or, as Bowers et al. 1997 suggest, due to the sea of weak optical lines of lowly ionized Fe and Co. At very late times when the spectrum becomes truly nebular, there is no optical thermal continuum, but we do not seek to extend our methods into this very late regime. To mimic this pseudo-continuum we assign to the core a grey, spatially constant volume emissivity $j_\lambda(r) = j$ for all radii $r \leq r_c$ and all wavelengths λ. This assumption allows us to present simple analytic results; with only slight modification, our methods for calculating line profiles are amenable to chromatic emissivity.

2.2.1 Continuum only

In general, to calculate the emergent flux from a SN atmosphere one must first calculate the source function at all locations in the SN, followed by the emergent intensity of rays exiting the ejecta toward the observer. However, since in this model we neglect all continuum opacity, the source function is not a well defined quantity in the absence of lines. Therefore we write down immediately the emergent intensity of a constant p ray originating at the back[1] of the core and traversing toward the observer, without calculating the source function. When no

[1]In this discussion "front" and "back" refer to locations in the SN nearest to and farthest from the observer, respectively.

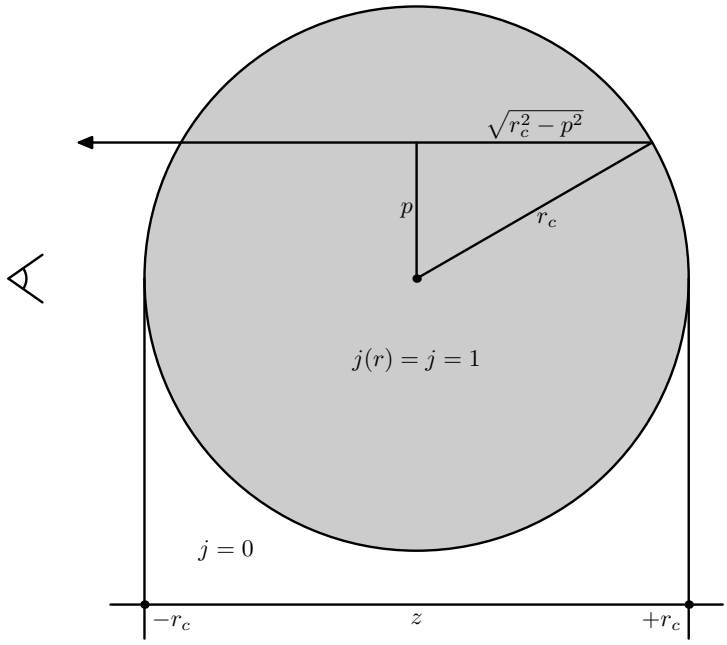

Figure 2.3: A continuum ray in the core of the SN. In this figure and all which follow, we use grey shading to label the continuum-emitting region.

lines are present the intensity of a ray passing through the core is proportional to its geometric length:

$$I(p) = 2j(r_c^2 - p^2)^{1/2}. \tag{2.2}$$

A representative intensity ray is shown in Figure 2.3. If instead the emissivity has spatial dependence, $j = j(r)$, the result has a more general form:

$$I(p) = \int_{-(r_c^2-p^2)^{1/2}}^{(r_c^2-p^2)^{1/2}} j((p^2+z^2)^{1/2})dz = 2\int_0^{(r_c^2-p^2)^{1/2}} j((p^2+z^2)^{1/2})dz \tag{2.3}$$

where we have transformed the argument of j since the intensity along a ray of constant p depends only on its z coordinate.

Already a physical peculiarity arises: limb darkening in the absence of scatter-

ing or absorption. The traditional interpretation of limb darkening in photospheric objects such as dwarf stars and young SNe is that intensity rays with large impact parameter p, that is, rays which emerge from the limb, reach an optical depth of $\tau \simeq 1$ at shallower layers in the atmosphere than low-impact parameter rays. Under the assumption of local thermodynamic equilibrium (LTE), shallower locations in atmospheres have lower temperatures and thus weaker source functions, since LTE requires by definition that $S = B$ where B is the Planck function. A weaker source function in turn leads to a lower intensity emergent ray, the cumulative result of which is limb darkening.

In the case of this post-photospheric model, however, high-p rays accumulate less continuum as they proceed from the back of the object toward the observer. Such accumulation does not occur in photospheric-phase atmospheres of SNe except through lines in the atmosphere which scatter continuum photons from the blackbody photosphere into the ray; however, this contribution is small except when the line has an extraordinarily high optical depth.

Using Equation 2.2, the continuum flux at all wavelengths is given by

$$F_\lambda \equiv \int I_\lambda \cos\theta d\Omega = \frac{2\pi}{r_c^2} \int_0^{r_c} I_\lambda p dp = \frac{4\pi}{3} j r_c. \tag{2.4}$$

For clarity, and without loss of generality, hereafter we set $j \equiv 1$, so I_λ, J_λ, and F_λ have units of length and the geometric nature of our results becomes apparent. In addition, since in homologous expansion $v \propto r$, we interchange lengths and velocities where convenient.

2.2.2 Mean intensity

We now calculate the mean intensity, J, both inside and outside the glowing core. Without any lines, J is not a particularly useful quantity in this model since we do not need it to calculate the emergent flux. However, when we add a single line to the core in §2.3 we require the source function to calculate the emergent intensity, and in the resonance-scattering approximation $S = J$.

By definition,

$$J_\lambda(r) \equiv \frac{1}{4\pi} \int I_\lambda(r) d\Omega = \frac{1}{2} \int_{-1}^{1} I_\lambda(r) d\mu \tag{2.5}$$

where $\mu \equiv \cos\theta$, and we have applied to the radiation field the condition of azimuthal symmetry. Inside the core, $r \leq r_c$, so from Figure 2.4,

$$X = r\mu + \left(r^2\mu^2 + r_c^2 - r^2\right)^{1/2}. \tag{2.6}$$

Setting $I_\lambda(r) = X(r)$, plugging this into Equation (2.5), and using standard integral tables, we find

$$J(r) = \frac{1}{2r} \left\{ r r_c + \frac{(r_c^2 - r^2)}{2} \ln\left[\frac{r_c + r}{r_c - r}\right] \right\}. \tag{2.7}$$

Calculating the mean intensity outside the core (with the line still inside the core) is slightly more complicated and we include the derivation in Appendix A. The

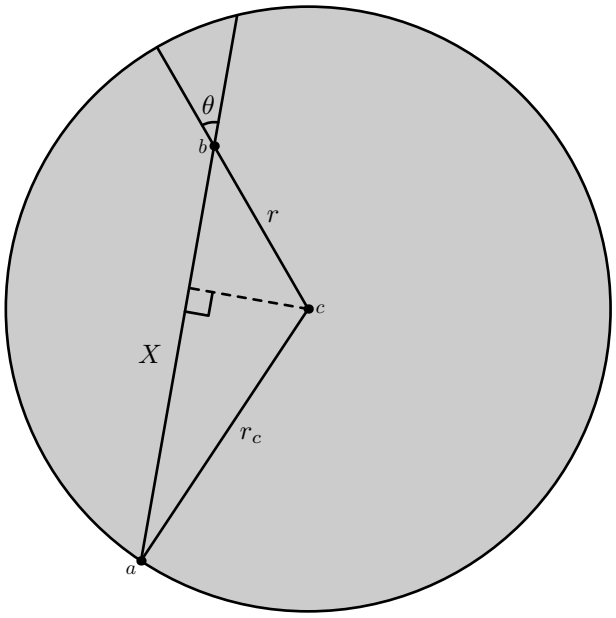

Figure 2.4: Geometric configuration used to calculate $J(r < r_c)$ both for pure continuum and for a single line in the core. X is the magnitude of the vector $\overrightarrow{ab}$, r_c is that of $\overrightarrow{ac}$, and r is that of $\overrightarrow{bc}$.

result is:

$$J(r) = \frac{1}{2r}\left\{ rr_c + \frac{(r^2 - r_c^2)}{2} \ln\left[\frac{r - r_c}{r + r_c}\right]\right\}. \tag{2.8}$$

Figure 2.5 shows the behavior of $J(r)$ in units of r_c and for comparison the dilution factor $W(r)$ (Mihalas 1978) is also shown. The shape of J is vary similar to that of a Gaussian and it is larger than $W(r)$ until quite large r, where both functions behave as $\frac{1}{4}(\frac{r_c}{r})^2$. We emphasize that J peaks strongly at $r = 0$, a result which affects line formation significantly, as we will discuss in Section 2.3.

2.3 A line in the core

We now treat the case of a single line, forming inside the core. We assume, for simplicity, a constant Sobolev optical depth τ in the line throughout the

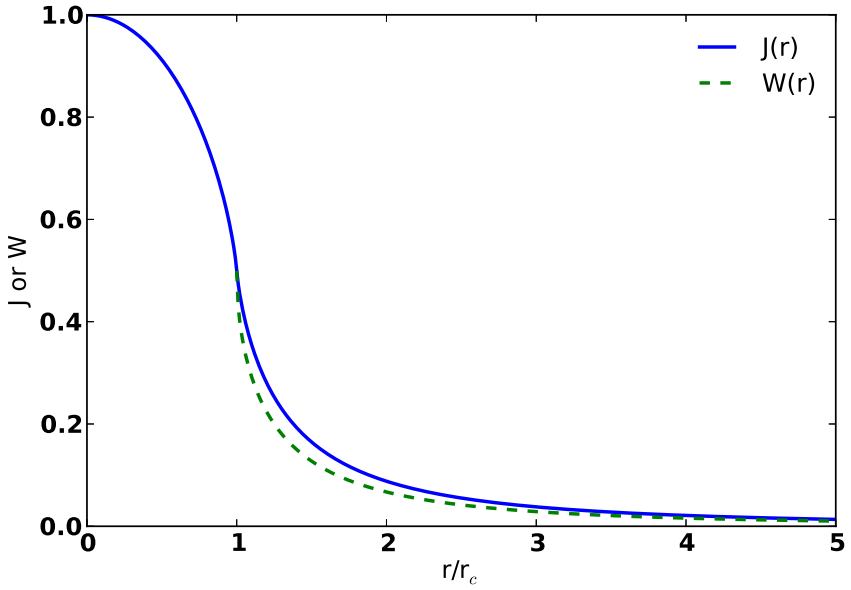

Figure 2.5: The profile of $J(r)$ and $W(r)$, where W is the dilution factor.

core. Before continuing, we note that the most profound effect of homologously expanding matter on the radiation field is that photons redshift with respect to the matter regardless of propagation direction. Therefore photons in a ray which starts at the back of the core and emerges toward the observer redshift continuously as they move along the ray. Referring to Figure 2.6, if a ray originates in front of the plane of constant $z_{\rm res}$ corresponding to the location in the core $z = z_{\rm res}$ where the line Doppler shifts into resonance with a particular wavelength point — that is, if $p > (r_c^2 - z_{\rm res}^2)^{1/2}$ — then the intensity of that ray is simply its continuum value, given by Equation (2.2). However, if the ray forms behind that plane — if $p < (r_c^2 - z_{\rm res}^2)^{1/2}$ — the line attenuates some of the continuum intensity by scattering photons out of the ray and therefore out of the observer's line of sight. In the Sobolev approximation this attenuation manifests as a $e^{-\tau}$ term multiplying the continuum intensity at the location of the line. In addition

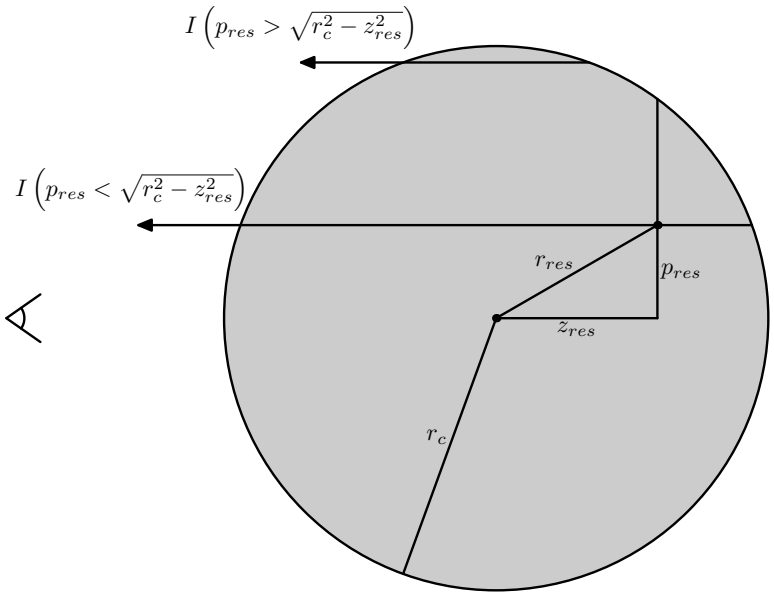

Figure 2.6: Intensity rays with a single line in the core.

to attenuating the intensity along a ray, the line also contributes to the intensity via its source function $S(r[z_{\rm res}])$. Specifically, the contribution is

$$I_{\rm line} = S(1 - e^{-\tau}). \tag{2.9}$$

The two different types of rays are depicted in Figure 2.6. Their emergent intensities are

$$I_{z_{\rm res}}(p) = \begin{cases} ((r_c^2 - p^2)^{1/2} - z_{\rm res})e^{-\tau} + S(r)(1 - e^{-\tau}) & \\ \quad +(r_c^2 - p^2)^{1/2} + z_{\rm res} & p < (r_c^2 - z_{\rm res}^2)^{1/2} \\ 2(r_c^2 - p^2)^{1/2} & p > (r_c^2 - z_{\rm res}^2)^{1/2} \end{cases} \tag{2.10}$$

The integral over $I_{z_{\rm res}}(p)$ is straightforward except for the term containing the source function $S(r)$. To integrate this term we define

$$g(z_{\rm res}) \equiv \int_0^{\sqrt{r_c^2 - z_{\rm res}^2}} S(r) p dp = \int_0^{\sqrt{r_c^2 - z_{\rm res}^2}} \frac{1}{2r} \left[r r_c + \frac{r_c^2 - r^2}{2} \ln \left[\frac{r_c + r}{r_c - r} \right] \right] p dp. \tag{2.11}$$

We then transform the integration variable from p to r, which leads to

$$g(z_{\rm res}) = \int_{z_{\rm res}}^{r_c} \frac{1}{2r} \left[r r_c + \frac{r_c^2 - r^2}{2} \ln \left[\frac{r_c + r}{r_c - r} \right] \right] r dr.$$

This integral is still unwieldy, so we transform integration variables once again by defining

$$\mu \equiv \frac{z_{\rm res}}{r}$$

and

$$\mu_{\rm res} \equiv \frac{z_{\rm res}}{r_c}$$

from which we find

$$\frac{r}{r_c} = \frac{\mu_{\rm res}}{\mu}.$$

We then change the integration variable from r to μ, which yields

$$g(z_{\rm res}) = \frac{r_c^3}{2} \mu_{\rm res}^2 \int_{\mu_{\rm res}}^1 \left[1 + \frac{\mu^2 - \mu_{\rm res}^2}{2 \mu \mu_{\rm res}} \ln \left[\frac{1 + \mu_{\rm res}}{1 - \mu_{\rm res}} \right] \right] \frac{d\mu}{\mu^3}.$$

The result is

$$g(z_{\rm res}) = \frac{r_c^3}{6}\left[1 + 2\ln 2 - \mu_{\rm res}^2 - \frac{\mu_{\rm res}}{2}(3-\mu_{\rm res}^2)\ln\left[\frac{1+\mu_{\rm res}}{1-\mu_{\rm res}}\right] - \ln(1-\mu_{\rm res}^2)\right]. \tag{2.12}$$

The remainder of Equation 2.4 poses little challenge and leads directly to an analytic result for the flux profile for the constant-τ case:

$$F(z_{\rm res}) = \frac{2\pi}{r_c^2}\left[\frac{2r_c^3}{3} + (1-e^{-\tau})\left[g(z_{\rm res}) + \frac{z_{\rm res}(r_c^2 - z_{\rm res}^2)}{2} - \frac{r_c^3 - |z_{\rm res}|^3}{3}\right]\right]. \tag{2.13}$$

We remark here that, although Equation 2.4 defines the flux as a function of wavelength, we have derived Equation 2.13 in terms of the coordinate $z_{\rm res}$. One transforms between $z \leftrightarrow \lambda$ using the first-order Doppler formula,

$$z = r_{\rm max}\left(\frac{c}{v_{\rm max}}\right)\frac{\lambda - \lambda_0}{\lambda_0}, \tag{2.14}$$

where $r_{\rm max}$ ($v_{\rm max}$) is the maximum radius (velocity) of the ejecta. We show in Figure 2.7 the line profiles of Na I D, λ5892, with several different optical depths.[2] For comparison we show in Figure 2.8 the profile of Na I D as calculated by `SYNOW`, with the same optical depths as in Figure 2.7.

The profiles in both plots appear quite P Cygni-like, but differences do exist between them. We highlight two in particular. First, when a photosphere is present as in `SYNOW`, the emission peak of a line profile is located at its rest

[2]Examining Figure 2.1 and Figure 2.2, identification of Na I is ubiquitous; we therefore use the Na I D line for illustrative purposes.

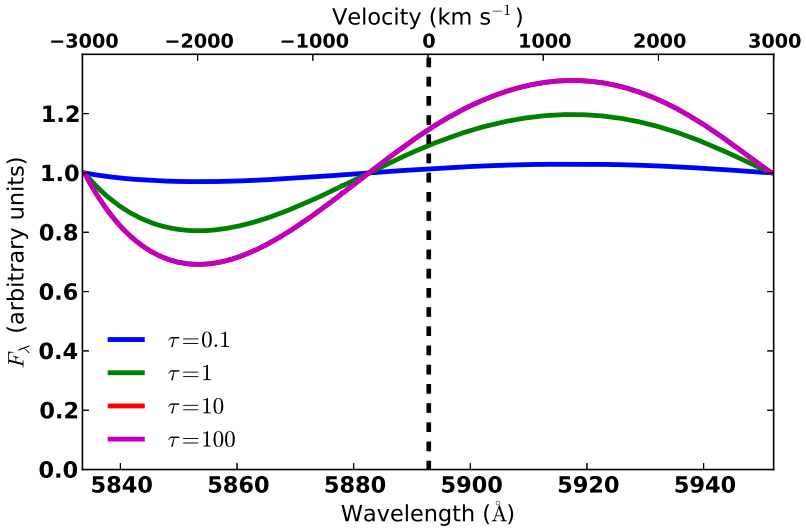

Figure 2.7: Flux profiles for Na I D, λ5892, in the post-photospheric model, with spatially constant optical depth and an outer core velocity of 3000 km s^{-1}. The vertical dashed line indicates the rest wavelength of the line. The $\tau = 10$ and $\tau = 100$ profiles overlap almost exactly and are indistinguishable in this figure. In contrast to `SYNOW` the red emission peak does not occur at the rest wavelength, but rather is redshifted by an amount independent of optical depth.

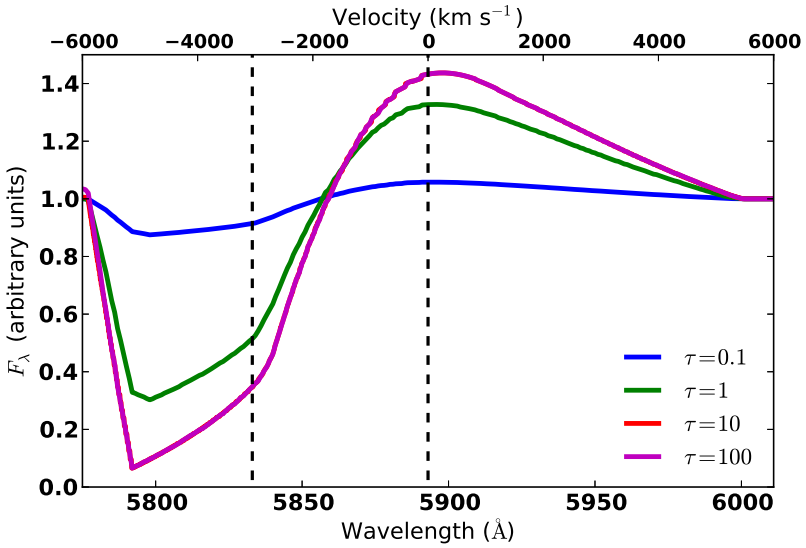

Figure 2.8: Flux profiles for Na I D in `SYNOW`, with photospheric velocity 3000 km s^{-1} and spatially constant optical depth. The maximum velocity of the line-forming region is 6000 km s^{-1}. The right dashed vertical line indicates the rest wavelength of the Na I D line (λ5892), and the left vertical line indicates the blueshifted rest wavelength of Na I D at the photospheric velocity. The $\tau = 10$ and $\tau = 100$ profiles overlap almost exactly and are indistinguishable in this figure. Unlike the profiles in Figure 2.7, the emission peak in the `SYNOW` case remains fixed at the line rest wavelength regardless of the optical depth.

wavelength, regardless of the velocity of the material forming the line in the SN atmosphere. This fact simplifies enormously the task of identifying isolated lines in a SN spectrum (Jeffery and Branch 1990). In the post-photospheric model, however, the emission peak is *not* centered on the line rest wavelength; rather it is considerably redshifted. As Figure 2.7 shows, with a core outer edge velocity of only 3000 $\mathrm{km\,s^{-1}}$, the emission peak is ~ 15 Å redward of the line rest wavelength. Though the absorption component of a P Cygni profile is used more often than the corresponding emission to identify lines in a spectrum (since the former dominates the latter in overlapping lines; see ibid.), this redshift could lead to misidentification of lines in intermediate- or late-time SN spectra.

What is the origin of the emission peak redshift? This question is easier to answer in the limit $\tau \to \infty$, the line profile for which would look identical to that of $\tau = 100$ in Figure 2.7. In the $\tau \to \infty$ case the line at the resonance point z_{res} scatters *all* continuum photons forming in the ray segment $z > z_{\mathrm{res}}$ out of the ray, and the contribution of the line to the intensity along that ray is simply $I_{\mathrm{line}} = S(r[z_{\mathrm{res}}])$. Thus only two sources of emission contribute to the flux at a given wavelength: 1.) the continuum emission in front of the resonance plane at $z = z_{\mathrm{res}}$; and 2.) the source function at the plane. If the plane is located near the back of the core, $z \lesssim r_c$, the portion of the core's volume which emits continuum photons which escape unscattered and reach the observer is large. However, because the surface area of the plane is small when z is close to r_c, and because from Figure 2.5 we see that S is small at $r \sim r_c$ — only half of its maximum value — the emission contribution from the source function on the

plane is in turn relatively small.

As the resonance plane moves forward (to bluer wavelengths, smaller z), the volume of the emitting core in front of the plane decreases, but the surface area of the plane grows, and Figure 2.5 shows that the source function at the plane grows quickly as well. From $\frac{1}{3}r_c \lesssim z \lesssim r_c$ the scattering emission from the resonance plane more than compensates for the diminishing continuum emission from the core, causing the flux to increase monotonically as one moves blueward in that region, eventually reaching the emission peak, which in Figure 2.7 is $\sim$ 5915 Å. Blueward of this peak, despite the fact that S increases monotonically until reaching $z = 0$, the surface area of the plane increases only slightly when $z \gtrsim 0$ and the now very large resonance plane occults so much of the core over a small shift Δz that it can no longer compensate for the large amount of emission removed from the volume of the core behind it, causing the flux to decrease as z becomes smaller. This transition point exists *redward* of $z = 0$ and thus the emission peak of the P Cygni profile is redder than the rest wavelength of the line.

Blueward of $z = 0$, that is, $-r_c < z < 0$, the area of the resonance plane begins to decrease, now only obscuring a cylindrical volume of the glowing core. Even though the length of this occulted cylinder increases as z becomes more negative, its radius decreases, and the portion of the total volume of the core that this cylinder comprises decreases as well. The now-unocculted limbs of the core, emitting continuum which the resonance plane can no longer scatter away, grow in volume and eventually compensate once again for the cylindrical volume obscured by the plane, causing the flux to increase. This transition point manifests as the

absorption minimum in the flux profile ($\sim$ 5855 Å in Figure 2.7), blueward of which the flux increases until the resonance plane reaches $z = -r_c$ and we recover pure continuum.

The second difference between the line profiles with and without a photosphere is that, in the former, the flux in strong lines deviates from the continuum by a large amount, whereas in the latter the changes are small. The flux in the absorption minimum of the $\tau_0 = 100$ line in Figure 2.8, for example, is 80% lower than the continuum value. In our post-photospheric model, on the other hand, even the strongest line in Figure 2.7 departs by only up to 30% from the continuum. That the post-photospheric model exhibits such small departures from continuum is due to the ability of a small portion of the core to emit unscattered photons toward the observer even when the resonance plane is near the front. In the `SYNOW` case, the shell above the photosphere does not emit any continuum, so when the plane is close to the front of the ejecta, only scattering from the plane itself contributes to the flux, causing it to be extremely low at the absorption minimum.

The physical simplicity of constant τ line profiles such as those in Figure 2.7 and Figure 2.8 readily facilitates analysis of line formation in SN ejecta, as we have just seen. However, one must also be aware of complicating effects such as the inhomogeneous structure of SNe, viz. the velocity-dependent density profile. In the Elementary Supernova framework one assumes implicitly that $\tau = \tau(\rho)$, where ρ is the matter density, and accounts for this by writing τ as, e.g., an exponential or power law function which decreases with increasing velocity. To illustrate how a

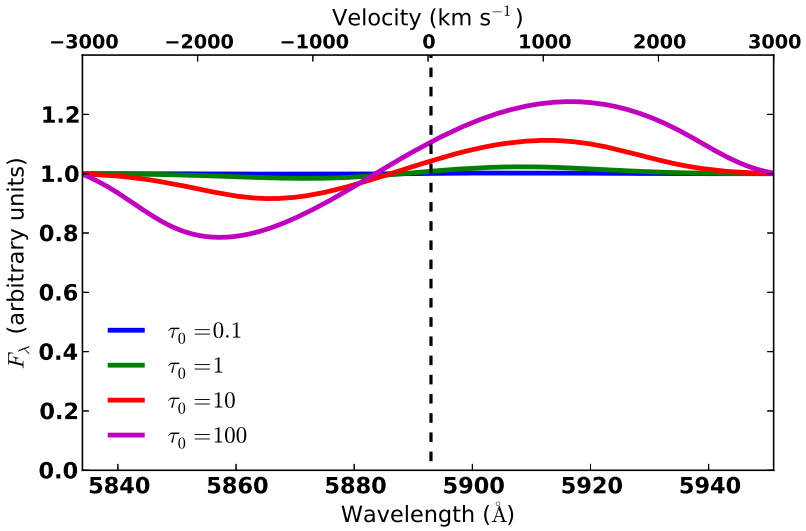

Figure 2.9: Flux profiles for Na I D, λ5892, in the post-photospheric model with outer edge core velocity 3000 km s^{-1} and a line optical depth following an exponential decay, $\tau(v) = \tau_0 \exp(-v/v_e)$, where $v_e = 500$ km s^{-1}. The vertical dashed line indicates the rest wavelength of the line. In contrast to SYNOW, the red emission peak does not occur at the rest wavelength, but is rather significantly redshifted by an amount which depends on the strength of the line. Also unlike SYNOW, the blue absorption minimum blueshifts continuously with increasing optical depth.

variable optical depth affects line formation we show in Figure 2.9 the line profile of Na I D in our post-photospheric model with $\tau(v) = \tau_0 \exp(-v/v_e)$, where τ_0 is a constant and $v_e = 500$ km s^{-1}. Again, for comparison, we show in Figure 2.10 a SYNOW plot of the same line with the same exponential τ profile.

In the post-photospheric case, shown in Figure 2.9, the relationship between velocities and the positions of the emission maximum and absorption minimum is not immediately obvious. Like the SYNOW line profiles, shown in Figure 2.10, the blue edge of the absorption component (not of the absorption *minimum*; see 5835 Å in Figure 2.9, and 5775 Å in Figure 2.10) indicates the maximum velocity of the line-forming material, although in blended cases this can be difficult to

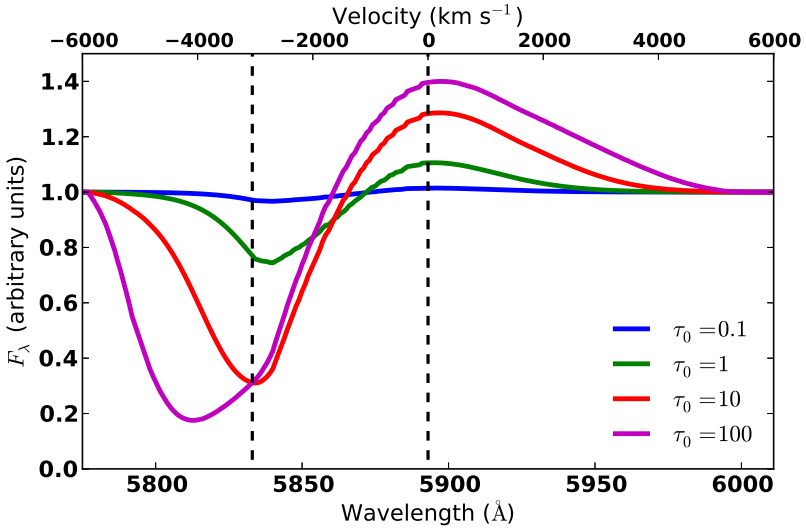

Figure 2.10: Flux profiles for Na I D, λ5892, in SYNOW, with photospheric velocity 3000 km s^{-1} and a line optical depth following an exponential decay, $\tau(v) = \tau_0 \exp(-v/v_e)$, where $v_e = 500$ km s^{-1}. The maximum velocity of the line-forming region is 6000 km s^{-1}. The right vertical dashed line indicates the rest wavelength of the line, and the left dashed line indicates the wavelength of Na I D blueshifted to the photospheric velocity. Except for extremely high optical depths, the blue edge of the absorption minimum remains fixed at the photospheric velocity; and for all optical depths, the red emission peak remains at the rest wavelength of the line.

discern. Unlike SYNOW, in this model both the peak and trough continuously redshift and blueshift, respectively, as the line optical depth increases. In the SYNOW case, on the other hand, the separation between the rest wavelength of the line and the minimum of the blueshifted absorption component indicates the velocity of the photosphere and thus the minimum velocity of the line-forming material itself (assuming the material is not "detached" above the photosphere, Jeffery and Branch 1990). Only when the line optical depth is extremely high does the location of the absorption minimum begin to move blueward of the photospheric blueshift, as in the $\tau_0 = 100$ line in Figure 2.10. For each of the three weaker lines in that figure, one can simply measure the blue edge of the absorption minimum, $\sim$ 5830 Å, then calculate the photospheric velocity, $\sim$ 3000 $\mathrm{km\,s^{-1}}$.

We also note that the $\tau = 10$ and $\tau = 100$ line profiles in Figure 2.7 and Figure 2.8 appear identical, whereas in Figure 2.9 and Figure 2.10 the $\tau_0 = 10$ and $\tau_0 = 100$ profiles are distinct. This difference is due to the velocity dependence of τ: in the former pair of figures, the optical depth is constant everywhere, leading to a saturated profile throughout the line-forming region when $\tau \geq 10$. In the latter pair, on the other hand, τ decreases exponentially with increasing velocity, so the line samples such large optical depths at only very low velocities. This velocity dependence affects line formation outside the core in exactly the same way (cf. Section 2.4).

2.4 A line outside the core

Having explored in detail the geometric effects of continuum emission on line formation in the core, we now introduce a non-emitting, transparent shell around the core, with outer radius r_s, where $r_s > r_c$. In this region there is no continuum emission and line formation occurs in exactly the same way as in `SYNOW`. Therefore, unlike the case discussed in Section 2.3, the line forming region now exists *outside* the core, rather than inside. We include the shell in this model to account for the possibility of intermediate mass elements such as Ca II forming lines at late times above the material which has been burned all the way to the iron-peak.

2.4.1 Intensity for a line outside the core

We must now consider a number of possible ways that the line and a particular ray can interact. First, if the ray has impact parameter $p > r_c$ then it never intersects the core and, regardless of the location of the line resonance point $z_{\rm res}$, the ray's emergent intensity is

$$I_{z_{\rm res}}(p) = S(r[z_{\rm res}])(1 - e^{-\tau}) \tag{2.15}$$

where $S(r)$ is now the source function *outside* the core, given by Equation (2.8), and

$$\tau = \tau(r[z_{\rm res}]). \tag{2.16}$$

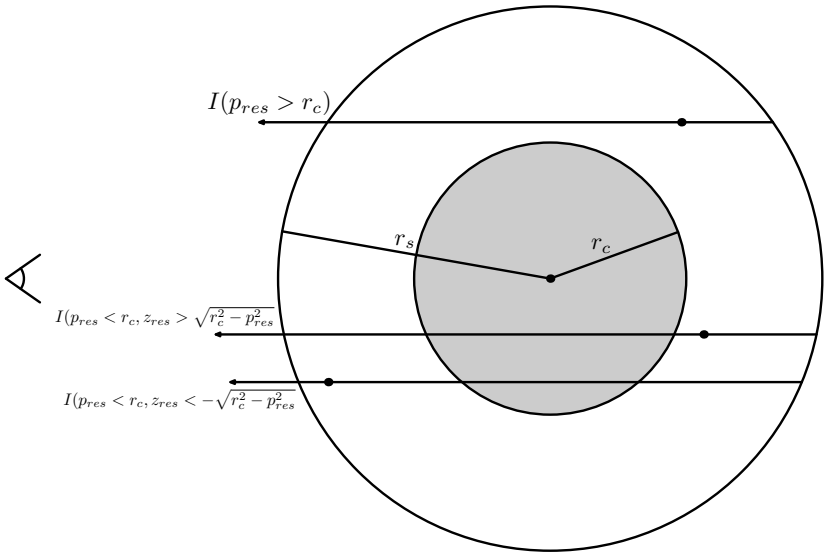

Figure 2.11: The three types of intensity rays for the core+shell configuration.

If the line has $p < r_c$ but $z_{\rm res} < -\sqrt{r_c^2 - p_{\rm res}^2}$, then the line attenuates the continuum ray from the core:

$$I_{z_{\rm res}}(p) = S(r[z_{\rm res}])(1 - e^{-\tau}) + 2(r_c^2 - p^2)^{1/2} e^{-\tau}. \tag{2.17}$$

Finally, if the line has $p < r_c$ and $z_{\rm res} > \sqrt{r_c^2 - p_{\rm res}^2}$, then it does *not* attenuate the core continuum and the emergent intensity is

$$I_{z_{\rm res}}(p) = S(r[z_{\rm res}])(1 - e^{-\tau}) + 2(r_c^2 - p^2)^{1/2}. \tag{2.18}$$

These three cases are shown in Figure 2.11.

2.4.2 Flux for a line outside the core

While F_λ proceeds simply from I_λ in the case $r \leq r_c$, its form is much more complicated in the $r > r_c$ regime. In particular the flux integral takes a unique

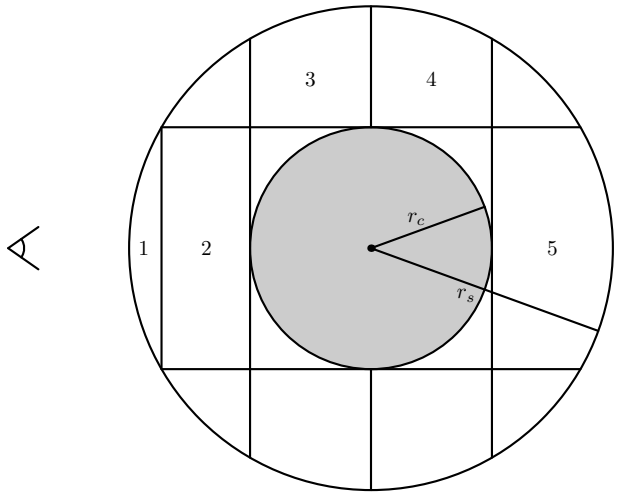

Figure 2.12: The five flux regions in the core+shell configuration.

form in five different regions. We show the five zones in Figure 2.12.

1. $-r_s < z < -(r_s^2 - r_c^2)^{1/2}$

$$\begin{aligned} F_z &= \frac{4\pi}{r_c^2} e^{-\tau} \int_0^{(r_s^2 - z^2)^{1/2}} (r_c^2 - p^2)^{1/2} p dp \\ &+ \frac{4\pi}{r_c^2} \int_{(r_s^2 - z^2)^{1/2}}^{r_c} (r_c^2 - p^2)^{1/2} p dp \\ &+ \frac{2\pi}{r_c^2} (1 - e^{-\tau}) \int_0^{(r_s^2 - z^2)^{1/2}} S(r[p]) p dp \end{aligned}$$

2. $-(r_s^2 - r_c^2)^{1/2} < z < -r_c$

$$F_z = \frac{4\pi}{3} r_c e^{-\tau} + \frac{2\pi}{r_c^2} (1 - e^{-\tau}) \int_0^{(r_s^2 - z^2)^{1/2}} S(r[p]) p dp$$

3. $-r_c < z < 0$

$$\begin{aligned} F_z &= \frac{4\pi}{r_c^2}\int_0^{(r_c^2-z^2)^{1/2}}(r_c^2-p^2)^{1/2}pdp \\ &+\frac{4\pi}{r_c^2}e^{-\tau}\int_{(r_c^2-z^2)^{1/2}}^{r_c}(r_c^2-p^2)^{1/2}pdp \\ &+\frac{2\pi}{r_c^2}(1-e^{-\tau})\int_{(r_c^2-z^2)^{1/2}}^{(r_s^2-z^2)^{1/2}}S(r[p])pdp \end{aligned}$$

4. $0 < z < r_c$

$$F_z = \frac{4\pi}{3}r_c + \frac{2\pi}{r_c^2}(1-e^{-\tau})\int_{(r_c^2-z^2)^{1/2}}^{(r_s^2-z^2)^{1/2}}S(r[p])pdp$$

5. $r_c < z < r_s$

$$F_z = \frac{4\pi}{3}r_c + \frac{2\pi}{r_c^2}(1-e^{-\tau})\int_0^{(r_s^2-z^2)^{1/2}}S(r[p])pdp$$

Figure 2.13 depicts single-line profiles with different values of τ. We first note the resemblance of these line profiles to those of `SYNOW` shown in Figure 2.8. This is not surprising, given that the only difference between the two models is that in `SYNOW` the core is opaque while in the post-photospheric model is it transparent. Both exhibit strong deviations from the continuum flux value, especially in the absorption component. We discussed in Section 2.3 the cause of this near-zero flux in the absorption component of the line.

There is one major difference between the line profiles in Figure 2.8 and Figure 2.13: the flat-topped emission component in the latter. To discern the

source of this plateau in the spectrum, we conduct a geometric analysis similar to that presented in Section 2.3, again studying the limit $\tau \to \infty$. Starting with the resonance plane at the back of the shell, $z = r_s$, we see that as it moves forward toward the observer, its surface area grows, which leads to the flux increase from 6010 Å blueward to 5950 Å in Figure 2.13.

When the resonance plane reaches the back edge of the core and begins to move forward through it, that is, when $0 < z_{\rm res} < r_c$, the core projects onto the plane a central circular region where $\tau = 0$ and continuum emission from the core is unattenuated. The component of the plane which samples the optical depth in the shell is a ring with area

$$A = \pi(r_s^2 - z_{\rm res}^2) - \pi(r_c^2 - z_{\rm res}^2) = \pi(r_s^2 - r_c^2). \tag{2.19}$$

From this equation we see that A is constant when $0 < z_{\rm res} < r_c$; this constancy is the cause of the emission plateau in Figure 2.13.

When $-r_c < z_{\rm res} < 0$, the plane begins to obscure the core, starting at the core's limb, and scatters an increasing amount of the continuum emission out of the observer's line of sight. When $z_{\rm res} < -r_c$ the entire core is obscured and the only emission from the ejecta comes from the source function at $z_{\rm res}$. In the region $-r_s < z_{\rm res} < -r_c$, line formation occurs in exactly the same way as in `SYNOW`, leading to the absorption trough in Figure 2.13 which is almost identical to that of the `SYNOW` profile shown in Figure 2.8.

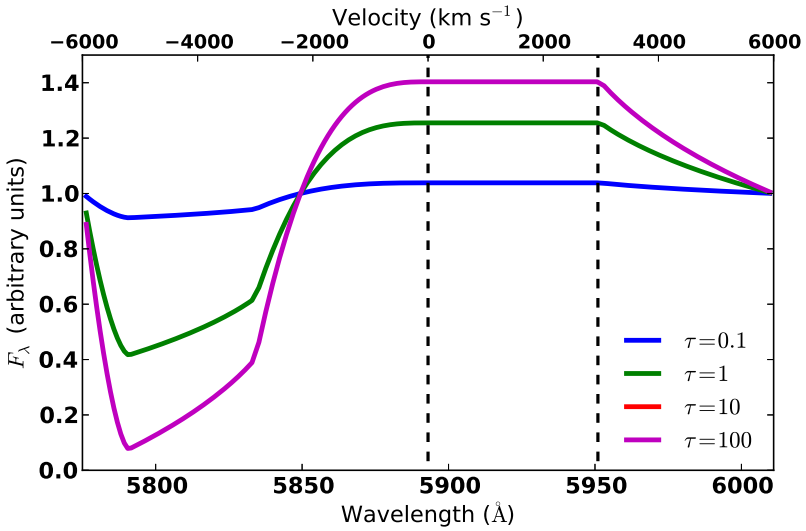

Figure 2.13: Flux for Na I D in the shell, with core velocity 3000 km s^{-1} and outer edge shell velocity 6000 km s^{-1}. The rest wavelength of the line is $\lambda_0 = 5892$ Å, indicated by the left vertical dashed line. The right dashed line indicates the rest wavelength of Na I D redshifted to the back edge of the core, at which point the emission peak forms a plateau. For $r_c \leq r \leq r_s$, $\tau =$ constant and for $r \leq r_c$, $\tau = 0$. The $\tau = 10$ and $\tau = 100$ profiles overlap almost exactly and are indistinguishable in this figure.

The constant-flux emission in the specta in Figure 2.13 is the most distinguishing feature of our post-photospheric model. In Section 2.6 we will consider a nebular line-forming region with a "hole" devoid of line optical depth, and there we will encounter a geometric conspiracy similar to the one presented in this section, leading to similarly flat features in line profiles. We remark in addition that `SYNOW` can produce flat-topped emission features in a spectrum by detaching lines from the photosphere. Thus we conclude that in general a plateau-shaped line emission feature indicates some kind of missing line opacity.

2.5 Two lines in the core

We now study the case of two resonance lines in the core. Understanding the ways in which multiple lines "interact" via their overlapping flux profiles, and in turn being able to identify them individually, is critical to interpreting observed spectra since, in all epochs of a SN, its optical spectrum exhibits severe line blending.

In the resonance-scattering approximation, for any number of lines in the core, the source function of the bluest line always has the single-line form given in Equation (2.7), since there are no bluer photons in the radiation field which can redshift into resonance with it. The second bluest line then interacts only with its bluer neighbor; the third bluest line interacts with its two bluer neighbors; etc. In computational terms this means that one calculates the source function for each line starting with the bluest and moving redward. The details of the calculation are shown in Chapter B.

We first consider the case $v_{\rm core} = 3000$ km s^{-1}, and we hold the optical depths of both lines fixed everywhere in the core, $\tau_B = \tau_R = 1$. We then set the rest wavelength of the blue line to 2850 Å and decrement the rest wavelength of the red line from 3000 Å, where the lines are too far apart in wavelength space to blend in the spectrum, to 2855 Å, where the lines overlap completely. The result is shown in Figure 2.14. In this figure we find that line blending in the post-photospheric case occurs in essentially the same way as in the `SYNOW` case (Jeffery and Branch 1990). Specifically, the absorption component of the red line completely overwhelms the emission of the blue line, and also, when the two lines

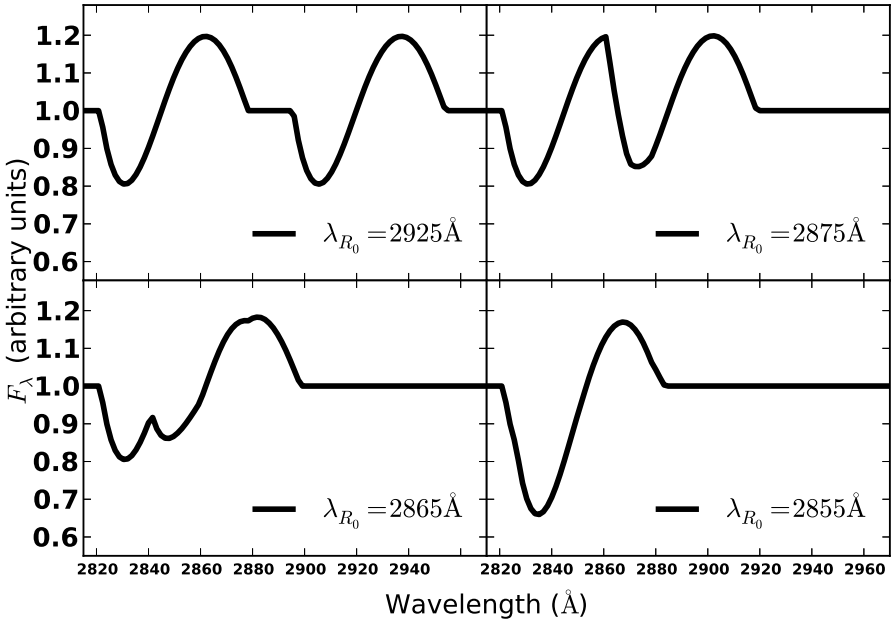

Figure 2.14: Interaction of two lines in the core as they blend together due to Doppler broadening. The rest wavelength of the blue line is fixed at $\lambda_{B_0} = 2850$ Å, while the rest wavelength of the red line moves blueward. The optical depths of both lines are fixed at $\tau_B = \tau_R = 1$.

overlap perfectly (the bottom-right panel of Figure 2.14), the redshifted emission component appears the same as the single-line case, but the absorption is much deeper.

One peculiar feature of Figure 2.14 is that, when the lines overlap only partially, the emission component of the blue line acquires a triangular shape. In fact, in the upper-right panel of that figure, the triangular emission peak is nearly symmetrical. However the abrupt (perhaps unrealistic) drop in τ at the edge of the core in this calculation may somewhat exaggerate this triangular feature.

In this section we have restricted our discussion to the interaction between two lines confined to the core. However, with the introduction of multiple lines, many other types of interactions are possible. As an example, in Section B.2

we construct the geometric framework for the two-line case where both lines are outside the core. However the situation is more complex due to the myriad combinations of line locations as well as their combined interaction with the core and shell.

2.6 Discussion

Much recent work analyzing SNe Ia spectra has focused on the importance of asymmetries (Maeda, Benetti, et al. 2010; Maund, Höflich, et al. 2010; Foley and Kasen 2011; Maeda, Leloudas, et al. 2011; Foley, Simon, et al. 2012). However, the spectra produced by this model illustrate a potentially significant complication in interpreting spectra at late times in SNe Ia, specifically in the interpretation of line emission in the absence of scattering. To illustrate this point we refer to the work of Maeda, Benetti, et al. (2010) and Maeda, Leloudas, et al. (2011), who interpret observed blueshifts and redshifts of Fe lines in nebular spectra as resulting from asymmetric clumps of iron-peak material moving toward and away from the observer, respectively, in the optically thin SN Ia ejecta. This interpretation implies that the explosion of a white dwarf resulting in a SN Ia is itself highly asymmetric, but relies heavily upon the assumption that spectral features at late times arise *only* through forbidden transitions of atomic lines due to the low gas density, and that the resulting emission profiles are distributed roughly symmetrically about the rest wavelength. Indeed, this assumption has become widespread in nebular spectrum synthesis since the pioneering work of Axelrod (1980). However, if an appreciable amount of resonance-scattering

is present at this epoch, our results show that in the presence of significant continuum emission, a perfectly spherically symmetric distribution of matter produces a redshifted emission component. It remains unclear what effect, if any, that resonance-scattering has on the sample considered in Maeda, Benetti, et al. (2010) since the objects in their study were often several hundred days older than the objects we attempted to fit using `SYNOW` in Figure 2.1 and Figure 2.2.

Maund, Höflich, et al. (2010) studied polarization measurements of the objects in Maeda, Benetti, et al. (2010) for which such data were available, and drew similar conclusions as ibid., that is, that asymmetry alone may explain the diversity observed in SNe Ia. The survey in Maund, Höflich, et al. (2010) was biased in that polarization data existed only for SNe with redshifted emission peaks for particular lines of Fe II and Ni II, but nevertheless we note that, at intermediate times, for many features there are multiple possible line identifications, and redshifted emission can result from either optically thin, receding ejecta, or, as shown in Figure 2.7, from spherically symmetric ejecta with large line optical depth. While the very late data (Maeda, Benetti, et al. 2010; Maund, Höflich, et al. 2010) may indeed be showing the inferred asymmetry, our results show that one should indeed be cautious about the epoch of the data when interpreting redshifted emission profiles.

Finally, we consider another significant effect of resonance-scattering at late times in SNe. Studies of late-time line profiles and the imaging of the supernova remnant S Andromeda (Höflich 2003; Motohara et al. 2006; Fesen, Höflich, et al. 2007; Gerardy, Meikle, et al. 2007; Maeda, Benetti, et al. 2010) have lead to the

suggestion that a "nickel hole" exists in at least some SNe Ia. In optically thin media, a central region devoid of line-forming material manifests in a spectrum as a flat-topped emission feature in the spectrum; Höflich, Gerardy, Nomoto, et al. (2004) find just this when studying the [Fe II] $\lambda 16\,440$ line in a spectrum of SN 2003du taken $\sim$ 300 days after explosion, suggesting that ^{56}Fe and therefore ^{56}Ni were absent in the central part of the SN ejecta. However, the IR observations in these studies are quite noisy, and if the same effect could be observed earlier, or in stronger lines, there would be more flux, allowing statistics to be built up on the existence of a nickel hole in SNe Ia, which would provide important constraints on the underlying explosion model.

With this in mind we explore the possibility that one may observe a similar plateau feature inside the glowing core by carving out regions of zero optical depth in a resonance-scattering line. To study this, we return to the core-only model, with velocity 3000 $\mathrm{km\,s^{-1}}$, and set the rest wavelength of a single line in the core to 3000 Å. We then set the optical depth of the line to $\tau = 1$, and proceed to exclude this optical depth from progressively larger portions of the core's central region. The resulting line profiles are shown in Figure 2.15. The classical rounded profile is replaced by a flat profile, but there still exists both an emission peak and an absorption trough. This result corroborates the plateau effects we studied in Section 2.4 — Figure 2.13 already showed that when a region of large line optical depth surrounds a region of zero optical depth, flat-topped components can appear in the spectral line profiles.

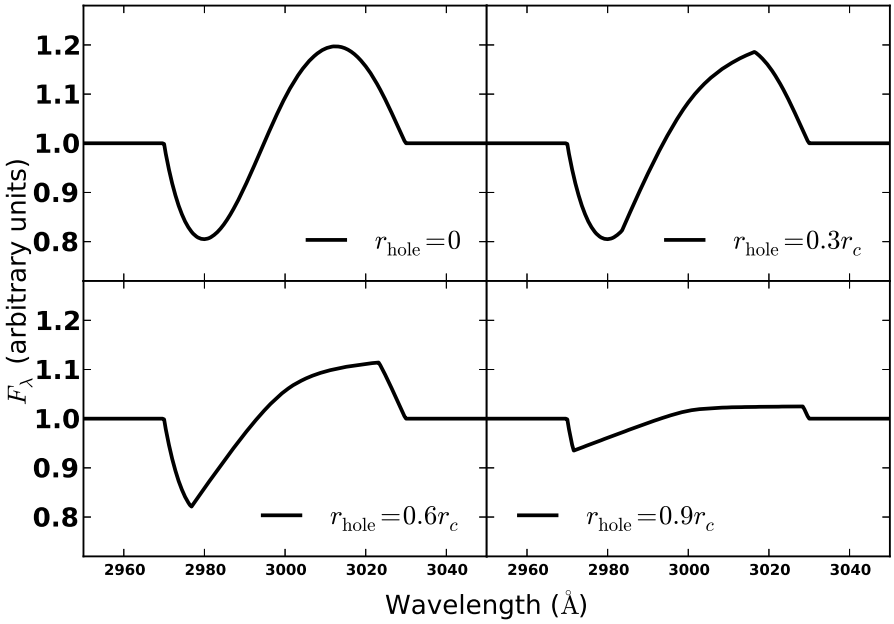

Figure 2.15: A post-photospheric line profile where the line is excluded from the various parts of the inner region of the core. The core has outer velocity 3000 $\mathrm{km\,s^{-1}}$. The optical depth in the region $r > r_{\rm hole}$ is $\tau = 1$, whereas in $r < r_{\rm hole}$, $\tau = 0$. The rounded profile is replaced by a flattened profile, but there is still an emission peak and an absorption trough, both of which become more muted as $r_{\rm hole}$ increases.

2.7 Conclusions

We have presented the geometric framework for a post-photospheric model of a SN, making simple assumptions about its emissivity and source function, in an attempt to explore the effects of resonance-scattering in optically thick lines in SN atmospheres in epochs where such scattering processes are rarely considered. Our model is inspired by and similar to the Elementary Supernova model, but the substitution of a photosphere for a transparent but continuum-emitting core leads to significant differences in line formation. The most noticeable difference is that the emission peak of a line is redshifted from its rest wavelength, even though the model is spherically symmetric. This property may affect the interpretation of SN spectra in post-photospheric phases, when asymmetric effects on line formation become influential.

Our model remains mostly within the geometric confines of the Elementary Supernova model, and choices about its properties different than the ones made here are possible. For example, one may assume that severe line blending in the core creates a pseudo-continuum, leading to a source function in the shell exactly equal to that assumed in `SYNOW`:

$$S = W(r)J,$$

where $W(r)$ is the dilution factor. We have also chosen to parameterize all line optical depths rather than calculating them in any self-consistent manner, e.g.,

by solving rate equations. We believe our choices in these matters have resulted in a level of detail commensurate with the simplicity of this model.

2.8 Acknowledgements

This chapter is reproduced by permission of the American Astronomical Society from the following publication: Friesen, B., E. Baron, D. Branch, et al. (Nov. 2012). "Supernova Resonance-scattering Line Profiles in the Absence of a Photosphere". In: ApJS 203, 12, p. 12

The referee's careful eye vastly improved the content of this work, for which we are grateful. This work was supported in part by NSF grant AST-0707704, and US DOE Grant DE-FG02-07ER41517, and by SFB 676, GRK 1354 from the DFG. Support for Program No. HST-GO-12298.05-A was provided by NASA through a grant from the Space Telescope Science Institute, which is operated by the Association of Universities for Research in Astronomy, Incorporated, under NASA contract NAS5-26555. This research has made use of NASA's Astrophysics Data System.

Chapter 3

Near-infrared line identification in type Ia supernovae during the transitional phase

We present near-infrared synthetic spectra of a delayed-detonation hydrodynamical model and compare them to observed spectra of four normal Type Ia supernovae ranging from day +56.5 to day +85. This is the epoch during which supernovae are believed to be undergoing the transition from the photospheric phase, where spectra are characterized by line scattering above an optically thick photosphere, to the nebular phase, where spectra consist of optically thin emission from forbidden lines. We find that most spectral features in the near-infrared can be accounted for by permitted lines of Fe II and Co II. In addition, we find that [Ni II] fits the emission feature near 1.98 µm, suggesting that a substantial mass of ^{58}Ni exists near the center of the ejecta in these objects, arising from nuclear burning at high density.

3.1 Introduction

SNe Ia radiate primarily at optical wavelengths. However, optical and especially ultraviolet (UV) radiation is sensitive to attenuation by dust along the line of sight to the observer (Cardelli et al. 1989). Furthermore, these bands are extremely crowded regions of the SN spectral energy distribution (SED): generally over 100

lines lie within one Doppler width of one another at any given optical wavelength, with the number approaching 1000 in the UV (Baron, Hauschildt, Nugent, et al. 1996). The NIR bands of a SN Ia SED behave very differently than the UV or optical, having adjacent regions of wildly varying line opacity (Wheeler et al. 1998). This phenomenon allows one to probe the ejecta at a wide range of velocities, providing a unique window to the radiation physics of SNe Ia, which in turn can constrain properties of explosion and progenitor scenarios. Spectroscopic studies of NIR spectra of SNe Ia at both early epochs (e.g., Meikle et al. 1996; Wheeler et al. 1998; Hsiao et al. 2013) and very late epochs (Spyromilio et al. 1992; Bowers et al. 1997; Höflich, Gerardy, Nomoto, et al. 2004; Mazzali, Maurer, et al. 2011) have provided wide-ranging constraints on the distribution of unburned and partially burned nuclear WD material, as well as the explosion energetics and ^{56}Ni mass. Several other studies have focused on a time series of NIR spectra which span from pre- to post-maximum light, e.g., Hamuy, Maza, et al. (2002), Höflich, Gerardy, Fesen, et al. (2002), Marion, Höflich, Vacca, et al. (2003), Marion, Höflich, Gerardy, et al. (2009), and Gall et al. (2012); these studies have generally reached similar conclusions about post-maximum NIR spectra, that they are formed primarily from iron-peak elements such as Fe and Co.

In this work we expand upon these studies by identifying the features in the NIR spectra of four normal SNe Ia during the "transitional" phase, a few months post-maximum light, during which the ejecta are neither photospheric nor entirely nebular. One of these objects is the recent and nearby SN 2014J, discovered by Fossey et al. (2014) in the nearby galaxy M82 approximately one week after

explosion. Early and extensive follow-up campaigns revealed that SN 2014J is a normal SN Ia, but the environment and/or the line of sight to the explosion are highly reddened by dust (Goobar et al. 2014; Zheng et al. 2014; Marion, Sand, et al. 2015). The other three SNe examined in this work are SNe 2001fe (Filippenko and Chornock 2001), 2002bo (Benetti et al. 2004), and 2003du (Gerardy, Höflich, et al. 2004; Höflich, Gerardy, Nomoto, et al. 2004; Anupama et al. 2005; Stanishev et al. 2007; Tanaka et al. 2011). The spectroscopic and photometric properties of these four SNe are summarized in Table 3.1; all four are relatively normal SNe, with the exception of some high-velocity features in SNe 2002bo and 2014J. Because several objects comprise our "time series" of NIR spectra, we do not seek in this work to characterize the time-evolution of any particular spectroscopic feature, as it is difficult to separate the intrinsic variability of the ejecta of each SN from age-dependent effects in a given spectrum. Rather, our purpose is to identify common features in each spectrum, and to infer properties inherent to our entire sample which may provide useful diagnostic tools in the study of larger samples or of a high-cadence time series of NIR spectra of a single object which includes these epochs.

3.2 Observations

We obtained two observations of SN 2014J with TripleSpec, a cross-dispersed infrared spectrograph mounted on the 3.5 m telescope at Apache Point Observatory on 2014 April 8 and 2014 April 11. At this epoch SN 2014J had NIR apparent magnitudes of approximately $J = 12.0$, $H = 10.6$, and $K = 10.8$ (Foley, Fox, et al.

2014). These data are the first of a pilot project to generate a wide-ranging data set of NIR spectra and photometry of nearby ($z \lesssim 0.008$) SNe Ia at post-maximum and late-time epochs using TripleSpec. The observations were made with the 1."1 $\times$ 43."0 slit, yielding resolution $R \sim 3500$ data from 0.95 µm to 2.46 µm, and were obtained using a standard ABBA nod sequence. Observations of a nearby A0V star were obtained immediately after our observations of SN 2014J to facilitate accurate telluric subtraction. Table 3.2 summarizes the details of our observations, including the individual exposure times and total on-source integration times for SN 2014J and our A0V calibrators.

Object	$M_B^{\max}$	Δm_{15}	$v_{\text{Si II, max}}$	Spectroscopic classification
SN 2001fe	—	—	$11,200$	NV
SN 2002bo	-19.41	1.13	$12,800$	HV
SN 2003du	-19.34	1.04	$10,500$	NV
SN 2014J	-19.19	1.11	$11,900$	HV

Table 3.1: Summary of photometric and spectroscopic characteristics of the four SNe Ia studied in this work. $M_B^{\max}$ is the absolute magnitude in the B band at maximum light in B. Δm_{15} is the number of magnitudes by which the object declines in B between maximum light and 15 days layer Phillips (1993). (Photometry of SN 2001fe is unavailable.) $v_{\text{Si II,max}}$ is the velocity of the Si II λ6355 absorption feature at maximum light in B. The spectroscopic classification consists of "normal velocity" ("NV") and "high velocity" ("HV"), based on $v_{\text{Si II,max}}$, as defined in X. Wang et al. (2009); the division between the two regimes is $\sim 11\,800$ km s^{-1}, placing SN 2014J barely in the HV group.

These data were flat-fielded, wavelength calibrated, and extracted using Triplespectool, a modified version of Spextool (Cushing et al. 2004). The data were corrected for telluric features using observations of nearby A0V stars at similar airmass to SN 2014J following the techniques outlined in Vacca et al. (2003). We also performed absolute flux calibration using the A0V telluric stars, following Vacca et al. (ibid.): when combining the individual SN and stellar spectra, we scaled each to the mean computed in high signal-to-noise regions of the spectra. The relative fluxes presented here are unaffected by these processes. Our two SN 2014J observations were obtained at significantly different hour angles and airmasses. As optimal removal of telluric features is achieved by minimizing the angular distance and airmass difference between science and A0V calibrator (ibid.), we utilized different A0V calibrators for our two epochs of observations (see Table 3.2). The spectra have been deredshifted by $v = 203$ km s^{-1} using M82 data from NED[1] and dereddened using $R_V = 1.7$ and $E(B-V) = 1.2$ mag for M82 and $R_V = 3.1$ and $E(B-V) = 0.14$ mag for the Milky Way, following the estimates of Goobar et al. (2014), although the reddening effects of dust from both galaxies are negligible in the NIR.

[1]The NASA/IPAC Extragalactic Database (NED) is operated by the Jet Propulsion Laboratory, California Institute of Technology, under contract with the National Aeronautics and Space Administration.

UT Date	Object	Facility	Exposure time (s)	Total on-source integration time (s)	Airmass
MJD 56755.14	SN 2014J	APO 3.5m/TripleSpec	300	3000	1.25
MJD 56755.17	HD 63586	APO 3.5m/TripleSpec	7	112	1.18
MJD 56758.33	SN 2014J	APO 3.5m/TripleSpec	300	1500	1.59
MJD 56758.36	39 UMa	APO 3.5m/TripleSpec	20	240	1.51

Table 3.2: The mid-exposure UT dates (in Modified Julian Date) for our observations of SN 2014J and corresponding A0V-star calibrators are tabulated, along with the duration of each individual exposure at an ABBA nod position and total on-source integration time are compiled.

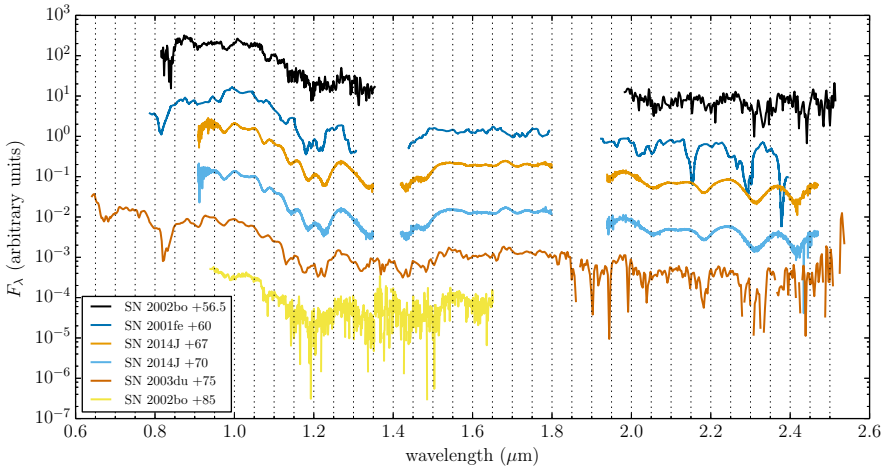

Figure 3.1: NIR spectra of SN 2014J compared with SNe 2001fe, 2002bo, and 2003du at similar epochs. All of the spectra have been deredshifted and dereddened. They have also been multiplied by arbitrary constants to facilitate comparison.

For comparison we plot alongside our SN 2014J spectra four transitional-phase NIR spectra: SN 2001fe at day +60, SN 2003du at day +75, and SN 2002bo at days +56.5 and +85 (Benetti et al. 2004; Marion, Höflich, Gerardy, et al. 2009). The spectra of SN 2002bo were obtained from WISeREP (Yaron and Gal-Yam 2012). All six spectra are shown in Figure 3.1, with the flux of each multiplied by an arbitrary factor to facilitate comparison of spectral features.

3.3 Numerical models

To generate model spectra we used the radiative transfer code `PHOENIX/1D` (e.g., Nugent, Phillips, et al. 1995; Hauschildt and Baron 1999; Lentz et al. 2000; Baron, Bongard, et al. 2006; Baron, Jeffery, et al. 2008), which solves the spherically symmetric, special relativistic radiative transfer equation, correct to all orders in $\mathcal{O}(v/c)$, along with the non-local thermodynamic equilibrium (NLTE) equations

of statistical equilibrium. It also accounts for non-thermal processes such as γ-ray and positron deposition, and includes a complete treatment of line blanketing. Our models contain approximately 100 000 wavelength points. We calculated synthetic spectra of a spherically symmetric delayed-detonation explosion model described in Domínguez et al. (2001), which reproduces the light curves and spectra for core-normal SNe (Höflich, A. M. Khokhlov, et al. 1995; Höflich, Gerardy, Fesen, et al. 2002; Höflich 2006). In this realization, the carbon/oxygen WD is from the core of an evolved 5 $M_\odot$ main-sequence star. Through accretion, this core approaches the Chandrasekhar mass, and an explosion begins spontaneously when the core has a central density of 2.0×10^9 g cm^{-3} and a total mass of 1.36 $M_\odot$. The transition from deflagration to detonation is triggered artificially at a density of 2.3×10^7 g cm^{-3}. The model abundances are shown in Figure 3.2, with ^{56}Ni plotted at $t = 0$ and all other species plotted at $t \to \infty$ such that, e.g., the mass of Fe includes the stable Fe produced at $t = 0$ as well as all of the decayed ^{56}Ni. The explosion produces 0.64 $M_\odot$ of ^{56}Ni and 0.09 $M_\odot$ of stable ^{58}Ni.

We generated a unique synthetic spectrum to correspond to each of the six observed spectra, assuming each SN had a rise time of 15 days. For example, the synthetic spectrum corresponding to the day +67 spectrum of SN 2014J had a homologous expansion time of 82 days. While it is unlikely that all six SNe indeed had rise times of that period, the variation in rise times (likely a few days) should not affect the spectra significantly, given how slowly they evolve at these epochs (Marion, Höflich, Gerardy, et al. 2009). Furthermore, our purpose here is to identify spectral features, not to quantify the time-evolution of a given SN (a

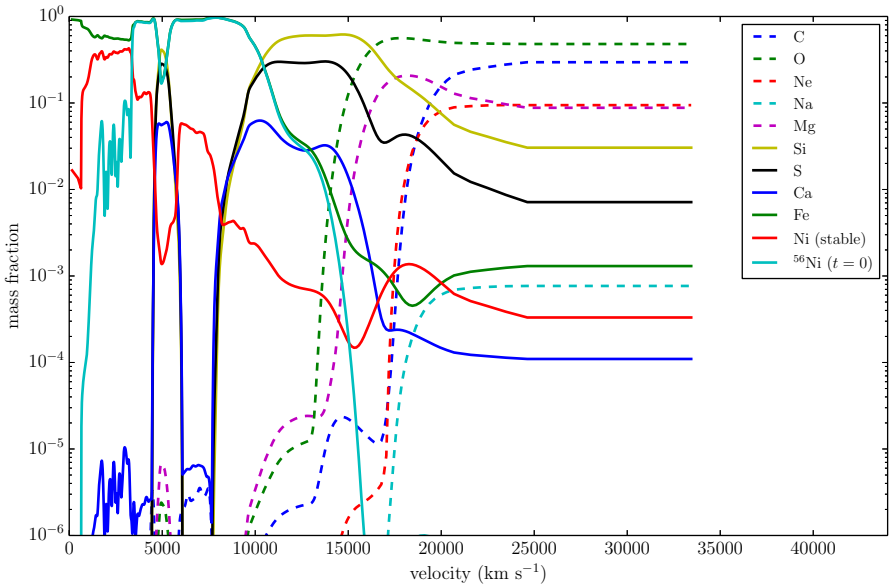

Figure 3.2: Abundances of delayed detonation explosion model used in this work. The ^{56}Ni abundance is plotted at $t = 0$; all others are plotted at $t \to \infty$. The details of the explosion model are reviewed in Section 3.3 and are described in more detail in Domínguez et al. (2001).

difficult task given the dearth of available post-maximum NIR spectra).

Only two significant differences exist between the numerical methods used in previous PHOENIX calculations and the ones presented here. In earlier works, we enforced radiative equilibrium via the modified Unsöld-Lucy algorithm (Hauschildt and Baron 1999), where the total bolometric luminosity in the observer's frame is specified at the outer boundary and the moment equations are integrated to obtain the values of the radiation energy density E and flux F in the comoving frame. Here, we have instead chosen to solve directly the time-independent radiation energy equation (Mihalas and Weibel-Mihalas 1999).

$$\frac{1}{r^2}\frac{\partial}{\partial r}(r^2 F) + \frac{v}{r}(3E - P) + \frac{\partial v}{\partial r}(E + P) = \int_0^\infty d\lambda(4\pi\eta_\lambda - c\chi_\lambda E_\lambda) - \frac{\dot{S}}{4\pi} \quad (3.1)$$

where E, F, and P are the radiation energy density, flux, and pressure, respectively, integrated over all wavelengths; η_λ is the emissivity, χ_λ is the total opacity (absorption and scattering), and $\dot{S}$ is the rate of deposition of non-thermal energy due to radiative decay of ^{56}Ni and ^{56}Co, in the form of γ-rays and positrons. By solving Equation (3.1) directly we do not specify a target luminosity at all. In this way we enforce energy conservation (heating = cooling) and the luminosity is given by the total emission from the entire ejecta which is now powered by radioactive energy deposition (contained in Equation (3.1)). The second difference is that here we have treated all line opacity in full NLTE, rather than parameterizing the opacity for weak lines as discussed in Hauschildt and Baron (1995).

Every term in Equation (3.1) except for $\dot{S}$ is a function of the gas temperature

T. Furthermore, the temperature-dependence of each of these terms is highly nonlinear; therefore this equation requires iteration to solve. To do so, we first choose two successive temperatures guesses for each point in the ejecta.[2] We next iterate the NLTE rate equations, approximate Λ-iteration, and the equation of state until all three are globally converged for the given temperature. Then we apply the secant method to Equation (3.1) to obtain a new temperature guess. Finally, we repeat the latter two steps until Equation (3.1) is satisfied[3] at all points in the ejecta.

3.4 Discussion

The observed NIR spectra shown in Figure 3.1 are fairly similar. However, there are a few interesting differences, including the lines from 1.9 µm to 2.5 µm in SN 2001fe and SN 2003du which are narrow and slightly blueshifted compared to SNe 2002bo and 2014J. In addition, SN 2003du also may exhibit two emission features between 2.3 µm and 2.4 µm (although it is not easy to distinguish this possibility from the noise), while the other three SNe show only a single feature. If it is indeed two distinct features, it is possible that they are present in all three SNe, and that only in SN 2003du are the velocities low enough for them to appear unblended. If this were the case, one might attribute the lower velocity to an

[2]Because the temperature-dependent quantities in Equation (3.1) are obtained iteratively, it is difficult to obtain analytic temperature derivatives which are required for Newton-Raphson iteration. We therefore are relegated to using the secant method, which follows the same procedure as the Newton-Raphson method except with numerical derivatives. The disadvantage of the secant method is that it requires two initial conditions instead of just one. However, as long as both initial guesses are near the correct solution, the converged solution is independent of their values.

[3]We consider a solution "converged" if $\Delta T/T$ is below 1%.

age effect, since SN 2003du's K-band spectrum is the oldest of those shown in Figure 3.1. However, we believe this explanation is unlikely, given how slowly NIR spectra appear to change in the catalog of Marion, Höflich, Gerardy, et al. (2009) (see their Figure 9). An alternative explanation is that the ejecta in the explosion of SN 2003du had a different ^{56}Ni distribution than in SN 2001fe or SN 2014J, or that the velocity gradient of the line-emitting region is narrower in this object than in the others.

Figure 3.3 shows the `PHOENIX` synthetic spectrum compared to SN 2014J at day +67, with the model spectrum scaled such that the predicted flux matches the observation at 1.00 µm. (We apply the same scaling procedure in all comparisons of models and observations.) The calculation used to generate this spectrum included no forbidden lines. Most features in the synthetic spectrum match those in the observed spectrum quite well. The primary shortcoming in the synthetic spectrum is the emission feature at 1.98 µm in SN 2014J which is not reproduced in the model.

In order to determine which atomic species and lines are responsible for which spectral features, we calculate "single-ion spectra" using the prescription of Bongard et al. (2008). The resulting spectra for the most influential ions are shown in Figure 3.4. These single-ion spectra indicate that nearly every feature in the NIR spectrum of SN 2014J can be accounted for with permitted lines of Fe II and Co II. In particular, Fe II dominates the NIR spectrum blueward of 1.50 µm, and Co II dominates the spectrum redward of that point. This result agrees with the conclusions of Branch, Jeffery, et al. (2008), who focused on the optical

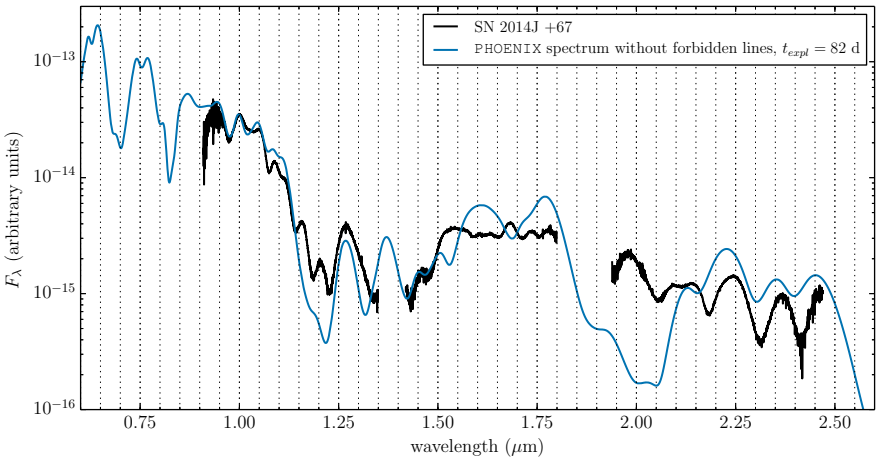

Figure 3.3: PHOENIX spectrum with only permitted lines, with a homologous expansion time of 82 d, compared to SN 2014J at day +67. The synthetic spectrum has been scaled to match the observed flux at 1.00 µm.

wavelengths of normal SN Ia SEDs during the transitional phase, and Gall et al. (2012), who showed that fluorescence of iron-peak and intermediate-mass elements produces much of the post-maximum NIR spectrum in the normal SN 2005cf.

Anticipating the possibility that forbidden lines play a role in NIR spectrum formation at these epochs, we have repeated the calculations of this model, including the forbidden lines in Lundqvist and Fransson (1996) and the NIST Atomic Spectral Database (Kramida et al. 2013) for all species with $Z = 6$ through $Z = 28$ (carbon through nickel). Comparing the permitted-line-only and the permitted-and-forbidden line spectra will then reveal the role that forbidden lines play during these epochs and in these NIR bands. Because changing the atomic data changes the problem that is actually solved (forbidden emission acts as an extra coolant which affects the temperature of the ejecta; Dessart, Hillier, et al. 2014), we re-converged the entire model after adding these extra lines. The

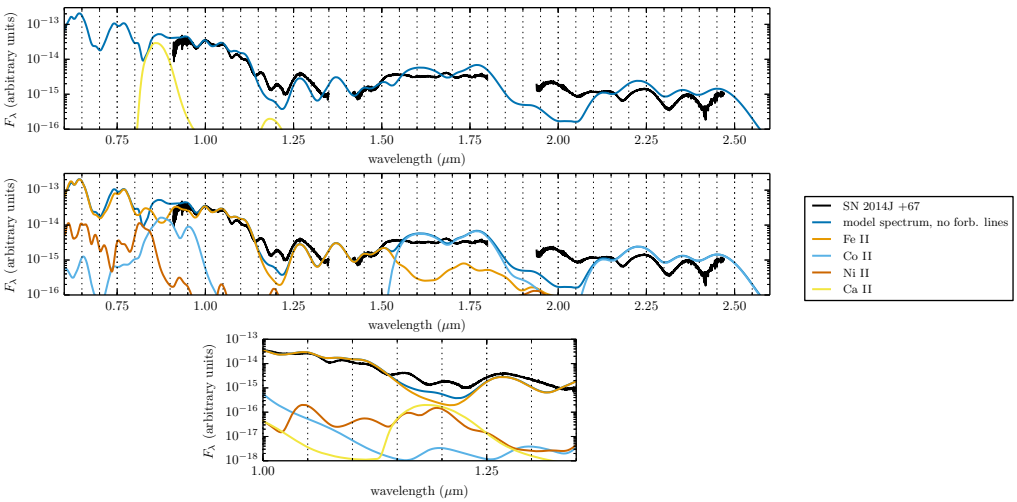

Figure 3.4: Single-ion spectra for the most influential ions in the PHOENIX calculation which did not include forbidden line data, compared to the composite synthetic spectrum as well as to SN 2014J at day +67. The top panel shows intermediate-mass elements; the middle panel shows iron-peak elements; the bottom panel shows an enlarged version of the emission features at 1.15 µm and 1.2 µm, which likely arise due to a combination of several ions. Most features blueward of 1.50 µm are fit with permitted Fe II, while most features redward of that point are fit with permitted Co II. The emission feature at 1.20 µm may be due to Ca II. Permitted lines alone appear unable to fit the emission at 1.98 µm.

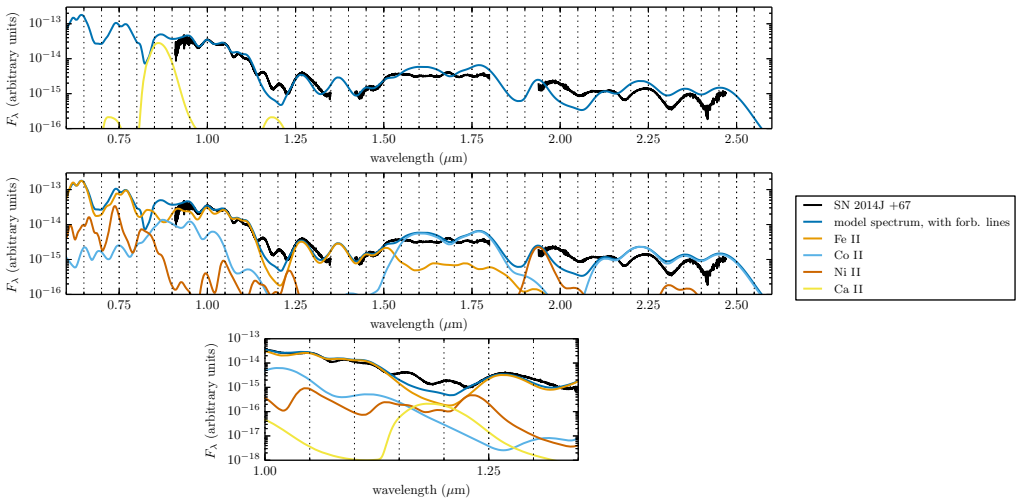

Figure 3.5: Single-ion spectra for the most influential ions in the PHOENIX calculation which included forbidden line data, compared to the composite synthetic spectrum as well as to SN 2014J at day +67. The top panel shows intermediate-mass elements; the middle panel shows iron-peak elements; the bottom panel shows an enlarged version of the emission features at 1.15 µm and 1.2 µm, which likely arise due to a combination of several ions. As in Figure 3.4, most features are best fit by permitted Fe II and Co II. The feature at 1.15 µm appears mostly due to Co II and Ni II. Ca II remains the most likely candidate for the emission at 1.20 µm. The emission at 1.98 µm is due to [Ni II], from stable ^{58}Ni.

resulting spectrum, along with the corresponding single-ion spectra, is shown in Figure 3.5. We also show the corresponding temperature structure $T(v)$ for both models in Figure 3.6 in order to illustrate the cooling effects of forbidden lines. We calculated a synthetic spectrum corresponding to each of the six observed spectra, which together are plotted in Figure 3.7. The addition of forbidden lines does lower the temperature, as discussed in Dessart, Hillier, et al. (2014), but the effect is fairly small, even at this epoch.

The few features which Fe and Co alone do not produce, merit additional scrutiny. These include the emissions at 1.15 µm, 1.20 µm, and 1.98 µm. We discuss identifications of each of these below.

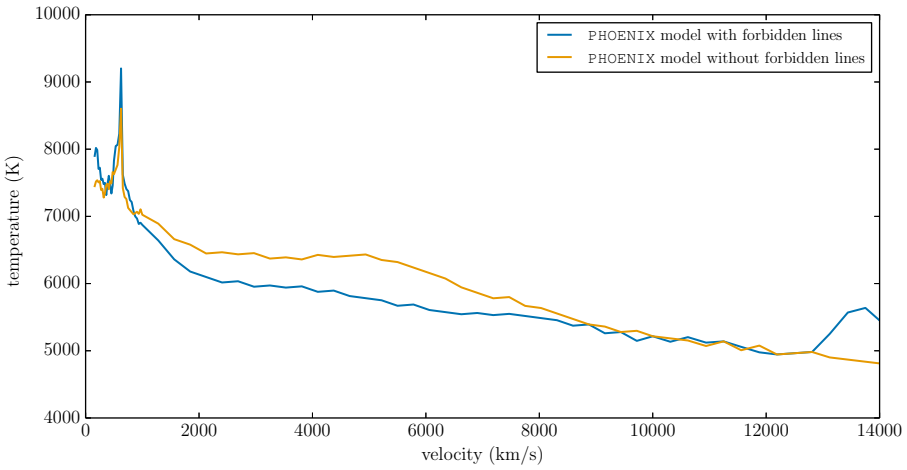

Figure 3.6: Converged temperature structures for the models with (blue) and without (orange) forbidden lines. These lines act as coolants and tend to lower the temperature (ibid.).

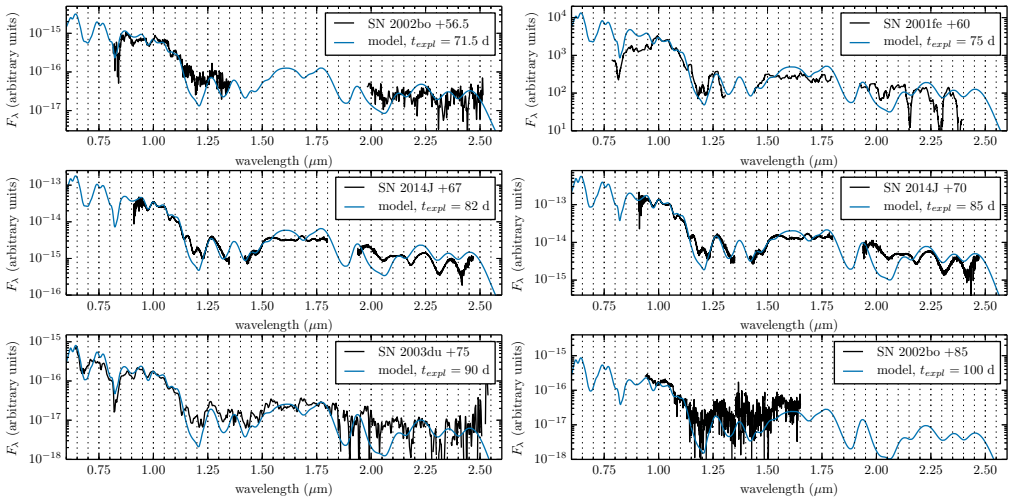

Figure 3.7: PHOENIX spectra with forbidden lines compared to all observed SN spectra in this work. The homologous expansion time for each synthetic spectrum was 15 days, such that, e.g., the model spectrum corresponding to SN 2001fe +60 had an expansion time of 75 d.

3.4.1 The 1.15 µm emission

Figure 3.4 suggests that the emission at 1.15 µm could be due to a combination of Fe II and Ca II, Mn II, and Ni II. Our model atoms, comprised mostly from the sources listed in Hauschildt and Baron (1995) and Short et al. (1999), predict 56 Ni II lines, 7 Ca II lines, and 30 Fe II lines, all within the range 1.14 µm − 1.16 µm; more detailed level population analysis would be required to identify which of these is forming the emission seen in the single-ion spectra. That the composite synthetic spectrum does not reproduce these features of the intermediate mass elements very well is possibly due to deficiencies in the hydrodynamical model or in the gas temperature calculation.

Adding forbidden lines to the calculation complicates the identification of this emission. Figure 3.5 shows that the strongest components at that wavelength after Fe II are now Co II and Ni II, followed by Ca II. Because the composite `PHOENIX` spectrum does not fit that feature very well, it is difficult to say which of these is responsible.

3.4.2 The 1.20 µm emission

In the permitted-line-only spectrum (Figure 4), the emission near 1.20 µm is likely due to a blend of Fe II lines (there are 38 within in the range 1.19 µm − 1.21 µm), Ca II, (there are 6 within the same range), and Ni II (45 lines). As with the 1.15 µm feature, inclusion of forbidden lines complicates identification of this emission. A number of Ni II lines strengthen at nearby wavelengths, but Ca II

remains the strongest component after Fe II.

3.4.3 The 1.98 µm emission

No ion in the permitted-line-only spectrum in Figure 3.4 appears able to reproduce the emission at 1.98 µm. However, addition of forbidden line data produces a strong emission feature in the synthetic spectrum near that wavelength. Figure 3.5 indicates that the emission is due to [Ni II], which we identify as λ1.939 µm. This emission feature produced in the synthetic spectrum is too blue by about 0.5 µm compared to the corresponding feature in SN 2014J (Figure 3.5). Curiously, this shortcoming is repeated in all of the other SNe in our sample (see Figure 3.7). The spectral coverage of SN 2002bo at both day +56.5 and day +85 unfortunately does not span this region and so we cannot study the influence of [Ni II] in that object. An explosion model which leaves the ^{58}Ni more concentrated at the center may cause the nickel emission to shift redward slightly, providing a better match to the three SNe Ia with available spectral coverage studied in this work.

This [Ni II] emission appears in our SN Ia sample to be consistently redward of its appearance in our models. In addition, its location in our model spectra does not change over the 30 day time frame spanned in this work: the emission center is at 1.94 µm, very near the center of the line rest wavelength. It is possible that the systematic redshift of this feature in our sample of observations is due to asymmetrical explosions combined with a line-of-sight effect, as Doppler shifts of optically thin emission lines are sensitive to hydrodynamical asymmetries (Maeda, Benetti, et al. 2010). If asymmetry is indeed the explanation for this observed

redshift, then this feature may possess great utility as a probe of asymmetry at quite early epochs of a SN Ia, assuming a complete and high-quality series of NIR spectra can be obtained.

Given the model age of $t_{\rm expl} = 82$ days, the radioactive ^{56}Ni, with a half-life of ~ 7 days, has all but disappeared. Therefore the [Ni II] which produces the emission feature at this epoch (the feature is present in varying degrees in all SNe in Figure 3.1 except SN 2002bo, which lacks the necessary spectral coverage) must instead be a stable isotope, specifically ^{58}Ni, which is a product of high-density nuclear burning (Thielemann et al. 1986; Iwamoto et al. 1999). The [Ni II] emission in the series of model spectra shown in Figure 3.7 exhibits similar behavior to, e.g., the [Fe II] and [Fe III] lines which appear in optical spectra in the nebular phase (e.g., Leloudas et al. 2009), strengthening as the optical depth of the inner regions of the ejecta decreases and more of the central ^{58}Ni is exposed.

Although the wavelength of the [Ni II] emission in Figure 3.7 does not change over the 30 days spanned by the models, it does strengthen noticeably. We estimate then that a series of moderate-cadence (periods of ~ 20 days) NIR observations of individual SNe Ia during these epochs would provide the information necessary to confirm or refute this identification of ^{58}Ni in this particular hydrodynamical model. (Observations with longer periods would also resolve the strengthening of this emission, but may be unable to determine the time scale over which it evolves.) They would likely also allow models to constrain the amount of ^{58}Ni produced in the explosion, since the strength of the [Ni II] emission should vary with the mass of ^{58}Ni. (In this particular model the mass ratio of stable ^{58}Ni to radioactive

^{56}Ni is $\sim 0.15 : 1$, a typical value for delayed-detonation explosion models.) If the ^{58}Ni identification is correct, observations with such a cadence would be able to track the Doppler shift of this feature (or lack thereof), thereby constraining its velocity extent. However, given this emission feature's close proximity to a heavily polluted telluric region, the sites for such observations would need to be selected carefully, i.e., at high elevation. SNe Ia at higher redshift would exhibit a lower signal-to-noise ratio, but this emission feature in those objects would be less susceptible to telluric contamination.

Marion, Sand, et al. (2015) showed that the layered structure apparent in the early optical and NIR spectra of SN 2014J is consistent with a delayed-detonation explosion model. In addition, Churazov, Sunyaev, Isern, Knödlseder, et al. (2014) found that the mass and distribution of radioactive ^{56}Ni in SN 2014J is consistent with a near-Chandrasekhar-mass explosion, consistent with our results. Sub-Chandrasekhar explosion models tend to underproduce neutron-rich elements such as ^{58}Ni (Seitenzahl, Cescutti, et al. 2013), and so the NIR [Ni II] spectral signatures presented here may provide useful proxies for diagnosing near-Chandrasekhar-mass explosions.

3.5 Conclusions

We have presented NIR synthetic spectra of a SN Ia delayed-detonation hydrodynamical model at epochs spanning from $t_{\rm expl} = 71$ days through $t_{\rm expl} = 100$ days, corresponding roughly to the ages of the NIR spectra of SNe 2001fe, 2002bo, 2003du, and 2014J spanning from days +56.5 through +85, which at these epochs

are undergoing the transition from the photospheric to nebular phase. We found that our model reproduces most features in the NIR spectrum with permitted lines of Fe II and Co II, confirming the results of Branch, Jeffery, et al. (2008) and Gall et al. (2012). Only a few other species contribute appreciably to the NIR spectrum, including Ni II, Co II, and Ca II at 1.15 µm, and Ca II and possibly Ni II at 1.20 µm. The emission at 1.98 µm seen in three of the four SNe Ia studied here is the only feature which arises from forbidden lines in our model; it is due to forbidden lines of [Ni II]. That the emission is so strong indicates a significant mass of stable ^{58}Ni in the ejecta (our model has 0.09 $M_{\odot}$), produced during the early stages of the explosion of the WD progenitor. The evidence for [Ni II] lines implies burning at high density, suggesting that the progenitors of these three SNe Ia ignited at nearly the Chandrasekhar mass.

3.6 Acknowledgements

This chapter is reproduced by permission of the American Astronomical Society from the following publication: Friesen, B., E. Baron, J. P. Wisniewski, et al. (Sept. 2014). "Near-infrared Line Identification in Type Ia Supernovae during the Transitional Phase". In: ApJ 792, 120, p. 120.

We are grateful to the referee for a thoughtful review that significantly improved the quality of this work. We also thank Ivo Seitenzahl for pointing out an error in our model's nucleosynthesis properties. This research has made use of NASA's Astrophysics Data System and the Weizmann Interactive Supernova Data Repository (WISeREP), and is based on observations obtained with the

Apache Point Observatory 3.5 m telescope, which is owned and operated by the Astrophysical Research Consortium. This work has been supported in part by support from NSF grant AST-0707704 and by support for programs HST-GO-12298.05-A, and HST-GO-122948.04-A provided by NASA through a grant from the Space Telescope Science Institute, which is operated by the Association of Universities for Research in Astronomy, Incorporated, under NASA contract NAS5-26555. This research used resources of the National Energy Research Scientific Computing Center (NERSC), which is supported by the Office of Science of the U.S. Department of Energy under Contract No. DE-AC02-05CH11231 and the Hchstleistungs Rechenzentrum Nord (HLRN). We thank both these institutions for a generous allocation of computer time.

Chapter 4

Late-time optical and UV spectroscopy of SN 2011fe

In chapter Chapter 3 we presented synthetic spectra calculated with PHOENIX at moderately late times in SNe Ia – a few months post-maximum light. The results indicated that many of the atomic and radiative processes which shape maximum-light spectra continue to influence spectrum formation during the transitional phase. We also found that the Unsöld-Lucy temperature correction scheme, which produces stable and reliable enforcement of radiative equilibrium at early epochs, is less reliable in these epochs and tends to give spurious results. As a result, we implemented a different scheme to calculate the gas temperature which was less sophisticated – an independent root-find in each layer of the model to solve the radiation energy equation directly – but nevertheless yielded synthetic spectra which matched observations well.

Spurred by these encouraging results, we explored further applications of this and other temperature correction procedures to spectral models at even later times, focusing in particular on comparisons to SN 2011fe. This SN Ia was discovered on 2011 August 24, only 11 hr after explosion (Nugent, Sullivan, et al. 2011). It is among the nearest (~ 6.9 Mpc) and youngest (< 1 d) SNe Ia ever discovered. Extensive spectroscopic and photometric studies of SN 2011fe indicate that it is "normal" in nearly every sense: in luminosity, spectral and color

evolution, abundance patterns, etc. (Parrent, Howell, et al. 2012; Richmond and H. A. Smith 2012; Röpke, Kromer, et al. 2012; Vinkó et al. 2012; Munari et al. 2013; Pereira et al. 2013). Its unremarkable nature coupled with the wealth of observations made over its lifetime render it an ideal laboratory for understanding the physical processes which govern the evolution of most SNe Ia. Indeed, these data have allowed observers to place numerous and unprecedented constraints on the progenitor system of a particular SN Ia (e.g., W. Li et al. 2011; Nugent, Sullivan, et al. 2011; Bloom et al. 2012; Chomiuk et al. 2012; Horesh et al. 2012; Margutti et al. 2012).

Equally as information-rich as the spectra taken at early times are those taken much later, when the SN's photosphere has receded and spectrum formation occurs deep in the SN core. For example, Shappee et al. (2013) used these spectra to constrain further the progenitor system of SN 2011fe, namely that the amount of hydrogen stripped from the putative companion must be $< 0.001\ M_{\odot}$. To explore the physics of late-time spectrum formation more thoroughly, we obtained optical spectra of SN 2011fe at days +100, +205, +311 (J. Parrent, priv. comm.), +349, and +594 (P. Nugent, priv. comm.). The observations are shown in Figure 4.1. We also obtained an ultraviolet spectrum with *Hubble Space Telescope* at day +360 (GO 12948; PI: R. Thomas). This latter observation consisted of ten orbits, the first nine using the STIS/NUV-MAMA configuration, and the last with the STIS/CCD G430L and G750L configurations. The data from one of the NUV-MAMA orbits was unrecoverable, and so the spectrum, presented in Figure 4.2, is a co-add of the nine remaining observations.

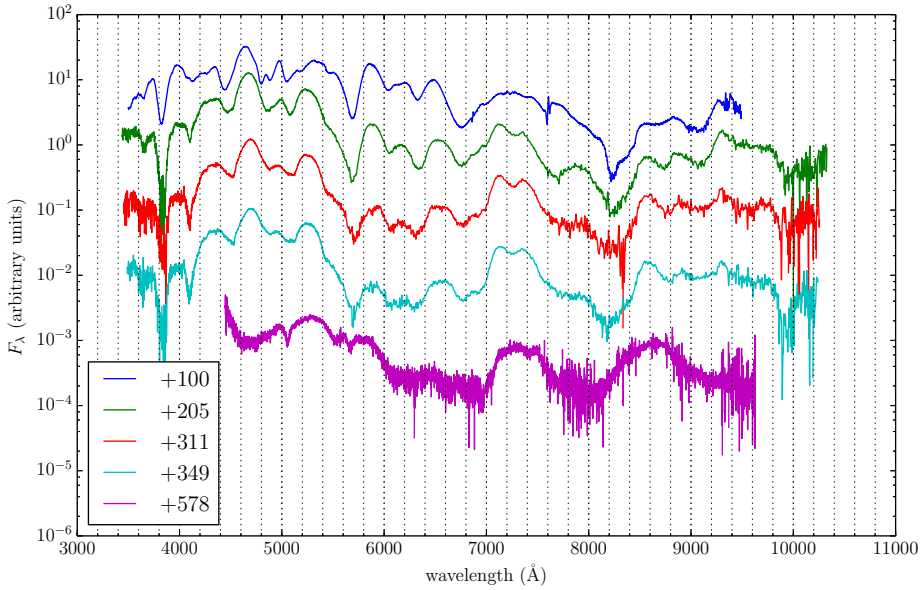

Figure 4.1: Five optical spectra of SN 2011fe used in this work. The fluxes are scaled by arbitrary values in order to facilitate spectral feature comparisons.

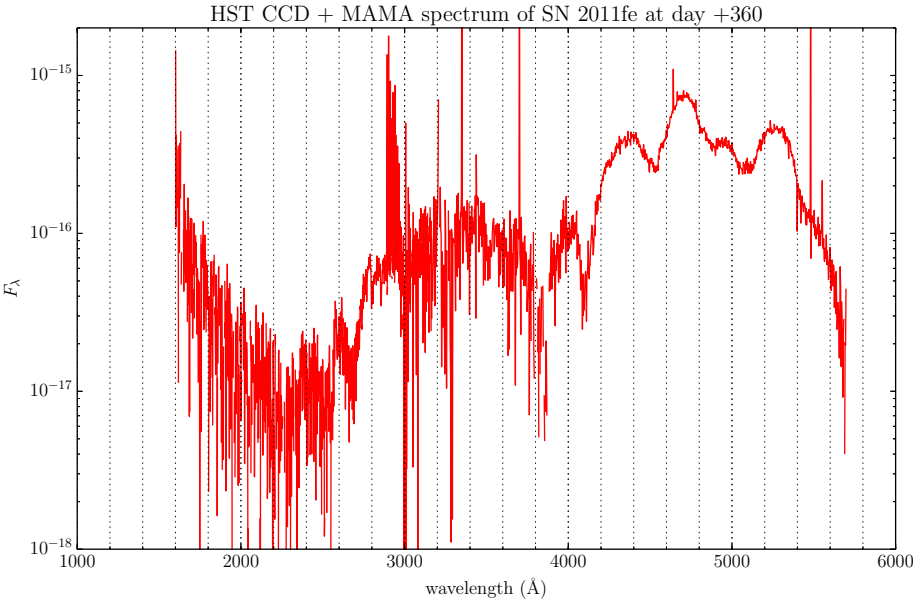

Figure 4.2: UV spectrum of SN 2011fe at day +360 taken with *Hubble Space Telescope*. The flux is scaled arbitrarily to facilitate spectral feature comparison.

To analyze these spectra we performed a series of spherically symmetric radiative transfer calculations using the general-purpose code PHOENIX. We used both the DD explosion model of Domínguez et al. (2001) (the same model used in Friesen, Baron, Wisniewski, et al. 2014), as well as a pair of angle-averaged pulsating reverse detonation (PRD) models from Bravo and García-Senz (2006), Baron, Jeffery, et al. (2008), Bravo and García-Senz (2009), and Bravo, García-Senz, et al. (2009). The PRD explosion model is a response to some of the problems with attempting to induce a detonation in an unconfined domain, i.e., from an outward-moving deflagration flame in a WD (Niemeyer 1999). The "pulse" consists of a weak initial deflagration which burns $\sim 0.1\ M_\odot$ of C/O to iron-peak elements, which rise to the WD surface while cold C/O fuel falls inward, leading to a composition inversion. The deflagration eventually quenches and does not unbind the star. Instead, the central $\sim 1.0\ M_\odot$ of unburned C/O forms a hydrostatic "core" onto which the outer material begins to fall after the flame quenches; this infalling material forms a spherical accretion shock, compressing the C/O fuel. Eventually the C/O at Lagrangian mass $\sim 0.1\ M_\odot$ compresses enough to launch a detonation wave, which sweeps azimuthally around the inner core and ultimately outward to unbind the star. A simultaneous rarefaction wave sweeps through the innermost region of the WD, and the expansion quenches the detonation, leaving $\sim 0.1\ M\odot$ of unburned C/O near the center.

The two PRD models considered in this work differ from each other chiefly in the amount of material burned during the deflagration phase, with one producing

0.14 $M_\odot$ of nuclear ash, and the other 0.18 $M_\odot$.[1] As discussed in Bravo, García-Senz, et al. (2009), a deflagration which burns more mass tends to result in a weaker detonation, since the WD has more time to expand before the detonation triggers. As a result, the model `PRD14` produces more ^{56}Ni (a detonation product) than does `PRD18`. Late-time spectral analysis of the DD and PRD models provides significant constraints on the innermost regions of the explosion models, since the abundance distributions in these regions are quite different among the different models.

The abundance distributions of the two PRD models are shown in Figure 4.3 and Figure 4.4. The corresponding abundances for the DD model are shown in Figure 2 of Friesen, Baron, Wisniewski, et al. (2014). We compare the aggregate yields for the most abundant species in all three models in Table 4.1. PRDs differ from DDs in their increased degree of mixing of the ejecta, as well as having a large amount of iron-peak elements (both stable and radioactive) at high velocity. Bravo, García-Senz, et al. (2009) also add a cap of He to the surface of the WD prior to explosion, emulating material recently accreted from the companion star. Some of this He is mixed inward during the explosion, but much of the He in the final composition of the ejecta forms during the detonation phase, which produces mostly ^{56}Ni and ^{4}He. In addition, PRDs leave a substantial mass of unburned C/O, up to ~ 0.1 $M_\odot$. More details of this class of explosion model are provided

[1]We highlight the change in model designations among these publications. The model introduced in Bravo and García-Senz (2006) is designated `PRD6` in Baron, Jeffery, et al. (2008) and `PRD18` in Bravo, García-Senz, et al. (2009). Similarly, the model called `PRD5.5` in Baron, Jeffery, et al. (2008) is called `PRD14` in Bravo, García-Senz, et al. (2009). In this work we use the most modern designations, given in Bravo, García-Senz, et al. (ibid.), which describe the amount of material burned during the deflagration phase.

	PRD14	PRD18	DD
C	0.061	0.101	0.009
O	0.105	0.149	0.065
Ne	0.010	0.015	0.004
Mg	0.025	0.027	0.018
Si	0.118	0.102	0.228
S	0.055	0.052	0.126
Ar	0.011	0.011	0.025
Ca	0.010	0.011	0.025
Cr	0.005	0.007	0.0005
Mn	0.001	0.002	0.020
Fe ($t \to \infty$)	0.878	0.815	0.739
Ni ($t \to \infty$)	0.054	0.046	0.086
^{56}Ni ($t = 0$)	0.810	0.770	0.643

Table 4.1: Aggregate abundances for the three explosion models tested in this work.

in Bravo and García-Senz (2006, 2009) and Bravo, García-Senz, et al. (2009).

For the spectral comparisons performed below, it is important also to note that hydrodynamical structure of the PRD models used in the PHOENIX radiative transfer calculations presented here did not include stable ^{58}Ni. As a result, there is essentially no Ni present at all at the epochs considered in this work, since the radioactive ^{56}Ni has undergone ~ 19 half-lives by day +100. However even in the DD model which has several 0.1 $M_\odot$ of stable ^{58}Ni, there is only one strong Ni line in any of the optical synthetic spectra, namely the forbidden line [Ni II] λ7377 Å. Other than this feature, then, we expect the comparisons between the models to be "fair."

4.1 Smoothing the UV spectrum of SN 2011fe from *HST*

Although the optical spectra of SN 2011fe at late times have high signal-to-noise (thanks to the close proximity and the nearly unreddened line of sight), the UV

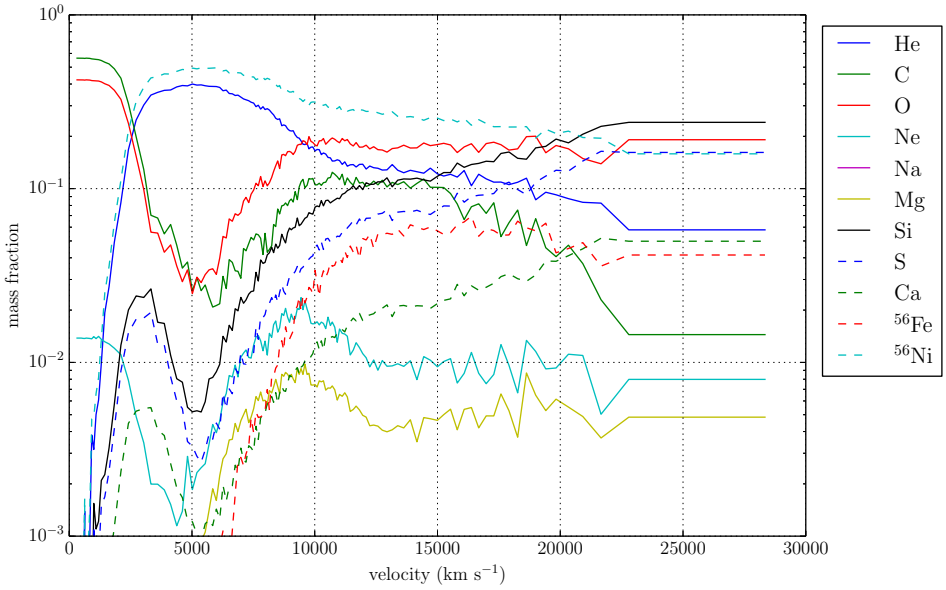

Figure 4.3: Angle-averaged abundances of the PRD model `PRD14` of Bravo, García-Senz, et al. (2009). All abundances are plotted at $t = 0$.

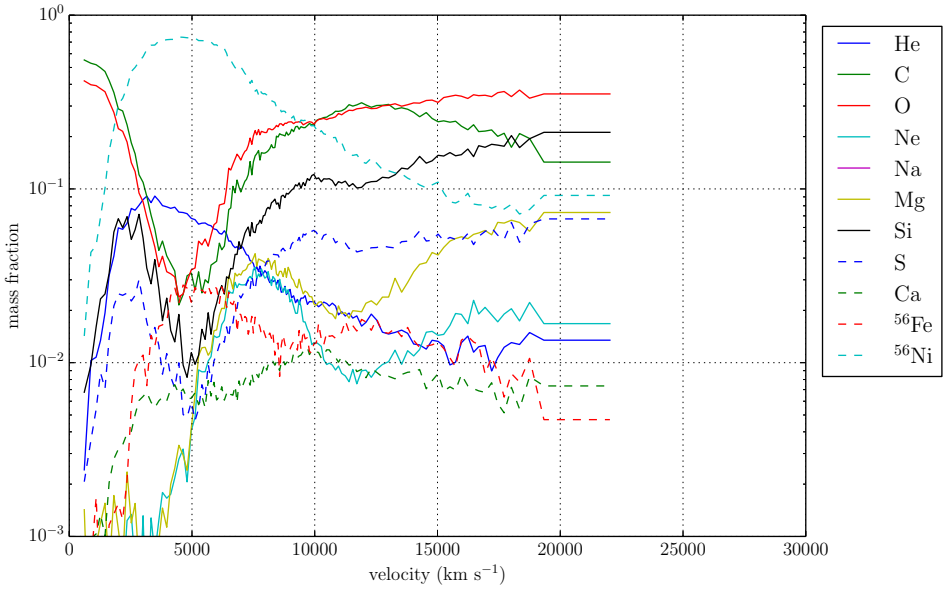

Figure 4.4: Angle-averaged abundances of the PRD model `PRD18` of Bravo, García-Senz, et al. (2009). All abundances are plotted at $t = 0$.

spectrum from *HST* is much noisier. It is desirable to extract as much signal as possible, especially since there appears to be a significant amount of detailed structure in the spectrum. A common method for smoothing noisy spectra is to use convolution window functions, such as moving-average ("boxcar") smoothing. To evaluate the smoothed value at point i, one chooses a window length N and then calculates the average value of the noisy data points which straddle point i:

$$f'_i = \frac{1}{N} \sum_{j=i-N/2}^{i+N/2} f_j \tag{4.1}$$

where f represents the noisy data and f' is the smoothed data. The optimal window length varies sensitively with the behavior of the kernel data being smoothed. For example, in Figure 4.5 we show the effects of different convolution window sizes on the smoothed UV spectrum of SN 2011fe. For the shorter convolution window lengths, boxcar smoothing retains much of the noise and does not improve much on the original spectrum. For longer window lengths, it smears out too much of the signal.

There exist alternative methods of smoothing noisy data. A particularly creative one is presented in Marion, Höflich, Gerardy, et al. (2009), which consists of applying a low-pass filter (Sedra and K. Smith 2009) to the signal. The motivation for this approach is the notion that the "real" physical features in SN Ia spectra are broad, while most noise in the spectrum is narrow. Therefore, if one can suppress the high-"frequency" features (the noise), what will remain will be the pure signal from the SN. To accomplish this task, one calculates the power

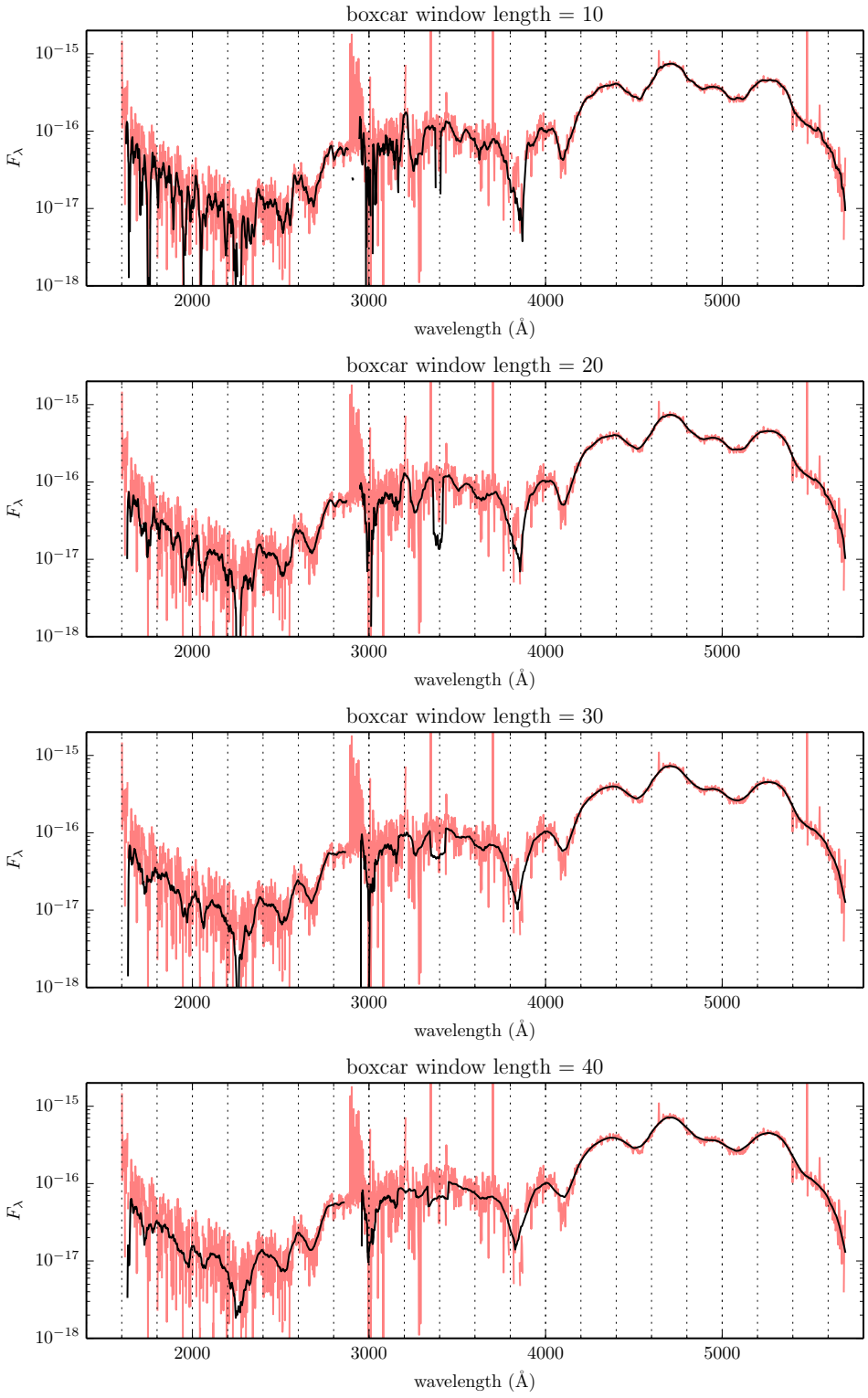

Figure 4.5: Behavior of boxcar smoothing as a function of window length for the UV spectrum obtained with *HST*. The red spectrum is the unsmoothed data, and the blue spectrum is smoothed with the boxcar method.

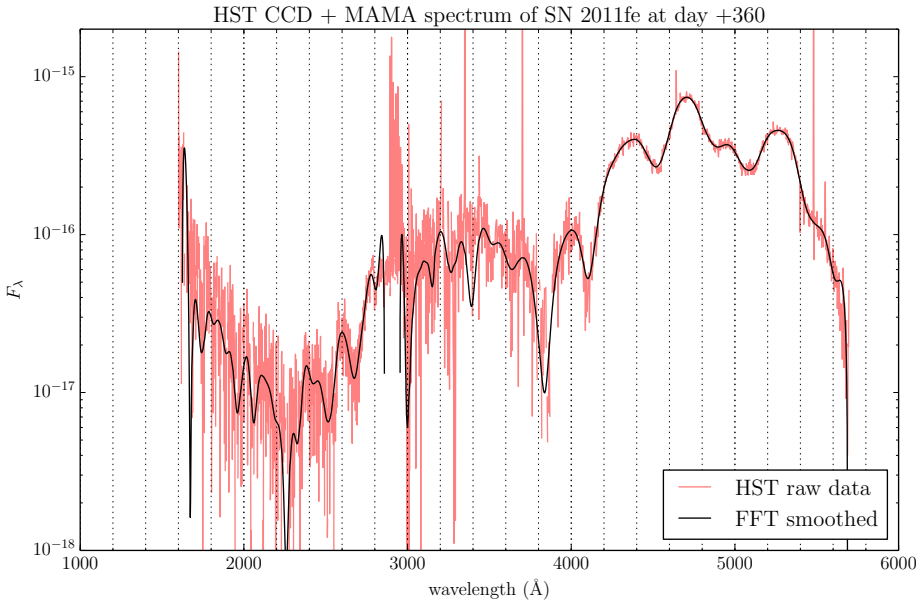

Figure 4.6: Smoothed spectrum using the low-pass filter technique outlined in Marion, Höflich, Gerardy, et al. (2009).

spectrum of the original spectrum using a Fourier transformation, suppresses the power spectrum at all high "frequencies" in which information is deemed to be noise, and applies an inverse Fourier transformation to recover the smoothed spectrum. The resulting smoothed spectrum for the *HST* UV spectrum presented above is shown in Figure 4.6. Considerably more structure in the UV is recovered, especially at the bluest wavelengths, than with the boxcar method, although it is in some places still difficult to pick out the signal pattern.

A third smoothing technique is that of Savitzky and Golay (1964). Like the boxcar method, it uses a moving "window" of width N of adjacent abscissae. However, instead of simply averaging the ordinates within this window as in the boxcar method, this procedure fits a nth-order polynomial to the ordinates within the window by minimizing the least-squares residuals between the polynomial and

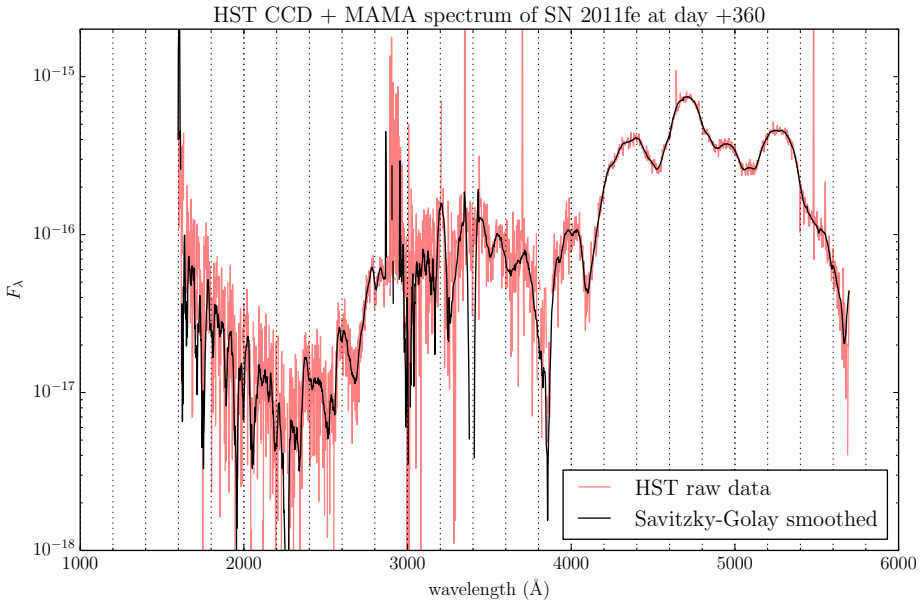

Figure 4.7: Smoothed spectrum using the filtering technique described in Savitzky and Golay (ibid.).

the data. The only constraint on the polynomial order n is $n \leq N - 2$. In general, decreasing the window width and increasing the fitting polynomial order capture more of the noise in the signal, while a large window and a low-order polynomial suppress it, although they tend to suppress the signal as well. An example of the Savitzky-Golay filter applied to the *HST* spectrum is shown in Figure 4.7. This particular filter used a window length of 31 points and a polynomial order of $n = 3$.

There exists no objective, quantitative way to distinguish the "best" smoothed spectrum, as all smoothing methods destroy information while trying to glean the weak signal from the noise. The goal is destroy as little "useful" information as possible in the process. One can in principle employ a quantitative metric such as the χ^2 value between the smoothed and unsmoothed spectra, but this measure is

agnostic to the underlying physics which form the spectra; if uninteresting parts of the spectrum are easily smoothed but other, more information-rich features are lost, then the smoothing algorithm is not useful, even if it yields a low χ^2 value. It is thus the prerogative of the individual to decide this for himself; in the work presented here we have chosen the low-pass filter technique to smooth the UV spectrum of SN 2011fe.

4.2 Previous interpretations of late-time spectra of SNe Ia

As discussed in Section 1.1.4, it is generally believed that the P Cygni features which characterize maximum-light spectra of SNe Ia are absent at late times. Kirshner and Oke (1975) argued that, since the continuum flux is so weak compared to emission features at these late epochs (see, e.g., their Figure 2), such emission does not arise from resonance-scattering processes which form the P Cygni profiles that characterize early SN Ia spectra, because there are not enough photons to scatter into the line. Instead, the low gas temperature and low gas density in the ejecta conspire to excite atoms via collisions with free electrons to only their lowest several excited states, with energies of only a few eV. Most of these levels are metastable and emit photons via forbidden transitions to de-excite back to the ground state. These transitions then manifest in the optical spectra of SNe Ia as, e.g., the optically thin emission features at ~ 4700 Å and ~ 5200 Å of Fe II and Fe III. Several studies of nebular spectra of SNe Ia corroborate this forbidden line interpretation of late-time spectra of SNe Ia (e.g., Meyerott 1978; Axelrod 1980; Meyerott 1980; Ruiz-Lapuente and Lucy 1992; Kuchner et al. 1994;

Ruiz-Lapuente, Kirshner, et al. 1995; Bowers et al. 1997; Mazzali, Maurer, et al. 2011; Mazzali and Hachinger 2012; Silverman et al. 2013).

In principle the same process — collisional excitation followed by radiative de-excitation — could apply to permitted transitions as well, as long as the gas temperature is high enough to excite the atoms to the requisite levels (for Fe II these levels have energies $\gtrsim 4$ eV). Indeed, Fransson (1984) explored spectral line signatures under various conditions of radiative- and collisionally-dominated excitation/de-excitation processes and found that if collisional excitation dominates, the resulting spectral line profiles can be strongly in emission, centered at the rest wavelength of the line, with only weak absorption to the blue of the emission peak (cf. his Figure 5). In SNe Ia, the gas temperatures necessary to populate these higher energy levels are present at early times (near maximum light), but because the mean intensity of the radiation field at most UVOIR wavelengths is so high at this epoch, it is much more likely that an atom will undergo radiative excitation to the upper level of a permitted transition, rather than collisional excitation. The immediately ensuing radiative de-excitation completes this process of line scattering, which in SNe Ia spectra presents as a P Cygni profile, with a strong absorption feature blueward of the line rest wavelength (Branch, Baron, et al. 2005).

There exists an alternative interpretation for at least a few late-time SN Ia spectra, namely that the permitted lines of a few elements – mainly Na I, Ca II, and Fe II – remain optically thick, and that the majority of the optical spectrum, especially blueward of ~ 6000 Å, is formed through line scattering. Good spectral

fits have been obtained with the parameterized spectrum synthesis code SYNOW[2], which treats only line scattering by permitted lines, of the normal SN 1994D at day +115 (Branch, Baron, et al. 2005), the normal SN 2003du at day +84 (Branch, Jeffery, et al. 2008), the subluminous SN 1991bg at day +91 (ibid.), and the peculiar SN 2002cx at day +227 (Jha et al. 2006). While the parameterized approach of SYNOW to solving the radiative transfer equation restricts analysis of those fits to putative line identifications and velocity measurements, they nevertheless demonstrate that either SN Ia spectra exhibit a remarkable degeneracy with respect to forbidden and permitted line formation, or that permitted lines continue to drive emergent spectrum formation at late times, regardless of what physical mechanisms generate the underlying flux (Branch, Jeffery, et al. 2008).

These two competing analyses of late-time SN Ia spectra agree that the majority of the spectrum is formed by Fe lines, but they predict dramatically different velocities of the line-forming regions in the ejecta. For example, Branch, Jeffery, et al. (ibid.) argue that Fe, Ca, and Na are located at 7000 $\mathrm{km\,s^{-1}}$ and higher in the day +84 spectrum of SN 2003du. In contrast, Bowers et al. (1997) argue for velocities from 1000–3000 $\mathrm{km\,s^{-1}}$ in the +95 spectrum of the same object. Identifying the correct velocity of the line-forming region has important consequences for constraining the structure of the inner regions of SN Ia ejecta, which in turn constrain the as-yet unknown explosion mechanism. It is therefore important to discern which of these line forming mechanisms is actually taking

[2] SYNOW's successor SYN++, which contains identical physics, is available for download at https://github.com/rcthomas/es.

place.

4.3 Spectrum synthesis calculations

Using the same numerical methods discussed in Chapter 3, we obtained fits to each of the optical spectra, as well as to the UV spectrum from *HST*. Below we discuss each epoch in detail.

4.3.1 Day +100

The day +100 spectrum of SN 2011fe and the corresponding synthetic spectrum of the DD model from Domínguez et al. (2001) are shown in Figure 4.8. Overall the fit is good, although a few features in our model do not match those in the observed spectrum, namely the emission feature near 5900 Å. In addition, the peak at 4700 Å in the synthetic spectrum is too weak, the blue side of the broad emission at 7200 Å is absent in the model, and the flux in the blue and near-UV is too high. Most other features are well reproduced, both in strength and in shape.

In the context of much of the literature which concerns late-time SN Ia spectra, the fidelity of this fit is peculiar because the calculation used the most current atomic database of Kurucz (1995, 2002), which includes no forbidden line data for any ions. This stands in contrast to the most common interpretations of spectra of "old" SN Ia, which were discussed in Section 4.2. It also conflicts with kinematic analyses such as that of Maeda, Benetti, et al. (2010), which assume that the emission peaks correspond to forbidden lines forming within a few 100 $\mathrm{km\,s^{-1}}$ of $v \simeq 0$ $\mathrm{km\,s^{-1}}$. Rather, the strong emission peaks at 4700 Å and 5200 Å, which

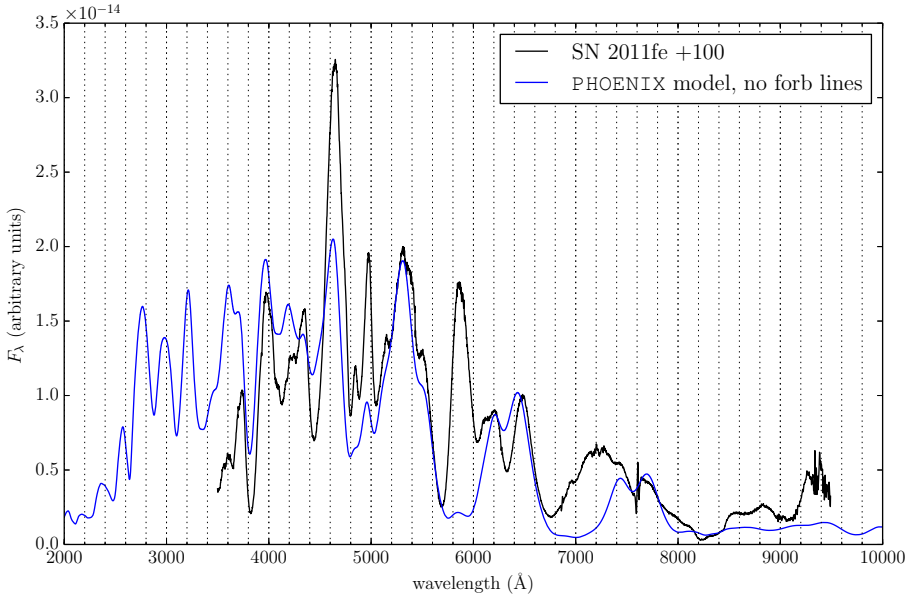

Figure 4.8: Synthetic spectrum of DD model of Domínguez et al. (ibid.) at day 116 vs. SN 2011fe at day +100. No forbidden lines were included in this calculation.

each have previously been identified as a mixture of [Fe II] and [Fe III] lines, may instead be formed by the handful of permitted lines of Fe II whose upper levels are among the crowded $3d^6(^5D)4p$ configuration, with energies between 5 eV and 6 eV, and whose lower levels are, coincidentally, the handful of metastable levels around 3 eV which are purportedly responsible for the aforementioned forbidden emission features. In the line-scattering interpretation of spectrum formation, this would imply that the dips just to the blue of these two strong emission features are the corresponding absorptions, rather than regions lacking in emission. These absorptions would correspond to line velocities of ~ 6000 km s^{-1}, similar to that found in the +115 spectrum of SN 1994D by (Branch, Baron, et al. 2005).

Although below we illustrate some complications with this permitted-line-only

model, it is instructive first to entertain the idea that this is in fact representative of late-time spectrum formation physics in SNe Ia. Given the contrast of this result with those found elsewhere in the literature, it is important to evaluate the late-time line scattering scenario within the context of other analyses of SN 2011fe, in order to determine whether or not it is consistent with what is already known about the spectral evolution of this object. We consider three such pieces of analysis. First, Parrent, Howell, et al. (2012) traced the velocity evolution of Fe II in the early spectra of SN 2011fe using the automated spectrum code `SYNAPPS` (Thomas et al. 2011) and found that at day +15 the minimum velocity of that ion was ~ 9000 km s^{-1} (see their Figure 3). After maximum light, the rate of change of line velocities in SN 2011fe, and in most SNe Ia in general, slows dramatically. Second, in the hydrodynamical model used in our calculation, Fe remains the most abundant species in the ejecta from the center of the ejecta out to $\sim 12\,000$ km s^{-1} (cf. Figure 3.2); our putative line velocity estimate of ~ 6000 km s^{-1} falls well within this range. Finally, Iwamoto et al. (1999) show that the optical depth of Fe II computed in local thermodynamic equilibrium (LTE) peaks between 5000 K and 10 000 K, roughly the same temperature range as that of the ejecta in our models. (One would be remiss to read too much into this corroboration, as the radiation field in the SN Ia ejecta at this epoch is far from LTE.) Although none of these results offer conclusive evidence that the strong features in the +100 spectrum of SN 2011fe are indeed P Cygni profiles, they do show that it is quite reasonable to consider that possibility.

We caution that it is unlikely that the *entire* optical spectrum consists of

overlapping P Cygni line profiles due to resonance-scattering, as is the case at very early (photospheric) epochs in SNe Ia. Branch, Jeffery, et al. (2008) attempted to fit the day +84 spectrum of SN 2003du with the resonance-scattering code `SYNOW`, and found that P Cygni lines fit the blue part of the spectrum (blueward of 6600 Å) quite well, but failed quite severely redward of that. As they discuss, the likely explanation is that resonance-scattering near this epoch is very influential at blue wavelengths, but forbidden emission is prominent in the red. (We find a similar result in our attempts to fit the optical and UV spectra at +349 and +360, respectively, which we discuss below.) In fact, to argue that spectrum formation consists of *either* resonance-scattering by optically thick permitted lines *or* emission from optically thin forbidden lines is somewhat of a false dilemma, as both scenarios assume a degree of locality in the radiative transfer which is probably unphysical. In particular, the former assumes that the source function S depends only on the local mean intensity J, while the latter assumes that emitting lines are well separated in wavelength such that they act independently of each other. Each of these approximations is valid in certain regimes, i.e., resonance-scattering at photospheric epochs and forbidden emission at *very* late times (> 1 yr) and in wavelength regions far from the forest of iron-peak lines, such as the infrared, but there exists a wide range between those extremes, in which all of these effects compete to form the emergent spectrum.

Bongard et al. (2008) addressed this topic in detail by calculating a grid of `PHOENIX` spectra using the hydrodynamical model W7 (Nomoto et al. 1984) at 20 days post-explosion. They found that even at very low velocities and high

optical depth ($\tau > 3$), the "spectrum"[3] at those velocities is already highly distorted from that of a blackbody, due to line and continuum interactions of the radiation field with iron-peak elements deep in the core of the SN. The ions found at higher velocities, near the photosphere, then further distort this underlying spectrum through additional absorption, emission, and line scattering, leading to an emergent spectrum containing a complicated mixture of P Cygni, continuum, and thermal components which are difficult to disentangle.

That our spectral model which explicitly omits forbidden line data fits the day +100 spectrum of SN 2011fe reasonably well, suggests that day +100 is simply too early for collisionally excited forbidden emission to be the primary driver of spectrum formation. It appears that line scattering processes continue to contribute significantly, even this late in the lifetime of this SN. In short, there are many physically-motivated reasons to suspect that permitted lines play an important role in SN Ia spectrum formation at this epoch.

However, since forbidden lines are frequently invoked as comprising spectra of SNe Ia of this age, we tested this hypothesis by expanding our atomic database to include collisional and radiative data of forbidden lines, as described in Chapter 3. We then repeated the radiative transfer calculation with this expanded database, and compare the two results in Figure 4.9. The results are quite similar, except that the model with forbidden lines has a lower UV flux and stronger emission at 7300 Å and 8600 Å.

The most notable shortcoming of both synthetic spectra is the lack of emission

[3]The radiation flux F_λ.

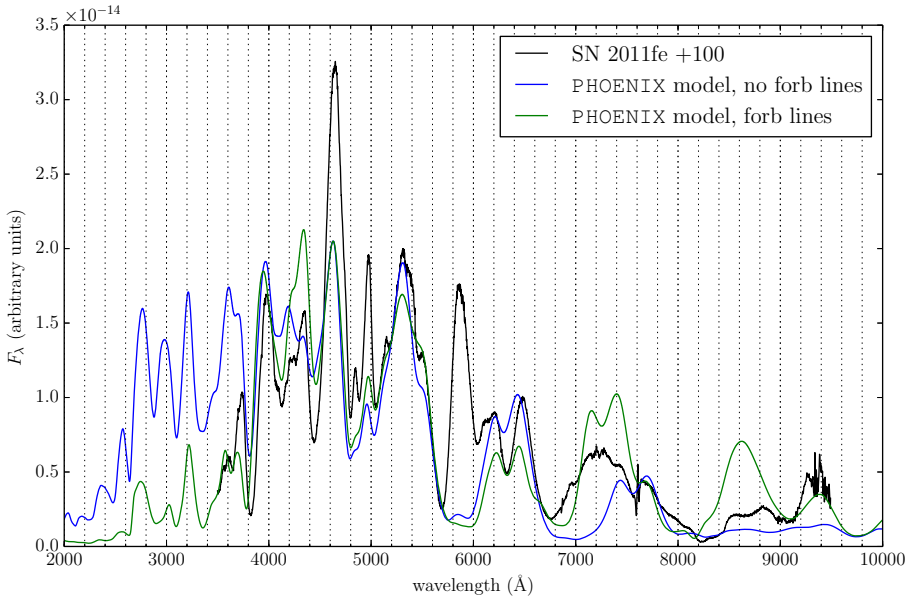

Figure 4.9: Comparison of PHOENIX spectra with and without forbidden lines at day 116.

at 5900 Å. This feature has been identified alternatively as Na I D (Branch, Jeffery, et al. 2008; Mazzali, Sauer, et al. 2008) or [Co III] λ5888 Å (Dessart, Hillier, et al. 2014). The explosion model used in these calculations contains little Na, so it is not surprising that we do not recover a strong Na I D emission feature there. However, at day 116 the model contains several 0.1 $M_\odot$ of ^{56}Co, and yet the forbidden emission at 5900 Å does not appear. This curious discrepancy is one we have not yet been able to resolve, although it may be related to underestimating the gas temperature in the model at this epoch (see Section 4.3.2).

Identifying whether a feature is an "emission" or "absorption" is not a straightforward task in PHOENIX calculations. This is because the algorithm calculates emissivities and opacities of NLTE species by adding up all contributions to each at each wavelength point (e.g., Hauschildt and Baron 2014), with no regard

to the underlying atomic processes which produced them. Such an approach captures naturally the notion that spectrum formation is inherently multi-layered in supernovae: one region deep in the ejecta may be strongly in emission at one wavelength, but a region above it may be optically thick at that wavelength, absorbing much of the underlying emission (Bongard et al. 2008). The emergent spectrum is then a convolution of both processes, and such classifications as "absorption" or "emission," while relevant to single interactions, no longer describe adequately the complete process of spectrum formation.

We are therefore relegated to using more indirect methods for isolating the sources of features in synthetic spectra. The single-ion spectrum method (ibid.) can help one identify the particular ion or ions which influence particular parts of a synthetic spectrum, but it cannot, e.g., isolate the effects of permitted lines from forbidden lines, which is desirable in this context. We found that the only useful way to accomplish this was to remove the forbidden lines from the calculation entirely and re-compute the entire model. This can unfortunately broaden the parameter space of the model, since forbidden lines affect the temperature structure by acting as coolants (Dessart, Hillier, et al. 2014; Friesen, Baron, Wisniewski, et al. 2014). Unfortunately we are aware of no more targeted method of accomplishing this goal.

We computed single-ion spectra for both synthetic spectra (with and without forbidden lines), for the most influential ions. For the spectrum without forbidden lines, these are shown in Figure 4.10. For the spectrum with forbidden lines, these are shown in Figure 4.11.

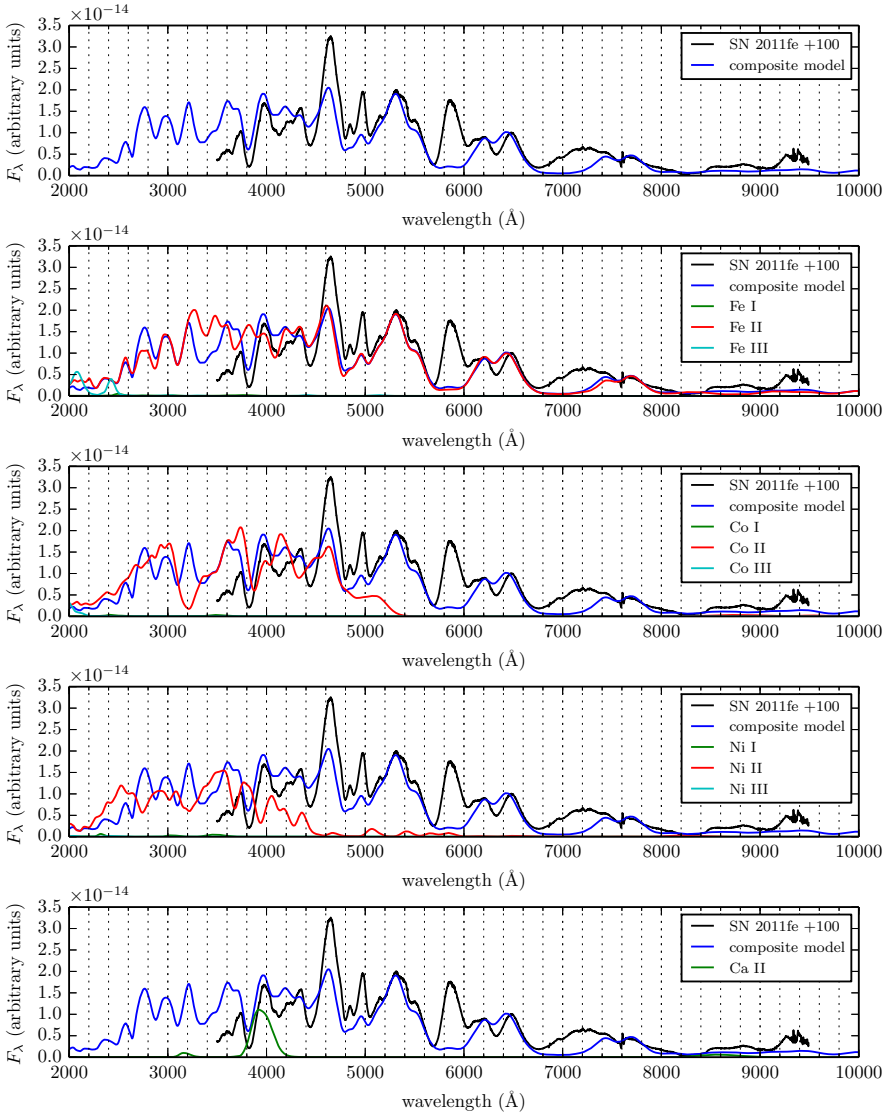

Figure 4.10: Single-ion spectra corresponding to the composite spectrum of the DD model of Domínguez et al. (2001) at day 116, compared to SN 2011fe at day +100. No forbidden lines were included in this calculation.

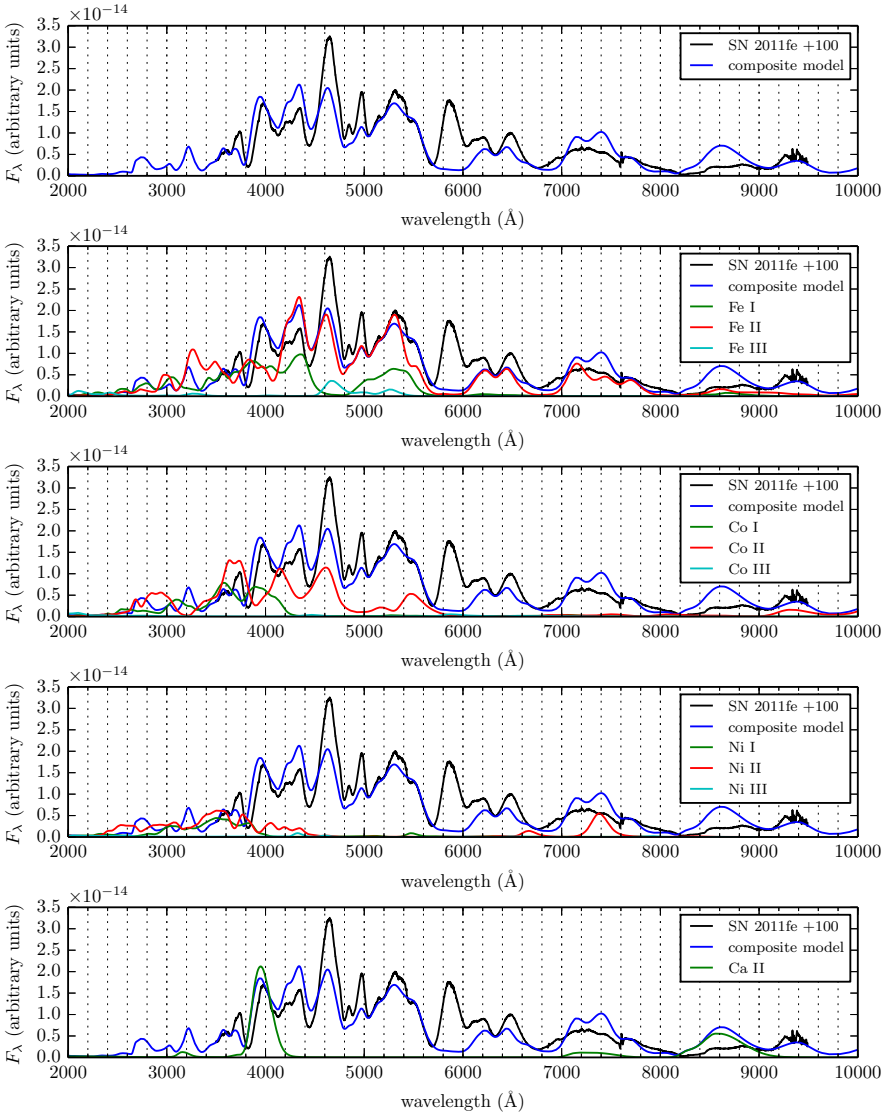

Figure 4.11: Single-ion spectra corresponding to the composite spectrum of the DD model of Domínguez et al. (2001) at day 116, compared to SN 2011fe at day +100.

Both with and without forbidden lines, the synthetic spectra indicate that most of the optical spectrum at day +100 is formed by Fe II. In addition, the Ca II H & K doublet at $\lambda\lambda 3934, 3968$ Å, a pair of strong resonance lines, contributes significantly to the emission at 4000 Å. However, comparison between the two sets of single-ion spectra indicate a fascinating result which Branch, Jeffery, et al. (2008) found highly improbable: it appears that entirely different combinations of atomic lines can conspire to produce similar optical spectra. Furthermore, the synthetic spectra in Figure 4.8 and Figure 4.9 are the *natural endpoints* of calculations subject to otherwise identical parameters. For example, when forbidden lines are included, the emission at 4000 Å is due entirely to the Ca II H & K doublet; when they are absent, it is a combination of that same doublet with contributions also from Fe II and Co II. The double-horned emissions at 7250 Å and 7500 Å in the synthetic spectra lacking forbidden lines are due to emission from Fe II; but the double-horned features at 7150 Å and 7400 Å in the spectra containing forbidden lines are due to Fe II (possibly [Fe II] $\lambda\lambda 7155, 7171$ Å)and [Ni II] $\lambda 7374, 7412$ Å. As discussed in Chapter 3, this is likely stable ^{58}Ni, since the radioactive ^{56}Ni has mostly decayed by this point. The degeneracy among these various features is the likely explanation for the conflicting results of, e.g., Bowers et al. (1997) and Branch, Jeffery, et al. (2008).

One would expect that adding forbidden lines is always favorable over neglecting them: if a calculation captures all relevant atomic processes and if forbidden lines are truly unimportant in some scenario, they will naturally "deactivate". And in fact, adding in the forbidden atomic data did address some problems in

the synthetic spectra which lacked them. The lower UV flux and the 8600 Å emission in the synthetic spectrum with forbidden lines can be explained by their cooling effects: lower temperatures generally lead to lower opacities in the UV, and a lower temperature allows more Ca III to recombine to Ca II. However, the cooling effects also introduced a new problem: the infrared triplet (IR3) of Ca II $\lambda\lambda 8498, 8542, 8662$ Å (a trio of strong permitted lines) is responsible for the emission at 8600 Å, but the model overestimates the strength of the emission at this wavelength. In the observation there is a pair of weaker emission features at the same location, and it is possible that at least one of these two emissions is due to the Ca II IR3, although probably not both, since they are spread too far apart in wavelength. It is therefore not entirely clear which of the two synthetic spectra are "better," and it is possible therefore that both permitted *and* forbidden lines affect the optical spectra of SNe Ia at this epoch.

The synthetic spectra from the two PRD models from Bravo, García-Senz, et al. (2009) are shown in Figure 4.12. Both of these spectra included radiative and collisional effects of forbidden lines. Only minute quantitative differences exist between them, which are as likely due to uncertainties in the radiative transfer calculation itself – particularly the enforcement of radiative equilibrium – as they are to differences in the explosion models themselves. Most of the same features are fit with the same species as in the DD model, including the Ca II H & K doublet at 4000 Å. However, the emission near 4700 Å is too weak, and, as in the DD model, we find no emission from either Na I D or [Co III] λ5888 Å near 5900 Å. In addition, the Ca II IR3 is too strong, indicating that the temperature

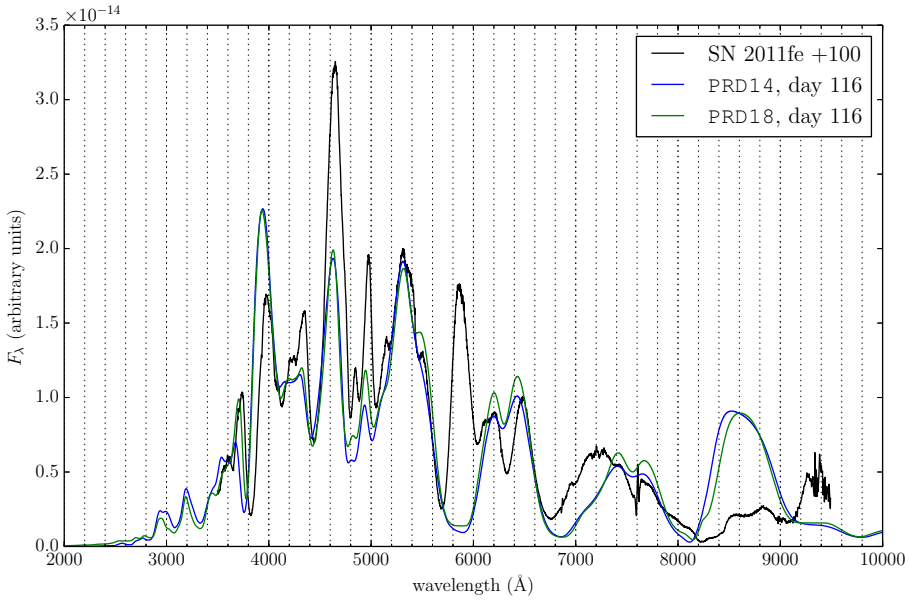

Figure 4.12: Synthetic spectrum of pulsating reverse detonation models PRD14 and PRD18 of Bravo, García-Senz, et al. (ibid.) at day 116 vs. SN 2011fe at day +100.

is too low.

As mentioned above, one important way in which PRDs differ from DDs is the presence of up to 0.1 $M_\odot$ of unburned C/O near the center of the ejecta (Baron, Jeffery, et al. 2008; Bravo, García-Senz, et al. 2009). Kozma, Fransson, et al. (2005) showed that late-time spectrum synthesis provide strong upper limits on the mass of unburned material. Specifically, they found that explosion models with large amounts of unburned material form strong emission features of [O I] $\lambda\lambda 6300, 6364$ Å which are not observed in nature. They studied a pure deflagration model which produced 0.34 $M_\odot$ of C and 0.42 $M_\odot$ of O (Travaglio et al. 2004; Röpke 2005). The corresponding masses in our two PRD models are much lower: 0.061 $M_\odot$ of C and 0.105 $M_\odot$ of O in PRD14, and 0.101 $M_\odot$ of C and

0.149 $M_\odot$ of O in `PRD18`. In our synthetic spectra of these PRD models, neither C nor O contribute significantly to the optical synthetic spectrum at day +100; the contributions from various ions are the same as the DD model.

4.3.2 Day +205

The day +205 spectrum of SN 2011fe and the corresponding synthetic spectrum of the DD model are shown in Figure 4.13. Attempts to calculate a spectrum at this epoch without forbidden lines, as was done in Section 4.3.1, led to unrecoverable numerical instabilities in the code. It seems, then, that by this age forbidden lines play an important role. The single-ion spectra are shown in Figure 4.14. The emission feature at 4700 Å is primarily [Fe III] $\lambda\lambda 4607, 4658$ Å and [Fe II] $\lambda\lambda 4640, 4664$ Å. The weak but clearly separate features around 4300 Å are [Fe II] $\lambda\lambda 4287, 4359$ Å, and the emission at 5300 Å is [Fe II] $\lambda 5300$ Å. The double-horned feature in the synthetic spectrum centered around 7300 Å consists of [Fe II] $\lambda\lambda 7155, 7172$ Å on the left, and [Ni II] $\lambda 7412$ Å on the right; the shape of this pair of features is too exaggerated in the synthetic spectrum compared to the day +100 spectrum of SN 2011fe, but at this and later epochs the shape is a good match to the observations.

At this epoch the ratio of Fe II to Fe III is well reproduced, with the strength of the 4700 Å emission from Fe III improved over that from the day +100 spectrum. However, the 5200 Å emission, also from Fe III, is somewhat weak. The strong Ca II IR3 emission which was overestimated in strength in the day +100 synthetic spectrum is now absent entirely. Coincidentally, the forbidden line [Fe II] $\lambda 8617$ Å,

at nearly the same wavelength as IR3, has grown in strength at day +205, and fits quite well to the observation. The Ca II H & K doublet, which was quite strong at day +100, has diminished in strength and is replaced mostly by [Fe III] λ4008 Å. It seems, then, that the serendipitous degeneracy among permitted and forbidden lines which Branch, Baron, et al. (2005) found unlikely, may actually be realized, at least for some features in the optical spectra of SN 2011fe.

The double-horned pair of emissions centered at 7200 Å is better reproduced at this epoch as well. Curiously, the emission at 5900 Å is now quite well fit with [Co III] λ5888 Å, while at day +100, when most of the ^{56}Ni had decayed to ^{56}Co, the feature was absent entirely. It is possible that the temperature in the day +100 model was too low, which would explain the underabundance of Fe III emitting at 4700 Å and Co III emitting at 5900 Å. A higher temperature would also reduce the abundance of Ca II in favor of Ca III, explaining the reduced strength of both the H & K doublet and the IR3.

The synthetic spectra from the PRD models are shown in Figure 4.15. Many of the features fit by [Fe II] and [Fe III] are well reproduced, just as in the DD model. However, unlike the DD model, in which the relative strength of the emission near 4700 Å grows considerably from day +100 to day +205, the PRD models produce emission at 4700 Å which stays effectively constants during this period, and is too weak compared to SN 2011fe at day +205. In addition, the PRD models produce no corresponding emission near 5900 Å, even though by this epoch the DD model fits the feature well with [Co III] λ5900 Å. The PRD models mix iron-peak elements evenly over a broad range of the ejecta, which

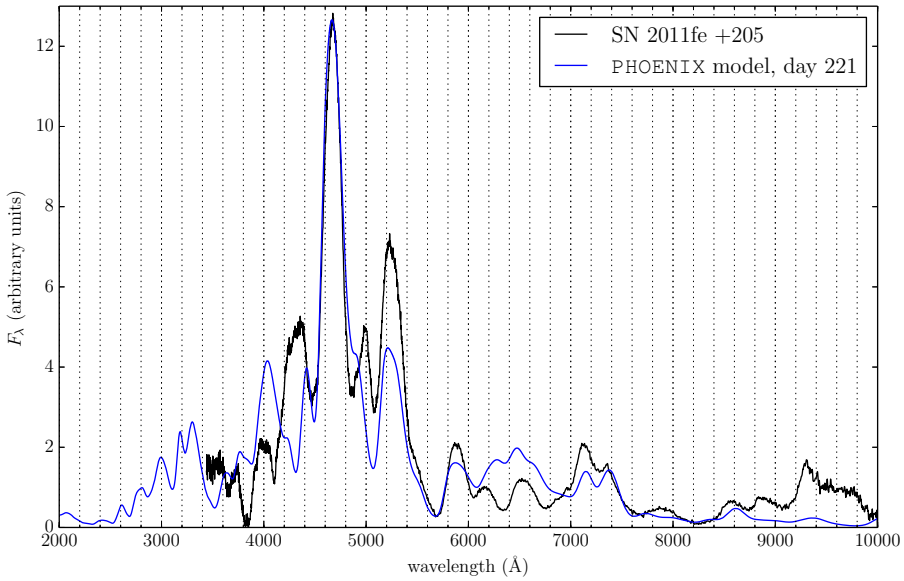

Figure 4.13: Synthetic spectrum of DD model of Domínguez et al. (2001) at day 221 vs. SN 2011fe at day +205.

may be responsible for both of these shortcomings; a more central distribution of Fe (or ^{56}Ni), as is found in the DD models, might be key to producing these two features correctly in synthetic spectra. Finally, the lack of ^{58}Ni in the nuclear reaction network of the PRD models yields no conspicuous emission near 7400 Å. Emission from C and O is even weaker than at day +100, contributing effectively nothing to the synthetic spectrum.

4.3.3 Day +311

The observed spectrum at day +311 and the synthetic spectrum of the DD model are shown in Figure 4.16; the single-ion spectra are shown in Figure 4.17. At this epoch the spectra look similar to those at day +205. The [Fe III] emission at 4700 Å is still strong, although at day +311 the [Fe II] emission at 4400 Å

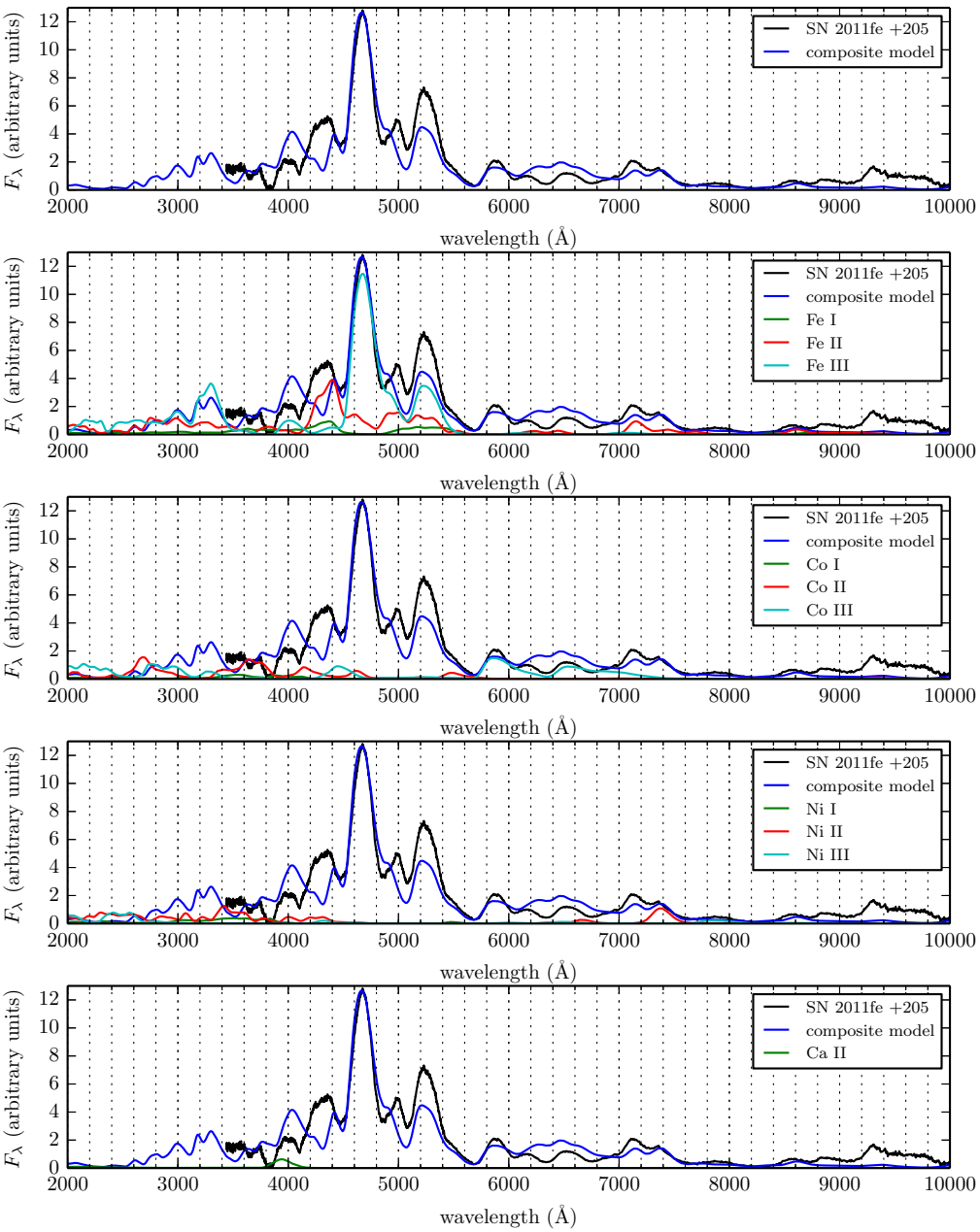

Figure 4.14: Single-ion spectra corresponding to the composite spectrum of the DD model of Domínguez et al. (2001) at day 221, compared to SN 2011fe at day +205.

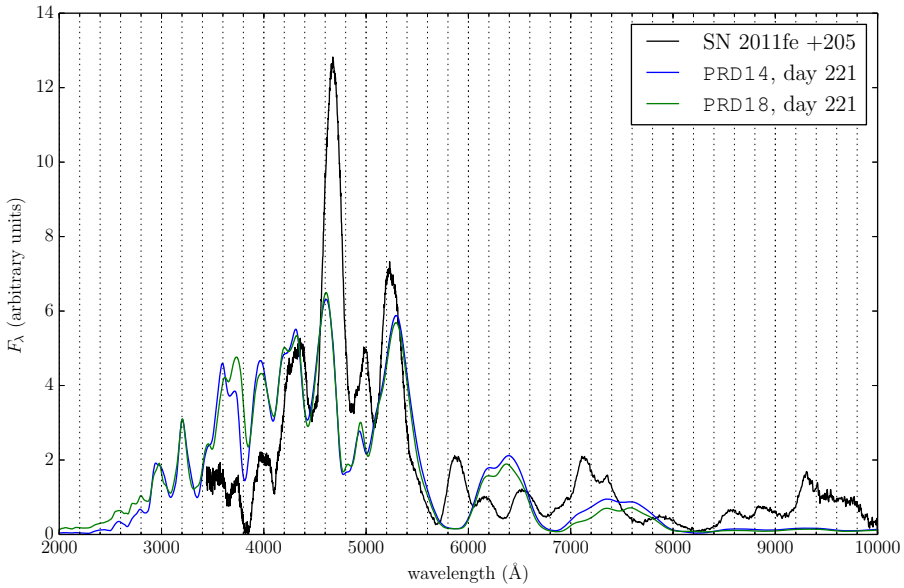

Figure 4.15: Synthetic spectrum of pulsating reverse detonation models PRD14 and PRD18 of Bravo, García-Senz, et al. (2009) at day 221 vs. SN 2011fe at day +205.

has grown in strength, and continues to do so at later epochs. This is likely a reflection of some (but not much) recombination from Fe III to Fe II at this age. The Ca II H & K emission is still present at 4000 Å, but somewhat weak, as at day +205.

The PRD synthetic spectra are shown in Figure 4.18. The fit at this epoch is quite poor, and becomes worse at later times. We therefore stop our analysis of the PRD models at day +311, since there is little information to be harvested from such poorly matching spectra. Much of the emission at bluer wavelengths is due to Fe II; a similar trend occurs in the DD model, although not until later times.

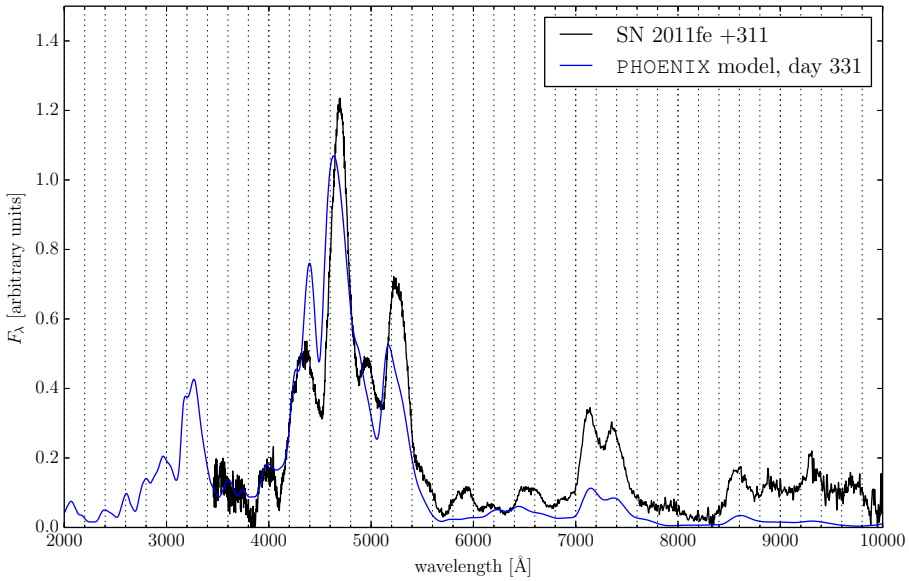

Figure 4.16: Synthetic spectrum of DD model of Domínguez et al. (2001) at day 331 vs. SN 2011fe at day +311.

4.3.4 Day +349

The DD model and observations at day +349 are displayed in Figure 4.19. The corresponding single-ion spectra are shown in Figure 4.20. The Ca II H & K doublet emission at 4000 Å is of similar strength as at day +205, and it may still contribute to that feature in SN 2011fe, although the [Fe III] appears to be stronger at that wavelength.

At this and later epochs the model begins to exhibit some problems. A sharp emission feature forms in the near-UV at 3300 Å in the synthetic spectrum which is not observed in SN 2011fe. In addition, in the synthetic spectrum the emission at 4400 Å (due mostly to Fe II) is nearly as strong as the 4700 Å feature (mostly Fe III), while in the observed spectrum the latter remains considerably stronger.

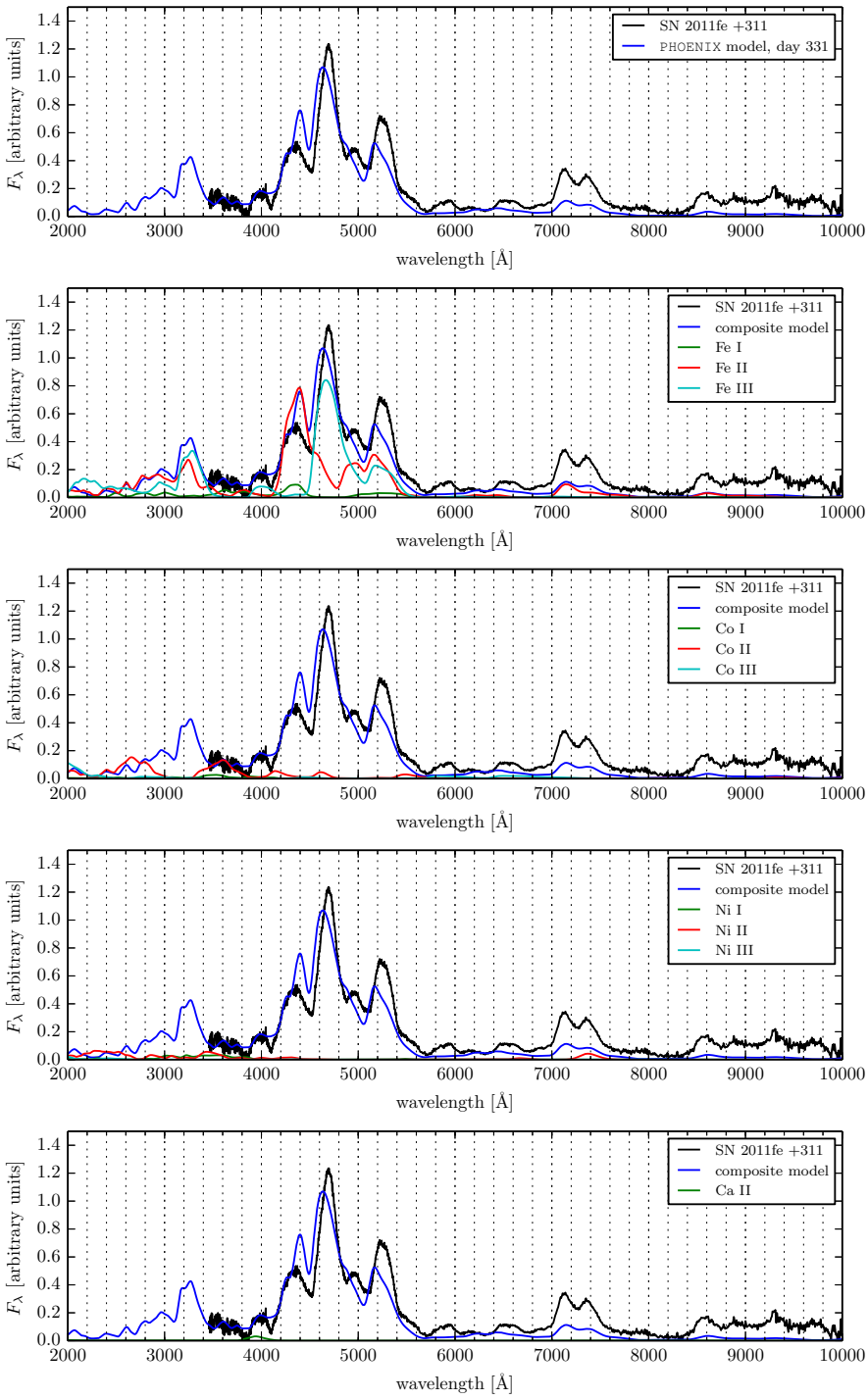

Figure 4.17: Single-ion spectra corresponding to the composite spectrum of the DD model of Domínguez et al. (2001) at day 331, compared to SN 2011fe at day +311.

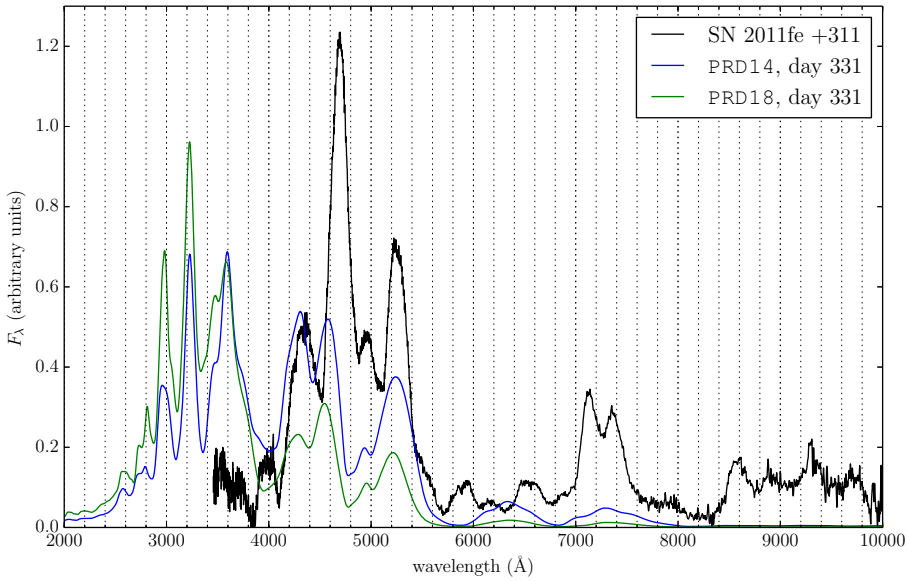

Figure 4.18: Synthetic spectra of models `PRD14` and `PRD18` of Bravo, García-Senz, et al. (2009) at day 331 vs. SN 2011fe at day +311.

This problem is likely not one of radiative transfer effects in the model, but rather one of atomic physics. The recombination rate for ions scales with the free electron density n_e, which dilutes geometrically roughly as t^{-3} (De et al. 2010b). Thus at these very late times the recombination time scale for, e.g., Fe II, can be of the same order as the dynamical time scale, i.e., the age of the SN. In this case, time-dependent effects of ion recombination can become influential on spectrum formation. In the calculations used to generate the above figures, we neglected time-dependence in both the radiation field and the ion populations: both are assumed to be in steady-state. Assuming a steady-state radiation field is a valid approximation at late times – since at most wavelengths the optical depths in the ejecta are low, the radiative transfer time scale is effectively the light-crossing time, which is many orders of magnitude shorter than the dynamical time scale.

Thus the radiation field equilibrates with the ejecta almost instantaneously at any given time t. However, by assuming steady-state in the ion populations, we overestimate the rate of recombination from, e.g., Fe III to Fe II. This manifests in synthetic spectra as Fe II features which are too strong, as in Figure 4.19. Presumably the same pathology affects the day +578 synthetic spectrum more severely (see Section 4.3.6).

Time-dependent effects in the ion populations may not be the only source of the discrepant features in the synthetic spectra at very late times. The density profile of the ejecta in the explosion model also strongly affect n_e. Thus the Fe II-to-Fe III population ratio may provide a constraint on the initial conditions of the explosion model. For example, Figure 4.19 may indicate that the density of the iron-rich core of the model is too high, leading to an n_e which is too high, inducing recombination from Fe III to Fe II too soon.

4.3.5 The UV spectrum at day +360

The UV spectrum from *HST* at day +360, as well as the best fitting spectrum from the DD model, are shown in Figure 4.21. The single-ion spectra are shown in Figure 4.22. From these one finds that Fe II is responsible for most of the spectral features in the UV at day +360, just as it was at day +100. However, Fe III, Co III, and Ni III all contribute significantly to the bluest portion of the spectrum as well. The most interesting result, however, is that the Ca II H&K doublet continues to contribute significantly to the emission around 4000 Å, despite being over 1 yr since explosion. It seems, then, that the extreme opacity of

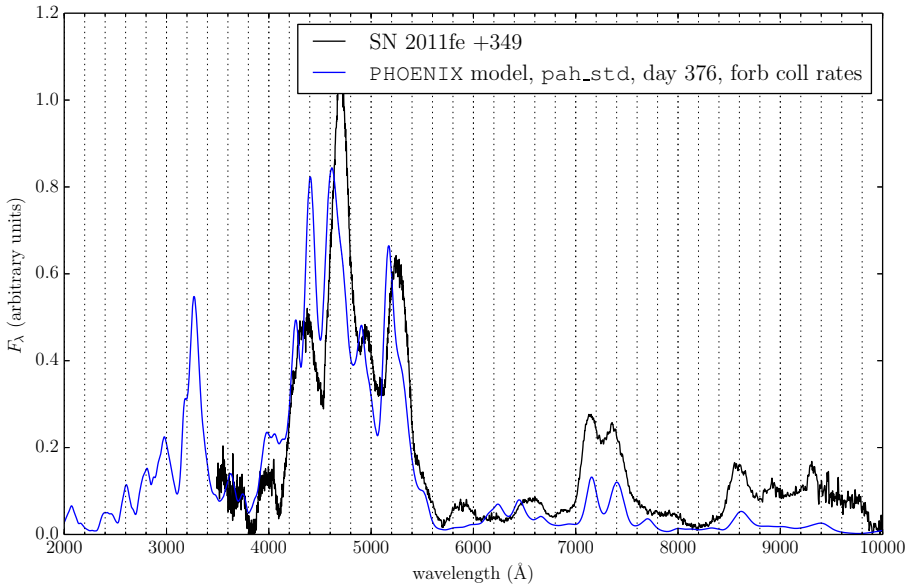

Figure 4.19: Synthetic spectrum of DD model of Domínguez et al. (2001) at day 376 vs. SN 2011fe at day +349.

this line overcomes both the small total abundance of Ca II in the ejecta, as well as the large amount of geometric dilution which accompanies a year of expansion.

A second notable feature of this result is that that nearly all of the Fe II features are permitted lines, not forbidden; the bluest forbidden lines for any ion in this version of the PHOENIX atomic database is about 3200 Å. Identifying these features is no simple feat, however, because Fe II has several thousands of lines between $\sim 1600 - 4000$ Å. Furthermore, the contributions from several other ions in the UV at late times, each with several thousands of lines themselves, are at some wavelengths of similar strength as Fe II. The convolution of all of these lines from different species renders the identification of individual features in the UV a difficult task. However, even without identifying particular lines, we can nevertheless learn a great deal about the UV line forming region using other

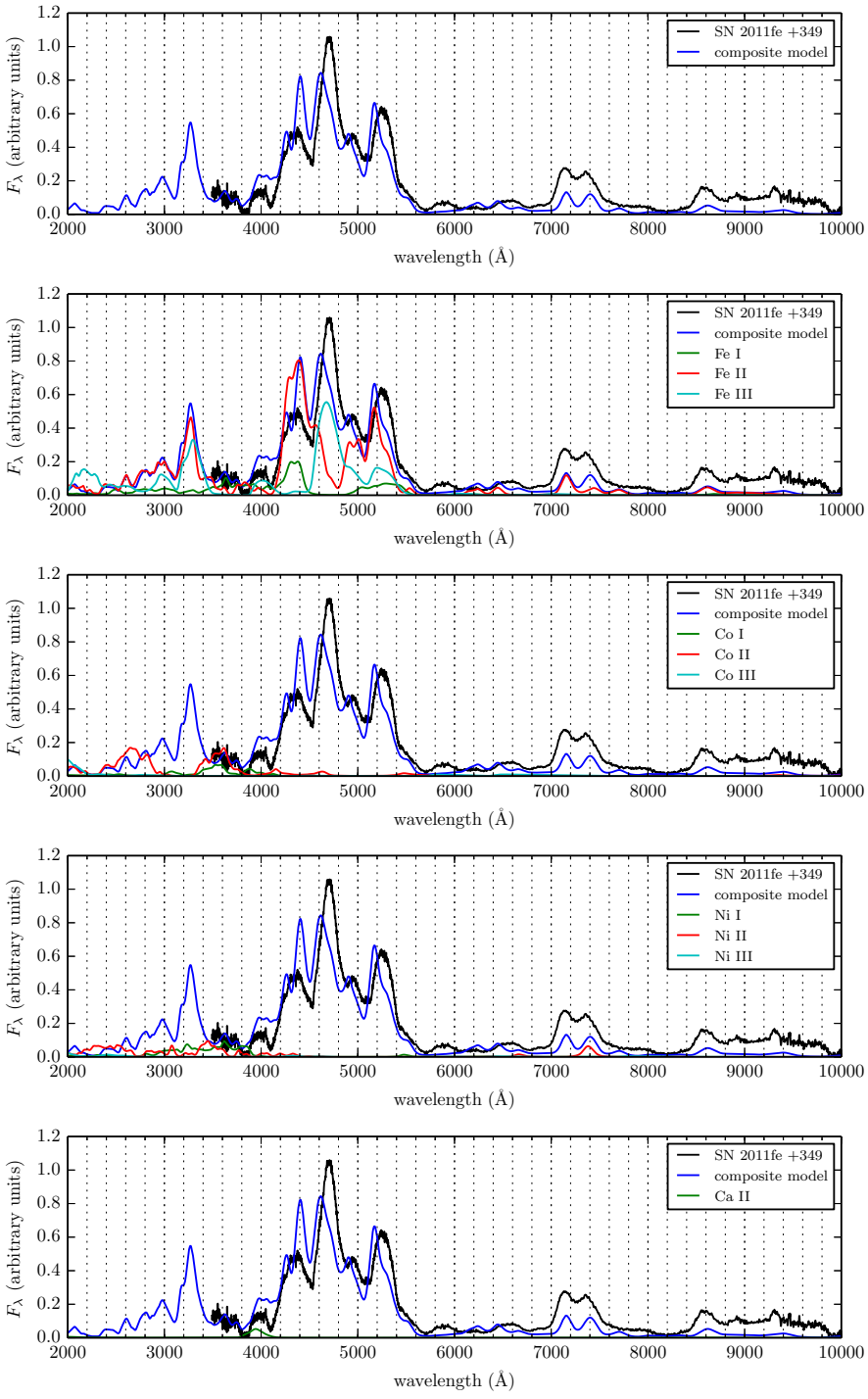

Figure 4.20: Single-ion spectra corresponding to the composite spectrum of the DD model of Domínguez et al. (2001) at day 376, compared to SN 2011fe at day +349.

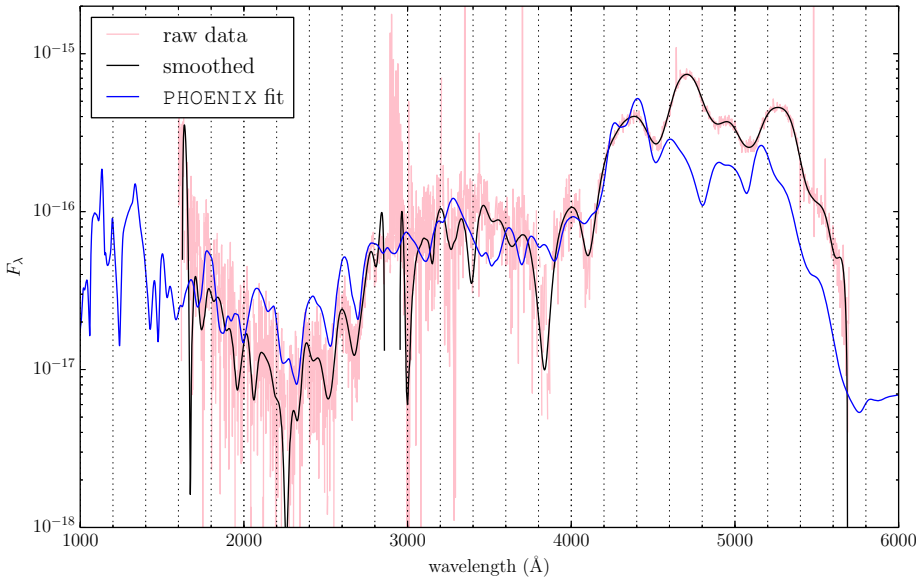

Figure 4.21: Synthetic spectrum of DD model of Domínguez et al. (2001) at day 376, compared to SN 2011fe at day +349.

methods (see Section 4.4).

4.3.6 Day +578

Figure 4.23 shows the observed spectrum of SN 2011fe at day +578, as well as the synthetic spectrum from the DD model. The single-ion spectra are shown in Figure 4.24. The fit of the PHOENIX synthetic spectrum to the observation is poor, and has resisted improvement even experimenting with a variety of different temperature-correction algorithms. Possible culprits for this include time-dependent effects as discussed in Section 4.3.4, as well as other physical processes which PHOENIX currently does not treat, including dielectric recombination and charge-exchange reactions. However, analysis of this result nevertheless reveals some useful information. For example, the unphysical spike in flux around 3250 Å

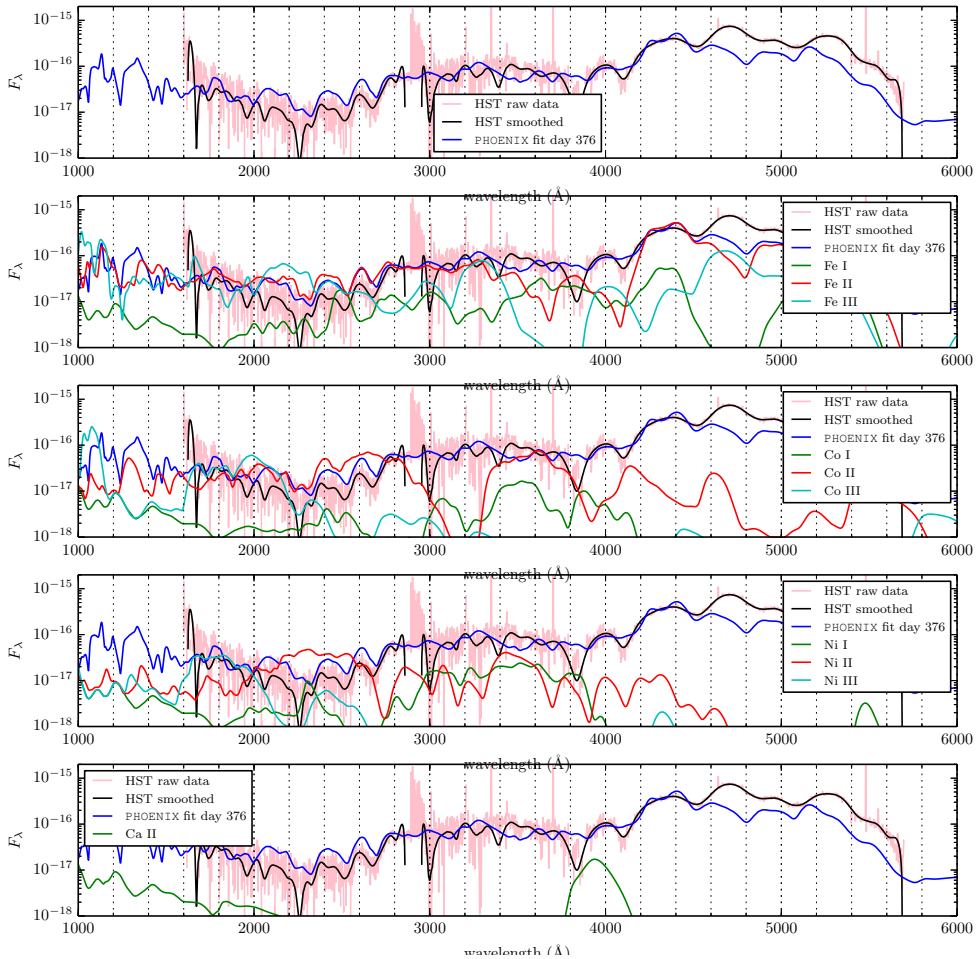

Figure 4.22: Single-ion spectra corresponding to the composite spectrum of the DD model of Domínguez et al. (2001) at day 376, compared to SN 2011fe at day +360.

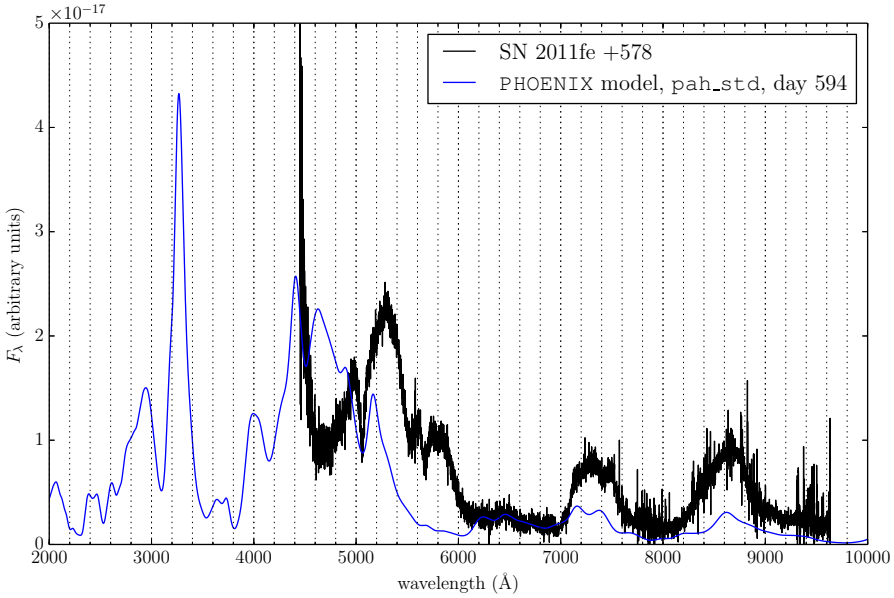

Figure 4.23: Synthetic spectrum of DD model of Domínguez et al. (2001) at day 594 vs. SN 2011fe at day +578.

is due entirely to Fe II, although to which line in particular is not clear. In addition, the emission at 8600 Å formerly produced by Ca II IR3, has been replaced by [Fe II] λ8617 Å. This is yet another example of a truly remarkable degeneracy among permitted lines and forbidden lines at similar wavelength, but which become active at very different times.

Although our model spectra predict the recombination to Fe II too early, the event eventually does happen in SN 2011fe. In particular, in the day +594 spectrum, the strong Fe III emission peak at 4700 Å has disappeared entirely, with only a handful of Fe II features remaining. Indeed, Taubenberger et al. (2015) and Graham et al. (2015) have tentatively identified features of Fe I in $\sim$ 1000 d spectrum of SN 2011fe, perhaps heralding a concurrent recombination transition from Fe II to Fe I.

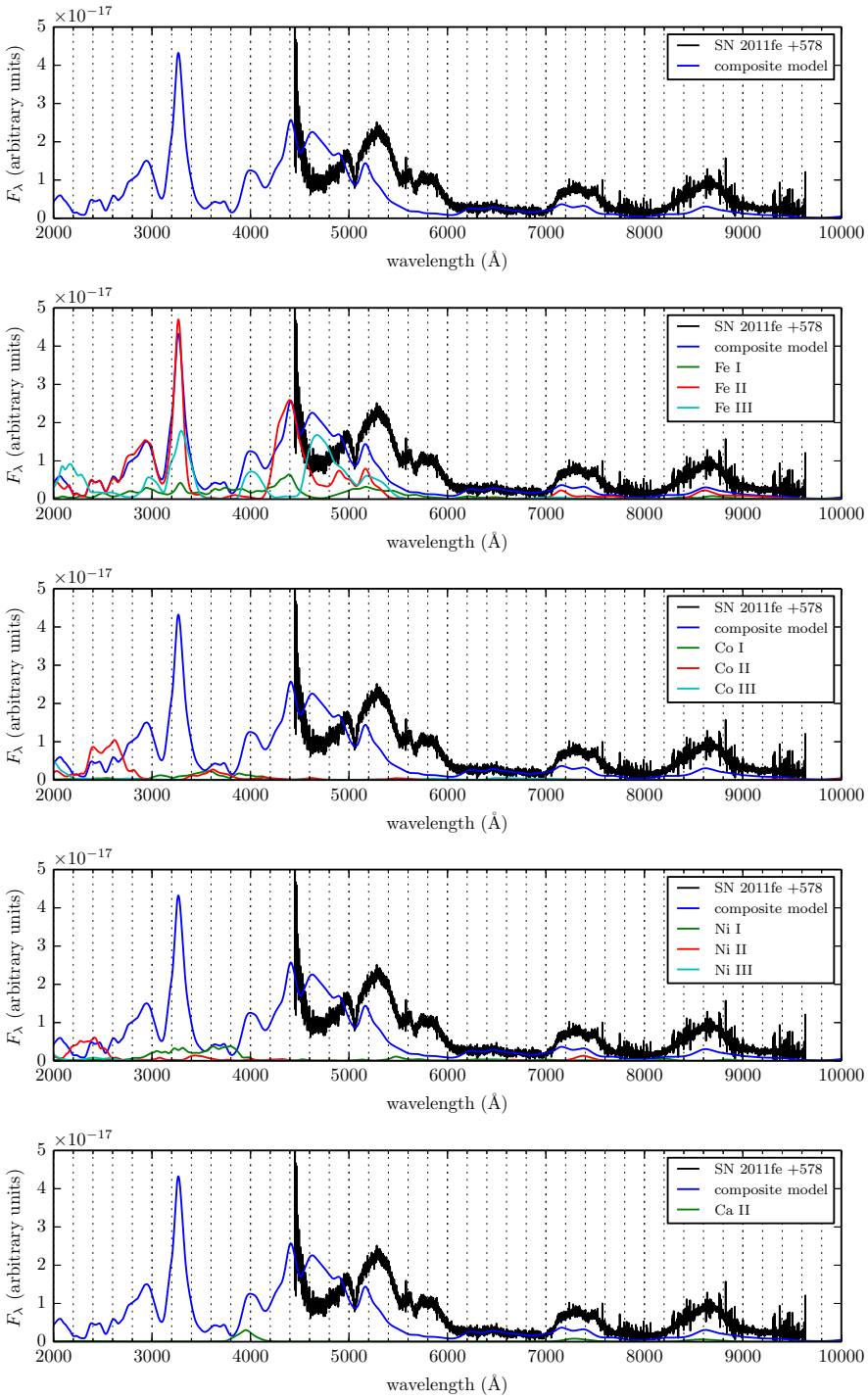

Figure 4.24: Single-ion spectra corresponding to the composite spectrum of the DD model of Domínguez et al. (2001) at day 594, compared to SN 2011fe at day +578.

4.4 Opacity at late times

Our PHOENIX calculations have been fairly successful at reproducing the late-time optical and UV spectra of the normal SN 2011fe. In addition, one of the great advantages of using first-principles codes such as PHOENIX is that one may glean a great deal of information about the underlying physics which drives the formation of the synthetic spectra. For example, in Figure 4.25 we show the optical depths along the $\mu = -1$ (radially inward) ray in the day +349 DD model whose spectrum was shown in Figure 4.19. For reference, the black dashed line shows $\tau = 1$, the division between optically thick and optically thin. The dashed red line shows the optical depth due only to Thomson scattering; at early times this is the dominant opacity source and gives rise to the photosphere in SNe (Section 1.1.2). At late times, however, the geometric dilution of the free electron density n_e leads to a very low Thomson scattering opacity, falling well below $\tau = 1$ even all the way to the center of the ejecta. From this alone we may infer that there is likely very little continuum radiation present this late in a SN Ia's lifetime, as reflected in the spectra. Furthermore, at only a select few wavelengths – mostly on the blue edge of the optical band – does the optical depth reach $\tau = 1$ at all; at most wavelengths $\lambda \gtrsim 4500$ Å, the ejecta are quite optically thin, in agreement with previous studies. Our calculations therefore indicate that most of the optical spectrum at day +349 in SN 2011fe consists of blended emission features from collisionally excited, optically thin forbidden lines.

The UV portion of the spectrum of SN 2011fe behaves entirely differently than

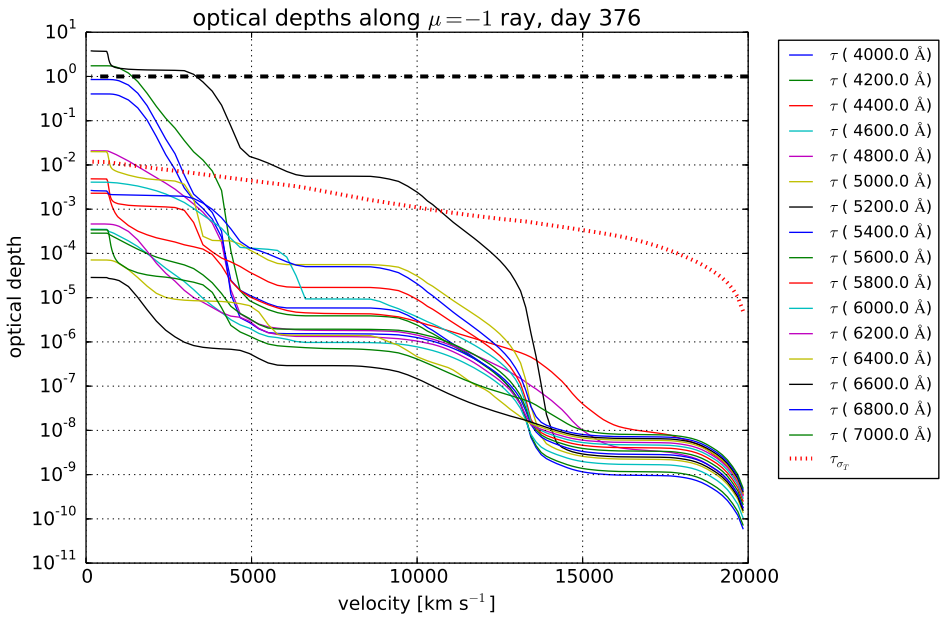

Figure 4.25: Optical depths at a collection of optical wavelengths in the day +349 DD model (cf. Figure 4.19).

the optical, however. One may suspect as much simply by noticing the significant degree of structure and complexity in the observed UV spectrum (Figure 4.2). These suspicions are confirmed by analogous calculations of optical depths at various UV wavelengths, shown in Figure 4.26. The black and red dashed lines are the same as in Figure 4.25. Unlike the optical band, however, most UV wavelengths are *extremely* optically thick, with many reaching $\tau \sim 1 \times 10^5$ at the center of the ejecta. Another surprising result is that many UV wavelengths become optically thick at quite high velocity, crossing the $\tau = 1$ threshold at $v \sim 10\,000 - 15\,000$ km s^{-1}. This result is corroborated by the presence of the emission component of the Ca II H & K doublet near 4000 Å in Figure 4.22.

If the UV remains as optically thick as Figure 4.25 and Figure 4.26 suggest, then it appears that the transition from the "photospheric" to the "nebular" phase

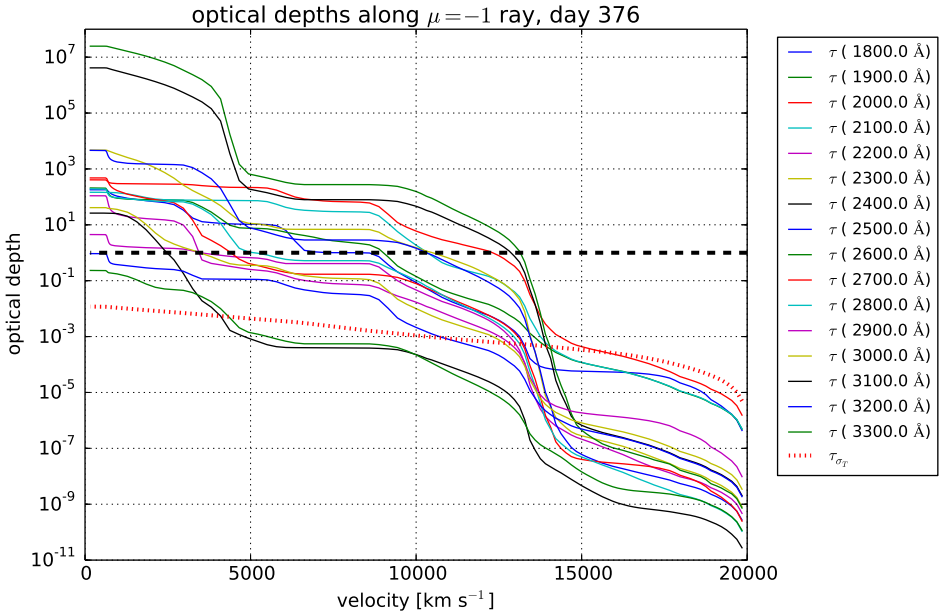

Figure 4.26: Optical depths at a collection of UV wavelengths in the day +349 DD model (cf. Figure 4.19).

in SNe Ia is far more complex than expected. Specifically, there are likely few or no forbidden emission lines which are active in the UV; this precludes the possibility of measuring asymmetric bulk motion of the inner regions of the SN ejecta, since the assumption behind such measurements is that the emission lines are optically thin and centered at the line rest wavelengths (Maeda, Benetti, et al. 2010). On the other hand, since the UV is optically thick, the spectrum may consist of the same overlapping P Cygni line scattering profiles which characterize maximum-light spectra of SNe; if this is the case we may be able to infer ejecta velocities of the iron-rich core of SN 2011fe by measuring the location of the absorption minima of the features in Figure 4.6. However, as discussed in Section 4.3.5, the multitude of UV lines, as well as likely blending among several atomic species, make this challenging. If we entertain the possibility that some of the UV spectrum is

forming at the UV photosphere at velocities of order 10 000 $\mathrm{km\,s^{-1}}$, the rest wavelengths of such lines would still lie within a crowded space of UV and optical transitions of iron-peak elements.

4.5 Conclusions

We extended `PHOENIX` to calculate radiative transfer models well into the late-time epochs of SNe Ia, with an eye toward obtaining good fits to the high-quality optical and UV spectra of SN 2011fe. Doing so required similar methods to those discussed in Chapter 3, in particular using an alternative method to that of Unsöld-Lucy for calculating the temperature structure of the gas, as well as accounting for the collisional and radiative rate data for forbidden lines, which behave quite differently than permitted lines. The resulting synthetic spectra, ranging from +100 to +578 days post-maximum light for delayed-detonation and two pulsing reverse detonation models, vary in degrees of fidelity to corresponding observed spectra of SN 2011fe, with the earlier epochs fitting quite well and the later epochs less so. At day +100 we found that radiative transfer calculations which neglect forbidden lines and those which include them can produce remarkably similar optical spectra, but with quite different atomic species and combinations of lines forming the various features. We found that, at least as late as day +360, permitted lines such as Ca II H & K and IR3 continue to influence spectrum formation in the optical, and permitted lines of Fe II form much of the spectrum in the UV. In addition, these models indicate that some emission features from permitted lines are replaced by other emission features of forbidden lines at nearly

the same wavelength as the SN evolves. For example, the emission from Ca II H & K at 4000 Å is replaced around day +205 by [Fe III] λ4008 Å, and the emission from Ca II IR3 at around 8600 Å is replaced by [Fe II] λ8617 Å. Furthermore, we find that the emission near 7400 Å is well fit by [Ni II] 7374 Å, providing evidence that some ^{58}Ni should be present in explosion models, which occurs during nuclear burning at high density.

The differences is abundance distribution between the DD and PRD models yields significant differences in their synthetic spectra. In particular, emission features from iron-peak species in the PRD models are consistently weak compared to observations. This suggests that a more central distribution of Fe or ^{56}Ni near the center of the ejecta, as found in the DD model, may alleviate some of these problems. In addition, even the considerable amount of unburned C/O in the PRD models plays little role in the synthetic spectra, indicating that it is possible to "hide" even up to $\sim 0.2\ M_{\odot}$ of C/O in late-time spectra.

The problem with the later fits may be related to time-dependent effects in the ionization of the gas, as the recombination time scale at late times is likely of order of the age of the SN. By assuming steady-state in our calculations, we likely overestimated the recombination rate, leading to an overabundance of Fe II with respect to Fe III. Re-computing these models with time-dependence in the NLTE rate equations is possible in principle, but the inherent "noisiness" of the root-finding algorithm we used to calculate the temperatures becomes amplified with each time step, resulting in a large amount of spurious temperature oscillations in the model at very late times, and a poorly fitting spectrum.

Several other uncertainties in our calculations likely also contribute to the shortcomings of the synthetic spectra presented here. For example, uncertainties in both radiative and collisional processes, which can be $> 20\%$ for forbidden transitions, can have significant effects on synthetic spectrum formation (Bautista et al. 2013; Kramida et al. 2013). In addition, there are a few atomic processes which `PHOENIX` currently does not treat. One such process is dielectronic recombination, in which an ion captures a free electron to a bound excited state, and simultaneously promotes a second (bound) electron to an excited state, before emitting a photon during de-excitation. A second process is charge-exchange reactions, in which an ion captures an electron from a donor atom (Jerkstrand et al. 2011). Finally, `PHOENIX` assumes positrons deposit their energy immediately after formation, which is the likely outcome if the magnetic field lines are "tangled" in the SN ejecta (Axelrod 1980). However, if the field lines are instead combed, then the positron mean free path may be a significant fraction of the ejecta radius. This may lead to, e.g., enhanced heating of the non-radioactive Ni "hole" in the inner regions of DD models, where the high degree of neutronization during the deflagration phase has produced significant amounts of stable ^{58}Ni.

Chapter 5

Summary

We have presented in this work a variety of applications of the theory of radiative transfer to SNe Ia, with a particular focus on post-maximum light epochs, where comparatively little spectral analysis has been performed to date. In Chapter 1, we outlined the array of physical processes which contribute in complicated ways to spectrum formation in SNe at all epochs, as well as an overview of the numerical methods used in the `PHOENIX` code to simulate each of these processes. The "dynamic range" of these different processes contribute in large part to conflicting interpretations of SNe Ia at late times, since it is rarely obvious which should be the most influential at any given time, e.g., geometric dilution due to ejecta expansion vs. line strength.

In Chapter 2, we presented semi-analytic calculations inspired by the "Elementary Supernova" model described in Branch, Baron, et al. (2005), which we used to explore spectrum formation in the case of optically thick scattering lines embedded in an optically thin, "glowing" core. The motivation for such a model was the interpretation made in some works (e.g., Branch, Jeffery, et al. 2008) that many spectral features in SNe Ia, even several months post-explosion are due to permitted lines of iron-peak elements, just as they are much earlier in the SN's life. The optically thin, "glowing" continuum was a simple way to mimic the forest

of weak and/or forbidden lines from Ni, Co, and Fe. The parameterized, strong, permitted lines then scatter this continuum, forming spectral profiles similar to the P Cygni profiles which characterize maximum-light spectra in SNe. From this model we found that the emission peak of the spectral profile shifts redward of the rest wavelength, rather than being centered on it. Similarly, increasing the optical depth of the line, shifts the absorption blueward, even while the velocity of the line-forming region remains fixed. If optically thick scattering lines are present at late times in SNe Ia, but are being interpreted as optically thin, forbidden emission, the inferred results for line velocities and other ejecta characteristics will be quite incorrect.

Next, in Chapter 3, we performed the first `PHOENIX` calculations of SNe Ia which focus on NIR spectroscopy, as well as the first to go as late as ~ 3 months post-maximum light. Along with four NIR spectra from three different SNe Ia obtained from the literature, we also obtained two NIR spectra at days +67 and +70 of the nearby SN 2014J. We performed radiative transfer calculations on a spherically symmetric, delayed-detonation explosion model which reproduces the spectroscopic and photometric properties of core-normal SNe Ia near maximum light, and found that with little tuning the NIR spectra match the observations at these epochs quite well. Most of the features from $1.0-1.5$ µm are fluorescence lines of Fe II driven by recombination from Fe III; similarly, most of the features from $1.5-2.5$ µm are fluorescence lines of Co II driven by recombination from Co III. We tentatively identified the emission feature near 1.98 µm as [Ni II] λ1.939 µm, implying that a significant amount of stable ^{58}Ni is present in normal SNe Ia.

However, in our models this forbidden emission feature was consistently redward of the corresponding emission in the observations. It is possible that the line identification is correct and the redshift is due to asymmetry in the ^{58}Ni distribution in the ejecta (being optically thin, Doppler shifts due to asymmetry would be quite visible). If it were a viewing angle effect such as this one would expect to see a random distribution of Doppler shifts of this line; that we see it consistently to the red in the observations does render this interpretation suspect, but with such a small sample (only six spectra from four objects) there is not enough data to make a conclusive statement about this.

Finally, Chapter 4 contains an even later-time analysis of the nearby SN 2011fe, containing observations and models in the optical as late as day +578, as well as in the UV at day +360. To do the radiative transfer calculations we mostly used the same methods as in Chapter 3, and with the same explosion model obtained good fits to the optical spectra of SN 2011fe from day +100 until day +349. We also performed similar calculations on a pair of pulsing reverse detonation models, and found that before day +311 the synthetic spectra fit the observations fairly well, but at later epochs they fit poorly, showing a large UV excess and optical features which are too weak. We found that, at day +100, much of the optical is formed by line scattering from permitted Fe II, with contributions from the Ca II H & K doublet at 4000 Å and possibly the Ca II infrared triplet at 8600 Å. However, repeating the same calculation with forbidden lines yielded similar spectra, but with different combinations of atomic lines forming the various features. Neither set of synthetic spectra is obviously better than the other, in which case it is not

obvious which interpretation is correct for observed spectra of SNe Ia near this age. At all later epochs the permitted Fe II spectral features are replaced by forbidden emission lines of Fe II and Fe III. At days +205 and +311 the H & K emission is much weaker and replaced at least in part by forbidden emission from Fe III. Similarly, the emission at 8600 Å is replaced mostly by forbidden emission from Fe II. At day +349 the PRD models yield poor fits to the observations, although the DD model is still reasonably good. At +578 all of our models produce poor fits to the observations and so it is difficult to glean useful information about that epoch. The DD model also produces a good fit to the UV spectrum at day +360, and indicates that almost all of the UV is formed by permitted lines from a few iron-peak elements, but mostly Fe II. Calculations of optical depth profiles at various optical and UV wavelengths in the DD model indicate that not only is the UV extremely optically thick, but also that the UV "photosphere" may form as far out as 10 000 $\mathrm{km\,s^{-1}}$.

Finally, during our work on this thesis we have come across a variety of other applications of radiative transfer which may be useful for future studies. These are discussed in Chapter D. Specifically, we discuss a modification of the temperature correction scheme originally developed by Hauschildt (1992b) which may produce less "noisy" temperature profiles at late times in SNe Ia than the method we used for most of the calculations presented here. This may also improve the results using time-dependent NLTE rate calculations, since each restart tends to amplify the noise of the previous temperature profile. We also speculate about combining the power of the accelerated Λ-iteration technique for solving the transfer equation

with the flexibility of the 3+1 numerical relativity framework in order to do radiative transfer in arbitrarily relativistic, multi-dimensional simulations.

Bibliography

Alexander, D. R. et al. (July 1997). "Grain Formation in Atmospheres of Cool Dwarfs". In: Ap&SS 251, pp. 171–175.

Allard, F. and P. H. Hauschildt (May 1995). "Model atmospheres for M (sub)dwarf stars. 1: The base model grid". In: ApJ 445, pp. 433–450.

Allard, F., P. H. Hauschildt, D. R. Alexander, et al. (1997). "Model Atmospheres of Very Low Mass Stars and Brown Dwarfs". In: ARA&A 35, pp. 137–177.

Allard, F., P. H. Hauschildt, I. Baraffe, et al. (July 1996). "Synthetic Spectra and Mass Determination of the Brown Dwarf GI 229B". In: ApJ 465, p. L123.

Allard, F., P. H. Hauschildt, S. Miller, et al. (May 1994). "The influence of H2O line blanketing on the spectra of cool dwarf stars". In: ApJ 426, pp. L39–L41.

Ambwani, K. and P. G. Sutherland (Feb. 1988). "Gamma-ray spectra and energy deposition for type IA supernovae". In: ApJ 325, pp. 820–827.

Anupama, G. C., D. K. Sahu, and J. Jose (Jan. 2005). "Type Ia supernova SN 2003du: Optical observations". In: A&A 429, pp. 667–676.

Arnett, W. D. (Feb. 1982). "Type I supernovae. I - Analytic solutions for the early part of the light curve". In: ApJ 253, pp. 785–797.

Arnowitt, R., S. Deser, and C. W. Misner (Sept. 2008). "Republication of: The dynamics of general relativity". In: *General Relativity and Gravitation* 40, pp. 1997–2027.

Auer, L. H. (1971). "The stellar atmospheres problem." In: J. Quant. Spec. Radiat. Transf. 11, pp. 573–587.

— (Mar. 1973). "Application of the Complete-Linearization Method to the Problem of Non-LTE Line Formation". In: ApJ 180, pp. 469–472.

Auer, L. H. and D. Mihalas (Jan. 1968). "Solution of Transfer Equations Subject to the Constraint of Radiative Equilibrium". In: ApJ 151, p. 311.

— (Nov. 1969). "Non-LTE Model Atmospheres. III. a Complete-Linearization Method". In: ApJ 158, p. 641.

Axelrod, T. S. (1980). "Late time optical spectra from the Ni-56 model for Type 1 supernovae". PhD thesis. University of California, Santa Cruz.

Baraffe, I., G. Chabrier, F. Allard, et al. (Nov. 1997). "Evolutionary models for metal-poor low-mass stars. Lower main sequence of globular clusters and halo field stars". In: A&A 327, pp. 1054–1069.

Baraffe, I., G. Chabrier, T. S. Barman, et al. (May 2003). "Evolutionary models for cool brown dwarfs and extrasolar giant planets. The case of HD 209458". In: A&A 402, pp. 701–712.

Baron, E., S. Bongard, et al. (July 2006). "Spectral Modeling of SNe Ia Near Maximum Light: Probing the Characteristics of Hydrodynamical Models". In: ApJ 645, pp. 480–487.

Baron, E., P. H. Hauschildt, and D. Branch (May 1994). "Modeling and interpretation of the optical and HST UV spectrum of SN 1993J". In: ApJ 426, pp. 334–339.

Baron, E., P. H. Hauschildt, D. Branch, S. Austin, et al. (Mar. 1995). "Non-LTE spectral analysis and model constraints on SN 1993J". In: ApJ 441, pp. 170–181.

Baron, E., P. H. Hauschildt, D. Branch, R. P. Kirshner, et al. (Apr. 1996). "Preliminary spectral analysis of SN 1994I". In: MNRAS 279, pp. 799–803.

Baron, E., P. H. Hauschildt, D. Branch, R. M. Wagner, et al. (Oct. 1993). "Interpretation of the Early Spectra of SN 1993J in M81". In: ApJ 416, p. L21.

Baron, E., P. H. Hauschildt, and B. Chen (May 2009). "A 3D radiative transfer framework. V. Homologous flows". In: A&A 498, pp. 987–992.

Baron, E., P. H. Hauschildt, B. Chen, and S. Knop (Dec. 2012). "A 3D radiative transfer framework. X. Arbitrary velocity fields in the comoving frame". In: A&A 548, A67, A67.

Baron, E., P. H. Hauschildt, P. E. Nugent, et al. (Nov. 1996). "Non-local thermodynamic equilibrium effects in modelling of supernovae near maximum light." In: MNRAS 283, pp. 297–315.

Baron, E., D. J. Jeffery, et al. (Jan. 2008). "Detailed Spectral Modeling of a Three-dimensional Pulsating Reverse Detonation Model: Too Much Nickel". In: ApJ 672, pp. 1038–1042.

Baumgarte, T. W. and S. L. Shapiro (June 2010). *Numerical Relativity: Solving Einstein's Equations on the Computer*. Cambridge, UK: Cambridge University Press.

Bautista, M. A. et al. (June 2013). "Uncertainties in Atomic Data and their Propagation through Spectral Models. I." In: ApJ 770, 15, p. 15.

Beck, H. K. B. et al. (Feb. 1995). "Ionization and temperature of nova shells. II. The influence of realistic photospheric radiation fields." In: A&A 294, pp. 195–205.

Benetti, S. et al. (Feb. 2004). "Supernova 2002bo: inadequacy of the single parameter description". In: MNRAS 348, pp. 261–278.

Bessell, M. S. (Oct. 1990). "UBVRI passbands". In: PASP 102, pp. 1181–1199.

Bloom, J. S. et al. (Jan. 2012). "A Compact Degenerate Primary-star Progenitor of SN 2011fe". In: ApJ 744, L17, p. L17.

Bohn, A. et al. (Oct. 2014). "What would a binary black hole merger look like?" In: *ArXiv e-prints*.

Bongard, S. et al. (Nov. 2008). "Multilayered Spectral Formation in Type Ia Supenovae around Maximum Light". In: ApJ 687, pp. 456–465.

Bowers, E. J. C. et al. (Oct. 1997). "Infrared and optical spectroscopy of Type IA supernovae in the nebular phase". In: MNRAS 290, pp. 663–679.

Branch, D., E. Baron, et al. (June 2005). "Comparative Direct Analysis of Type Ia Supernova Spectra. I. SN 1994D". In: PASP 117, pp. 545–552.

Branch, D., J. B. Doggett, et al. (July 1985). "Accreting white dwarf models for the type I supernovae. IV The optical spectrum of a carbon-deflagration supernova". In: ApJ 294, pp. 619–625.

Branch, D., D. J. Jeffery, et al. (Feb. 2008). "Comparative Direct Analysis of Type Ia Supernova Spectra. IV. Postmaximum". In: PASP 120, pp. 135–149.

Branch, D., C. H. Lacy, et al. (July 1983). "The Type I supernova 1981b in NGC 4536 - The first 100 days". In: ApJ 270, pp. 123–125.

Branch, D., M. Livio, et al. (Nov. 1995). "In Search of the Progenitors of Type IA Supernovae". In: PASP 107, p. 1019.

Branch, D. and G. A. Tammann (1992). "Type IA supernovae as standard candles". In: ARA&A 30, pp. 359–389.

Bravo, E. and D. García-Senz (May 2006). "Beyond the Bubble Catastrophe of Type Ia Supernovae: Pulsating Reverse Detonation Models". In: ApJ 642, pp. L157–L160.

— (Apr. 2009). "Pulsating Reverse Detonation Models of Type Ia Supernovae. I. Detonation Ignition". In: ApJ 695, pp. 1244–1256.

Bravo, E., D. García-Senz, et al. (Apr. 2009). "Pulsating Reverse Detonation Models of Type Ia Supernovae. II. Explosion". In: ApJ 695, pp. 1257–1272.

Buchholz, B. et al. (May 1994). "An operator splitting method for atmospheres with shocks". In: A&A 285, pp. 987–994.

Burbidge, E. M. et al. (1957). "Synthesis of the Elements in Stars". In: *Reviews of Modern Physics* 29, pp. 547–650.

Cannon, C. J. (1973a). "Angular quadrature perturbations in radiative transfer theory." In: J. Quant. Spec. Radiat. Transf. 13, pp. 627–633.

— (Oct. 1973b). "Frequency-Quadrature Perturbations in Radiative-Transfer Theory". In: ApJ 185, pp. 621–630.

Cardall, C. Y., E. Endeve, and A. Mezzacappa (May 2013). "Conservative 3+1 general relativistic variable Eddington tensor radiation transport equations". In: Phys. Rev. D 87.10, 103004, p. 103004.

Cardelli, J. A., G. C. Clayton, and J. S. Mathis (Oct. 1989). "The relationship between infrared, optical, and ultraviolet extinction". In: ApJ 345, pp. 245–256.

Carroll, Bradley W. and Dale A. Ostlie (2007). *An Introduction to Modern Astrophysics*. 2nd ed. San Francisco: Pearson Education, Inc.

Castor, J. I. (1970). "Spectral line formation in Wolf-Rayet envelopes." In: MNRAS 149, pp. 111–127.

— (Jan. 2007). *Radiation Hydrodynamics*. Cambridge, UK: Cambridge University Press.

Chan, K.-W. and R. E. Lingenfelter (Feb. 1991). "Gamma-ray lines from type I supernovae". In: ApJ 368, pp. 515–537.

— (Mar. 1993). "Positrons from supernovae". In: ApJ 405, pp. 614–636.

Chen, B., X. Dai, and E. Baron (Jan. 2013). "Inclination-dependent Active Galactic Nucleus Flux Profiles from Strong Lensing of the Kerr Spacetime". In: ApJ 762, 122, p. 122.

Chen, B., X. Dai, E. Baron, and R. Kantowski (June 2013). "Effects of Kerr Strong Gravity on Quasar X-Ray Microlensing". In: ApJ 769, 131, p. 131.

Chen, B., R. Kantowski, et al. (Sept. 2007). "Steps for solving the radiative transfer equation for arbitrary flows in stationary space-times". In: MNRAS 380, pp. 104–112.

Chiosi, E. et al. (Sept. 2014). "Exploring an Alternative Channel of Evolution Towards SNa Ia Explosion". In: *ArXiv e-prints*.

Chomiuk, L. et al. (May 2012). "EVLA Observations Constrain the Environment and Progenitor System of Type Ia Supernova 2011fe". In: ApJ 750, 164, p. 164.

Churazov, E., R. Sunyaev, J. Isern, I. Bikmaev, et al. (Feb. 2015). "Gamma-rays from Type Ia supernova SN2014J". In: *ArXiv e-prints*.

Churazov, E., R. Sunyaev, J. Isern, J. Knödlseder, et al. (Aug. 2014). "Cobalt-56 γ-ray emission lines from the type Ia supernova 2014J". In: Nature 512, pp. 406–408.

Colgate, S. A. and C. McKee (Aug. 1969). "Early Supernova Luminosity". In: ApJ 157, p. 623.

Colgate, S. A., A. G. Petschek, and J. T. Kriese (May 1980). "The luminosity of type I supernovae". In: ApJ 237, pp. L81–L85.

Cushing, M. C., W. D. Vacca, and J. T. Rayner (Apr. 2004). "Spextool: A Spectral Extraction Package for SpeX, a 0.8-5.5 Micron Cross-Dispersed Spectrograph". In: PASP 116, pp. 362–376.

De, S., E. Baron, and P. H. Hauschildt (Sept. 2010a). "Hydrogen recombination with multilevel atoms". In: MNRAS 407, pp. 658–668.

— (Jan. 2010b). "On the hydrogen recombination time in Type II supernova atmospheres". In: MNRAS 401, pp. 2081–2092.

Dessart, L. and D. J. Hillier (July 2005). "Quantitative spectroscopy of photospheric-phase type II supernovae". In: A&A 437, pp. 667–685.

— (July 2010). "Supernova radiative-transfer modelling: a new approach using non-local thermodynamic equilibrium and full time dependence". In: MNRAS 405, pp. 2141–2160.

Dessart, L., D. J. Hillier, et al. (Apr. 2014). "[Co III] versus Na I D in Type Ia supernova spectra". In: MNRAS 439, pp. 3114–3120.

Dexter, J. and E. Agol (May 2009). "A Fast New Public Code for Computing Photon Orbits in a Kerr Spacetime". In: ApJ 696, pp. 1616–1629.

Diamond, T., P. Höflich, and C. L. Gerardy (Oct. 2014). "Late-time near-infrared observations of SN 2005df". In: *ArXiv e-prints*.

Domínguez, I., P. Höflich, and O. Straniero (Aug. 2001). "Constraints on the Progenitors of Type Ia Supernovae and Implications for the Cosmological Equation of State". In: ApJ 557, pp. 279–291.

Dykema, P. G., R. I. Klein, and J. I. Castor (Feb. 1996). "A New Scheme for Multidimensional Line Transfer. III. A Two-dimensional Lagrangian Variable Tensor Method with Discontinuous Finite-Element SN Transport". In: ApJ 457, p. 892.

Fesen, R. A., P. Hoeflich, and A. J. S. Hamilton (Dec. 2014). "The 2D Distribution of Iron Rich Ejecta in the Remnant of SN 1885 in M31". In: *ArXiv e-prints*.

Fesen, R. A., P. Höflich, et al. (Mar. 2007). "The Chemical Distribution in a Subluminous Type Ia Supernova: Hubble Space Telescope Images of the SN 1885 Remnant". In: ApJ 658, pp. 396–409.

Filippenko, A. V. (1997). "Optical Spectra of Supernovae". In: ARA&A 35, pp. 309–355.

Filippenko, A. V. and R. Chornock (Nov. 2001). "Supernova 2001fe in UGC 5129". In: IAU Circ. 7752, p. 3.

Fisher, A. et al. (June 1997). "Evidence for a High-velocity Carbon-rich Layer in the Type IA SN 1990N". In: ApJ 481, pp. L89–L92.

Foley, R. J., O. D. Fox, et al. (Oct. 2014). "Extensive HST ultraviolet spectra and multiwavelength observations of SN 2014J in M82 indicate reddening and circumstellar scattering by typical dust". In: MNRAS 443, pp. 2887–2906.

Foley, R. J. and D. Kasen (Mar. 2011). "Measuring Ejecta Velocity Improves Type Ia Supernova Distances". In: ApJ 729, 55, p. 55.

Foley, R. J., J. D. Simon, et al. (June 2012). "Linking Type Ia Supernova Progenitors and Their Resulting Explosions". In: ApJ 752, 101, p. 101.

Fossey, J. et al. (Jan. 2014). "Supernova 2014J in M82 = Psn J09554214+6940260". In: *Central Bureau Electronic Telegrams* 3792, p. 1.

Fransson, C. (Mar. 1984). "Line profiles from supernovae". In: A&A 132, pp. 115–126.

Frieman, J. A., M. S. Turner, and D. Huterer (Sept. 2008). "Dark Energy and the Accelerating Universe". In: ARA&A 46, pp. 385–432.

Friesen, B., E. Baron, D. Branch, et al. (Nov. 2012). "Supernova Resonance-scattering Line Profiles in the Absence of a Photosphere". In: ApJS 203, 12, p. 12.

Friesen, B., E. Baron, J. P. Wisniewski, et al. (Sept. 2014). "Near-infrared Line Identification in Type Ia Supernovae during the Transitional Phase". In: ApJ 792, 120, p. 120.

Gall, E. E. E. et al. (Dec. 2012). "Interpreting the near-infrared spectra of the 'golden standard' Type Ia supernova 2005cf". In: MNRAS 427, pp. 994–1003.

Gamezo, V. N. et al. (Jan. 2003). "Thermonuclear Supernovae: Simulations of the Deflagration Stage and Their Implications". In: *Science* 299, pp. 77–81.

Gardner, Jonathan P. et al. (2006). "The James Webb Space Telescope". In: *Space Science Reviews* 123.4, pp. 485–606. ISSN: 0038-6308. URL: http://dx.doi.org/10.1007/s11214-006-8315-7.

Gerardy, C. L., P. Höflich, et al. (May 2004). "SN 2003du: Signatures of the Circumstellar Environment in a Normal Type Ia Supernova?" In: ApJ 607, pp. 391–405.

Gerardy, C. L., W. P. S. Meikle, et al. (June 2007). "Signatures of Delayed Detonation, Asymmetry, and Electron Capture in the Mid-Infrared Spectra of Supernovae 2003hv and 2005df". In: ApJ 661, pp. 995–1012.

Goobar, A. et al. (Mar. 2014). "The Rise of SN 2014J in the Nearby Galaxy M82". In: ApJ 784, L12, p. L12.

Graham, M. L. et al. (Jan. 2015). "Constraining the Progenitor Companion of the Nearby Type Ia SN 2011fe with a Kiloday Nebular Spectrum". In: *ArXiv e-prints*.

Hachinger, S., P. A. Mazzali, and S. Benetti (July 2006). "Exploring the spectroscopic diversity of Type Ia supernovae". In: MNRAS 370, pp. 299–318.

Hamann, W.-R. and G. Gräfener (Nov. 2003). "A temperature correction method for expanding atmospheres". In: A&A 410, pp. 993–1000.

Hamuy, M., J. Maza, et al. (July 2002). "Optical and Infrared Spectroscopy of SN 1999ee and SN 1999ex". In: AJ 124, pp. 417–429.

Hamuy, M., M. M. Phillips, et al. (Dec. 1996). "The Absolute Luminosities of the Calan/Tololo Type IA Supernovae". In: AJ 112, p. 2391.

Hatano, K., D. Branch, A. Fisher, E. Baron, et al. (Nov. 1999). "On the High-Velocity Ejecta of the Type IA Supernova SN 1994D". In: ApJ 525, pp. 881–885.

Hatano, K., D. Branch, A. Fisher, J. Millard, et al. (Mar. 1999). "Ion Signatures in Supernova Spectra". In: ApJS 121, pp. 233–246.

Hauschildt, P. H. (June 1992a). "A fast operator perturbation method for the solution of the special relativistic equation of radiative transfer in spherical symmetry". In: J. Quant. Spec. Radiat. Transf. 47, pp. 433–453.

— (Oct. 1992b). "Radiative equilibrium in rapidly expanding shells". In: ApJ 398, pp. 224–233.

— (Sept. 1993). "Multi-level non-LTE radiative transfer in expanding shells." In: J. Quant. Spec. Radiat. Transf. 50, pp. 301–318.

Hauschildt, P. H., F. Allard, et al. (Oct. 1997). "Non–Local Thermodynamic Equilibrium Effects of TI i in M Dwarfs and Giants". In: ApJ 488, p. 428.

Hauschildt, P. H. and E. Baron (Dec. 1995). "Non-LTE treatment of Fe II in astrophysical plasmas." In: J. Quant. Spec. Radiat. Transf. 54, pp. 987–999.

— (Sept. 1999). "Numerical solution of the expanding stellar atmosphere problem." In: *Journal of Computational and Applied Mathematics* 109, pp. 41–63.

— (May 2006). "A 3D radiative transfer framework. I. Non-local operator splitting and continuum scattering problems". In: A&A 451, pp. 273–284.

— (June 2014). "A 3D radiative transfer framework. XI. Multi-level NLTE". In: A&A 566, A89, A89.

Hauschildt, P. H., E. Baron, et al. (May 1996). "The Effects of Fe II Non-LTE on Nova Atmospheres and Spectra". In: ApJ 462, p. 386.

Hauschildt, P. H., M. Best, and R. Wehrse (July 1991). "Relativistic effects in supernova photospheres". In: A&A 247, pp. L21–L24.

Hauschildt, P. H. and L. M. Ensman (Apr. 1994). "Analysis of the early spectra and light curve of SN 1987A". In: ApJ 424, pp. 905–923.

Hauschildt, P. H., S. Starrfield, S. Austin, et al. (Feb. 1994). "Non-LTE model atmosphere analysis of Nova Cygni 1992". In: ApJ 422, pp. 831–844.

Hauschildt, P. H., S. Starrfield, S. N. Shore, et al. (July 1995). "The Physics of Early Nova Spectra". In: ApJ 447, p. 829.

Hauschildt, P. H. and R. Wehrse (Aug. 1991). "Solution of the special relativistic equation of radiative transfer in rapidly expanding spherical shells". In: J. Quant. Spec. Radiat. Transf. 46, pp. 81–98.

Hayes, J. C. and M. L. Norman (July 2003). "Beyond Flux-limited Diffusion: Parallel Algorithms for Multidimensional Radiation Hydrodynamics". In: ApJS 147, pp. 197–220.

Hillier, D. J. (May 1990). "An iterative method for the solution of the statistical and radiative equilibrium equations in expanding atmospheres". In: A&A 231, pp. 116–124.

Hillier, D. J. and L. Dessart (July 2012). "Time-dependent radiative transfer calculations for supernovae". In: MNRAS 424, pp. 252–271.

Höflich, P. (July 2002). "Gamma-rays as probes for the multi-dimensionality of type Ia supernovae". In: New A Rev. 46, pp. 475–480.

Höflich, P. (Jan. 2003). "ALI in Rapidly Expanding Envelopes". In: *Stellar Atmosphere Modeling*. Ed. by I. Hubeny, D. Mihalas, and K. Werner. Vol. 288. Astronomical Society of the Pacific Conference Series, p. 185.

— (Oct. 2006). "Physics of type Ia supernovae". In: *Nuclear Physics A* 777, pp. 579–600.

Höflich, P., C. L. Gerardy, R. A. Fesen, et al. (Apr. 2002). "Infrared Spectra of the Subluminous Type Ia Supernova SN 1999by". In: ApJ 568, pp. 791–806.

Höflich, P., C. L. Gerardy, K. Nomoto, et al. (Dec. 2004). "Signature of Electron Capture in Iron-rich Ejecta of SN 2003du". In: ApJ 617, pp. 1258–1266.

Höflich, P., A. M. Khokhlov, and J. C. Wheeler (May 1995). "Delayed detonation models for normal and subluminous type IA sueprnovae: Absolute brightness, light curves, and molecule formation". In: ApJ 444, pp. 831–847.

Höflich, P., A. Khokhlov, and E. Müller (June 1992). "Gamma-ray light curves and spectra for Type IA supernovae". In: A&A 259, pp. 549–566.

— (June 1994). "Gamma-ray light curves and spectra of models for Type IA supernovae". In: ApJS 92, pp. 501–504.

Höflich, P., K. Krisciunas, et al. (Feb. 2010). "Secondary Parameters of Type Ia Supernova Light Curves". In: ApJ 710, pp. 444–455.

Höflich, P., E. Mueller, and A. Khokhlov (Feb. 1993). "Light curve models for type IA supernovae - Physical assumptions, their influence and validity". In: A&A 268, pp. 570–590.

Höflich, P., R. Wehrse, and G. Shaviv (July 1986). "Non-LTE effects in low-density scattering-dominated photospheres". In: A&A 163, pp. 105–113.

Höflich, P., J. C. Wheeler, and A. Khokhlov (Jan. 1998). "Hard X-Rays and Gamma Rays from Type IA Supernovae". In: ApJ 492, pp. 228–245.

Horesh, A. et al. (Feb. 2012). "Early Radio and X-Ray Observations of the Youngest nearby Type Ia Supernova PTF 11kly (SN 2011fe)". In: ApJ 746, 21, p. 21.

Hoyle, F. and W. A. Fowler (Nov. 1960). "Nucleosynthesis in Supernovae." In: ApJ 132, p. 565.

Hsiao, E. Y. et al. (Apr. 2013). "The Earliest Near-infrared Time-series Spectroscopy of a Type Ia Supernova". In: ApJ 766, 72, p. 72.

Hubeny, I. and T. Lanz (Feb. 1995). "Non-LTE line-blanketed model atmospheres of hot stars. 1: Hybrid complete linearization/accelerated lambda iteration method". In: ApJ 439, pp. 875–904.

Hummer, D. G. and D. Mihalas (Aug. 1988). "The equation of state for stellar envelopes. I - an occupation probability formalism for the truncation of internal partition functions". In: ApJ 331, pp. 794–814.

Husser, T.-O. et al. (May 2013). "A new extensive library of PHOENIX stellar atmospheres and synthetic spectra". In: A&A 553, A6, A6.

Iben Jr., I. and A. V. Tutukov (Feb. 1984). "Supernovae of type I as end products of the evolution of binaries with components of moderate initial mass (M not greater than about 9 solar masses)". In: ApJS 54, pp. 335–372.

Iwamoto, K. et al. (Dec. 1999). "Nucleosynthesis in Chandrasekhar Mass Models for Type IA Supernovae and Constraints on Progenitor Systems and Burning-Front Propagation". In: ApJS 125, pp. 439–462.

Jack, D., P. H. Hauschildt, and E. Baron (Aug. 2009). "Time-dependent radiative transfer with PHOENIX". In: A&A 502, pp. 1043–1049.

— (Apr. 2011). "Theoretical light curves of type Ia supernovae". In: A&A 528, A141, A141.

— (Oct. 2012a). "A 3D radiative transfer framework. IX. Time dependence". In: A&A 546, A39, A39.

— (Feb. 2012b). "Near-infrared light curves of type Ia supernovae". In: A&A 538, A132, A132.

— (Jan. 2013). "Time-dependent radiative transfer with PHOENIX (Corrigendum)". In: A&A 549, C1, p. C1.

Janka, H.-T. (Nov. 2012). "Explosion Mechanisms of Core-Collapse Supernovae". In: *Annual Review of Nuclear and Particle Science* 62, pp. 407–451.

Jeffery, D. J. and D. Branch (1990). "Analysis of Supernova Spectra". In: *Supernovae, Jerusalem Winter School for Theoretical Physics*. Ed. by J. C. Wheeler, T. Piran, and S. Weinberg, p. 149.

Jeffery, D. J., W. Ketchum, et al. (Aug. 2007). "Goodness-of-Fit Tests DIFF1 and DIFF2 for Locally Normalized Supernova Spectra". In: ApJS 171, pp. 493–511.

Jeffery, D. J., B. Leibundgut, et al. (Sept. 1992). "Analysis of the photospheric epoch spectra of type 1a supernovae SN 1990N and SN 1991T". In: ApJ 397, pp. 304–328.

Jerkstrand, A., C. Fransson, and C. Kozma (June 2011). "The ^{44}Ti-powered spectrum of SN 1987A". In: A&A 530, A45, A45.

Jha, S. et al. (July 2006). "Late-Time Spectroscopy of SN 2002cx: The Prototype of a New Subclass of Type Ia Supernovae". In: AJ 132, pp. 189–196.

Jones, H. R. A., A. J. Longmore, F. Allard, and P. H. Hauschildt (May 1996). "Spectral analysis of M dwarfs". In: MNRAS 280, pp. 77–94.

Jones, H. R. A., A. J. Longmore, F. Allard, P. H. Hauschildt, et al. (Dec. 1995). "Water vapour in cool dwarf stars". In: MNRAS 277, pp. 767–776.

Kasen, D., P. E. Nugent, et al. (Aug. 2003). "Analysis of the Flux and Polarization Spectra of the Type Ia Supernova SN 2001el: Exploring the Geometry of the High-Velocity Ejecta". In: ApJ 593, pp. 788–808.

Kasen, D., R. C. Thomas, and P. E. Nugent (Nov. 2006). "Time-dependent Monte Carlo Radiative Transfer Calculations for Three-dimensional Supernova Spectra, Light Curves, and Polarization". In: ApJ 651, pp. 366–380.

Khokhlov, A., E. Müller, and P. Höflich (Mar. 1993). "Light curves of Type IA supernova models with different explosion mechanisms". In: A&A 270, pp. 223–248.

Kirshner, R. P. and J. B. Oke (Sept. 1975). "Supernova 1972e in NGC 5253". In: ApJ 200, pp. 574–581.

Knop, S. (2007). "General Relativistic Radiative Transfer". PhD thesis. Universität Hamburg.

Knop, S., P. H. Hauschildt, and E. Baron (Feb. 2007). "General relativistic radiative transfer". In: A&A 463, pp. 315–320.

Kozma, C. and C. Fransson (May 1992). "Gamma-ray deposition and nonthermal excitation in supernovae". In: ApJ 390, pp. 602–621.

— (Mar. 1998a). "Late Spectral Evolution of SN 1987A. I. Temperature and Ionization". In: ApJ 496, pp. 946–966.

— (Apr. 1998b). "Late Spectral Evolution of SN 1987A. II. Line Emission". In: ApJ 497, pp. 431–457.

Kozma, C., C. Fransson, et al. (July 2005). "Three-dimensional modeling of type Ia supernovae - The power of late time spectra". In: A&A 437, pp. 983–995.

Kramida, A. et al. (2013). *NIST Atomic Spectra Database*. Version 5.1. National Institute of Standards and Technology. URL: `http://physics.nist.gov/asd` (visited on 05/14/2014).

Krisciunas, K., M. M. Phillips, and N. B. Suntzeff (Feb. 2004). "Hubble Diagrams of Type Ia Supernovae in the Near-Infrared". In: ApJ 602, pp. L81–L84.

Kromer, M. and S. A. Sim (Oct. 2009). "Time-dependent three-dimensional spectrum synthesis for Type Ia supernovae". In: MNRAS 398, pp. 1809–1826.

Krueger, B. K., A. P. Jackson, A. C. Calder, et al. (Oct. 2012). "Evaluating Systematic Dependencies of Type Ia Supernovae: The Influence of Central Density". In: ApJ 757, 175, p. 175.

Krueger, B. K., A. P. Jackson, D. M. Townsley, et al. (Aug. 2010). "On Variations of the Brightness of Type Ia Supernovae with the Age of the Host Stellar Population". In: ApJ 719, pp. L5–L9.

Kuchner, M. J. et al. (May 1994). "Evidence for Ni-56 yields Co-56 yields Fe-56 decay in type IA supernovae". In: ApJ 426, p. L89.

Kurucz, R. L. (1995). "The Kurucz Smithsonian Atomic and Molecular Database". In: *Astrophysical Applications of Powerful New Databases*. Ed. by S. J. Adelman and W. L. Wiese. Vol. 78. Astronomical Society of the Pacific Conference Series, p. 205.

— (Oct. 2002). "Atomic and Molecular Data Needs for Astrophysics". In: *Atomic and Molecular Data and Their Applications*. Ed. by D. R. Schultz, P. S. Krstic, and F. Ownby. Vol. 636. American Institute of Physics Conference Series, pp. 134–143.

— (Apr. 2011). "Including all the lines". In: *Canadian Journal of Physics* 89, pp. 417–428.

Leggett, S. K. et al. (May 1996). "Infrared Spectra of Low-Mass Stars: Toward a Temperature Scale for Red Dwarfs". In: ApJS 104, p. 117.

Leloudas, G. et al. (Oct. 2009). "The normal Type Ia SN 2003hv out to very late phases". In: A&A 505, pp. 265–279.

Lentz, E. J. et al. (Feb. 2000). "Metallicity Effects in Non-LTE Model Atmospheres of Type IA Supernovae". In: ApJ 530, pp. 966–976.

Li, C., D. J. Hillier, and L. Dessart (Oct. 2012). "Non-thermal excitation and ionization in supernovae". In: MNRAS 426, pp. 1671–1686.

Li, W. et al. (Dec. 2011). "Exclusion of a luminous red giant as a companion star to the progenitor of supernova SN 2011fe". In: Nature 480, pp. 348–350.

Loch, S. et al. (July 2013). "The propagation of uncertainties in atomic data through collisional-radiative models". In: *American Institute of Physics Conference Series*. Ed. by J. D. Gillaspy, W. L. Wiese, and Y. A. Podpaly. Vol. 1545. American Institute of Physics Conference Series, pp. 242–251.

Löffler, F. et al. (June 2012). "The Einstein Toolkit: a community computational infrastructure for relativistic astrophysics". In: *Classical and Quantum Gravity* 29.11, 115001, p. 115001.

Lotz, W. (May 1967). "Electron-Impact Ionization Cross-Sections and Ionization Rate Coefficients for Atoms and Ions". In: ApJS 14, p. 207.

Lucy, L. B. (Dec. 1964). "A Temperature-Correction Procedure". In: *SAO Special Report* 167, p. 93.

Lundqvist, P. and C. Fransson (June 1996). "The Line Emission from the Circumstellar Gas around SN 1987A". In: ApJ 464, p. 924.

Maeda, K., S. Benetti, et al. (July 2010). "An asymmetric explosion as the origin of spectral evolution diversity in type Ia supernovae". In: Nature 466, pp. 82–85.

Maeda, K., G. Leloudas, et al. (June 2011). "Effects of the explosion asymmetry and viewing angle on the Type Ia supernova colour and luminosity calibration". In: MNRAS 413, pp. 3075–3094.

Maeda, K., K. Nomoto, et al. (Apr. 2006). "Nebular Spectra of SN 1998bw Revisited: Detailed Study by One- and Two-dimensional Models". In: ApJ 640, pp. 854–877.

Malone, C. M. et al. (Feb. 2014). "The Deflagration Stage of Chandrasekhar Mass Models for Type Ia Supernovae. I. Early Evolution". In: ApJ 782, 11, p. 11.

Mandel, K. S., G. Narayan, and R. P. Kirshner (Apr. 2011). "Type Ia Supernova Light Curve Inference: Hierarchical Models in the Optical and Near-infrared". In: ApJ 731, 120, p. 120.

Margutti, R. et al. (June 2012). "Inverse Compton X-Ray Emission from Supernovae with Compact Progenitors: Application to SN2011fe". In: ApJ 751, 134, p. 134.

Marion, G. H., P. Höflich, C. L. Gerardy, et al. (Sept. 2009). "A Catalog of Near-Infrared Spectra from Type Ia Supernovae". In: AJ 138, pp. 727–757.

Marion, G. H., P. Höflich, W. D. Vacca, et al. (July 2003). "Near-Infrared Spectra of Type Ia Supernovae". In: ApJ 591, pp. 316–333.

Marion, G. H., D. J. Sand, et al. (Jan. 2015). "Early Observations and Analysis of the Type Ia SN 2014J in M82". In: ApJ 798, 39, p. 39.

Maund, J. R., P. Höflich, et al. (Dec. 2010). "The Unification of Asymmetry Signatures of Type Ia Supernovae". In: ApJ 725, pp. L167–L171.

Maund, J. R., J. Spyromilio, et al. (June 2013). "Spectropolarimetry of the Type Ia supernova 2012fr". In: MNRAS 433, pp. L20–L24.

Maurer, I. et al. (Dec. 2011). "NERO- a post-maximum supernova radiation transport code". In: MNRAS 418, pp. 1517–1525.

Mazzali, P. A. (Nov. 2000). "Applications of an improved Monte Carlo code to the synthesis of early-time Supernova spectra". In: A&A 363, pp. 705–716.

— (Feb. 2001). "On the presence of silicon and carbon in the pre-maximum spectrum of the Type Ia SN 1990N". In: MNRAS 321, pp. 341–346.

Mazzali, P. A., S. Benetti, et al. (Apr. 2005). "High-Velocity Features: A Ubiquitous Property of Type Ia Supernovae". In: ApJ 623, pp. L37–L40.

Mazzali, P. A., E. Cappellaro, et al. (May 1998). "Nebular Velocities in Type IA Supernovae and Their Relationship to Light Curves". In: ApJ 499, pp. L49–L52.

Mazzali, P. A., I. J. Danziger, and M. Turatto (May 1995). "A study of the properties of the peculiar SN IA 1991T through models of its evolving early-time spectrum." In: A&A 297, p. 509.

Mazzali, P. A. and S. Hachinger (Aug. 2012). "The nebular spectra of the Type Ia supernova 1991bg: further evidence of a non-standard explosion". In: MNRAS 424, pp. 2926–2935.

Mazzali, P. A. and L. B. Lucy (Nov. 1993). "The application of Monte Carlo methods to the synthesis of early-time supernovae spectra". In: A&A 279, pp. 447–456.

Mazzali, P. A., I. Maurer, et al. (Sept. 2011). "The nebular spectrum of the Type Ia supernova 2003hv: evidence for a non-standard event". In: MNRAS 416, pp. 881–892.

Mazzali, P. A., D. N. Sauer, et al. (June 2008). "Abundance stratification in Type Ia supernovae - II. The rapidly declining, spectroscopically normal SN2004eo". In: MNRAS 386, pp. 1897–1906.

Meikle, W. P. S. et al. (July 1996). "An early-time infrared and optical study of the Type IA supernovae SN 1994D and 1991T". In: MNRAS 281, pp. 263–280.

Meyerott, R. E. (May 1978). "On the interpretation of the spectra of Type I supernovae". In: ApJ 221, pp. 975–989.

— (July 1980). "A radioactive excitation source model for the late time spectra of Type I supernovae". In: ApJ 239, pp. 257–270.

Mihalas, D. (Jan. 1965). "Model Atmospheres and Line Profiles for Early-Type Stars." In: ApJS 9, p. 321.

— (1970). *Stellar Atmospheres*. 1st ed. San Francisco, CA: W. H. Freeman and Co.

Mihalas, D. (1978). *Stellar Atmospheres*. 2nd ed. San Francisco, CA: W. H. Freeman and Co.

— (Apr. 1980). "Solution of the comoving-frame equation of transfer in spherically symmetric flows. VI - Relativistic flows". In: ApJ 237, pp. 574–589.

Mihalas, D., P. B. Kunasz, and D. G. Hummer (Dec. 1975). "Solution of the comoving frame equation of transfer in spherically symmetric flows. I - Computational method for equivalent-two-level-atom source functions". In: ApJ 202, pp. 465–489.

Mihalas, D. and B. Weibel-Mihalas (1999). *Foundations of Radiation Hydrodynamics*. Mineola, NY: Dover.

Motohara, K. et al. (Dec. 2006). "The Asymmetric Explosion of Type Ia Supernovae as Seen from Near-Infrared Observations". In: ApJ 652, pp. L101–L104.

Munari, U. et al. (Apr. 2013). "BVRI lightcurves of supernovae SN 2011fe in M101, SN 2012aw in M95, and SN 2012cg in NGC 4424". In: New A 20, pp. 30–37.

Niemeyer, J. C. (Sept. 1999). "Can Deflagration-Detonation Transitions Occur in Type IA Supernovae?" In: ApJ 523, pp. L57–L60.

Nomoto, K., F.-K. Thielemann, and K. Yokoi (Nov. 1984). "Accreting white dwarf models of Type I supernovae. III - Carbon deflagration supernovae". In: ApJ 286, pp. 644–658.

Nonaka, A. et al. (Jan. 2012). "High-resolution Simulations of Convection Preceding Ignition in Type Ia Supernovae Using Adaptive Mesh Refinement". In: ApJ 745, 73, p. 73.

Nugent, P. E., E. Baron, D. Branch, et al. (Aug. 1997). "Synthetic Spectra of Hydrodynamic Models of Type IA Supernovae". In: ApJ 485, p. 812.

Nugent, P. E., E. Baron, P. H. Hauschildt, et al. (Mar. 1995). "Spectrum synthesis of the Type IA supernovae SN 1992A and SN 1981B". In: ApJ 441, pp. L33–L36.

Nugent, P. E., M. M. Phillips, et al. (Dec. 1995). "Evidence for a Spectroscopic Sequence among Type 1a Supernovae". In: ApJ 455, p. L147.

Nugent, P. E., M. Sullivan, et al. (Dec. 2011). "Supernova SN 2011fe from an exploding carbon-oxygen white dwarf star". In: Nature 480, pp. 344–347.

Ohlmann, S. T. et al. (Sept. 2014). "The white dwarf's carbon fraction as a secondary parameter of Type Ia supernovae". In: *ArXiv e-prints*.

Olson, G. L. and P. B. Kunasz (1987). "Short characteristic solution of the non-LTE transfer problem by operator perturbation. I. The one-dimensional planar slab." In: J. Quant. Spec. Radiat. Transf. 38, pp. 325–336.

Osterbrock, Donald E. and Gary J. Ferland (2006). *Astrophysics of Gaseous Nebulae and Active Galactic Nuclei*. 2nd ed. Sausalito, CA: University Science Books.

Pakmor, R. et al. (Mar. 2012). "Normal Type Ia Supernovae from Violent Mergers of White Dwarf Binaries". In: ApJ 747, L10, p. L10.

Parrent, J. T., B. Friesen, and M. Parthasarathy (May 2014). "A review of type Ia supernova spectra". In: Ap&SS 351, pp. 1–52.

Parrent, J. T., D. A. Howell, et al. (June 2012). "Analysis of the Early-time Optical Spectra of SN 2011fe in M101". In: ApJ 752, L26, p. L26.

Penney, R. and P. Höflich (Nov. 2014). "Thermonuclear Supernovae: Probing Magnetic Fields by Positrons and Late-time IR Line Profiles". In: ApJ 795, 84, p. 84.

Pereira, R. et al. (June 2013). "Spectrophotometric time series of SN 2011fe from the Nearby Supernova Factory". In: A&A 554, A27, A27.

Perlmutter, S. et al. (June 1999). "Measurements of Ω and Λ from 42 High-Redshift Supernovae". In: ApJ 517, pp. 565–586.

Phillips, M. M. (Aug. 1993). "The absolute magnitudes of Type IA supernovae". In: ApJ 413, pp. L105–L108.

Phillips, M. M., P. Garnavich, et al. (June 2006). "The Joint Efficient Dark-energy Investigation (JEDI): measuring the cosmic expansion history from type Ia supernovae". In: *Society of Photo-Optical Instrumentation Engineers (SPIE) Conference Series*. Vol. 6265. Society of Photo-Optical Instrumentation Engineers (SPIE) Conference Series, p. 2.

Phillips, M. M., P. Lira, et al. (Oct. 1999). "The Reddening-Free Decline Rate Versus Luminosity Relationship for Type IA Supernovae". In: AJ 118, pp. 1766–1776.

Pinto, P. A. and R. G. Eastman (Feb. 2000). "The Physics of Type IA Supernova Light Curves. II. Opacity and Diffusion". In: ApJ 530, pp. 757–776.

Press, William H. et al. (2007). *Numerical Recipes: The Art of Scientific Computing*. 3rd ed. Cambridge, NY: Cambridge University Press.

Pritchet, C. J., D. A. Howell, and M. Sullivan (Aug. 2008). "The Progenitors of Type Ia Supernovae". In: ApJ 683, pp. L25–L28.

Ramsey, J. P. and C. P. Dullemond (Feb. 2015). "Radiation hydrodynamics including irradiation and adaptive mesh refinement with AZEuS. I. Methods". In: A&A 574, A81, A81.

Richmond, M. W. and H. A. Smith (Apr. 2012). "BVRI Photometry of SN 2011fe in M101". In: *Journal of the American Association of Variable Star Observers (JAAVSO)* 40, p. 872.

Riess, A. G. et al. (Sept. 1998). "Observational Evidence from Supernovae for an Accelerating Universe and a Cosmological Constant". In: AJ 116, pp. 1009–1038.

Röpke, F. K. (Mar. 2005). "Following multi-dimensional type Ia supernova explosion models to homologous expansion". In: A&A 432, pp. 969–983.

Röpke, F. K., W. Hillebrandt, et al. (Mar. 2006). "Multi-spot ignition in type Ia supernova models". In: A&A 448, pp. 1–14.

Röpke, F. K., M. Kromer, et al. (May 2012). "Constraining Type Ia Supernova Models: SN 2011fe as a Test Case". In: ApJ 750, L19, p. L19.

Ruiz-Lapuente, P., R. P. Kirshner, et al. (Jan. 1995). "Late-time spectra and type IA supernova models: New clues from the Hubble Space Telescope". In: ApJ 439, pp. 60–73.

Ruiz-Lapuente, P. and L. B. Lucy (Nov. 1992). "Nebular spectra of type IA supernovae as probes for extragalactic distances, reddening, and nucleosynthesis". In: ApJ 400, pp. 127–137.

Rybicki, G. B. and D. G. Hummer (May 1991). "An accelerated lambda iteration method for multilevel radiative transfer. I - Non-overlapping lines with background continuum". In: A&A 245, pp. 171–181.

— (Aug. 1992). "An accelerated lambda iteration method for multilevel radiative transfer. II - Overlapping transitions with full continuum". In: A&A 262, pp. 209–215.

— (Oct. 1994). "An accelerated lambda iteration method for multilevel radiative transfer. III. Noncoherent electron scattering". In: A&A 290, pp. 553–562.

Sauer, D. N. et al. (Dec. 2008). "Properties of the ultraviolet flux of Type Ia supernovae: an analysis with synthetic spectra of SN 2001ep and SN 2001eh". In: MNRAS 391, pp. 1605–1618.

Savitzky, Abraham. and M. J. E. Golay (1964). "Smoothing and Differentiation of Data by Simplified Least Squares Procedures." In: *Analytical Chemistry* 36.8, pp. 1627–1639. URL: http://dx.doi.org/10.1021/ac60214a047.

Schinder, P. J. (Sept. 1988). "General-relativistic radiation hydrodynamics and neutrino transport in polar-sliced space-time". In: Phys. Rev. D 38, pp. 1673–1683.

Schinder, P. J. and S. A. Bludman (Nov. 1989). "Radiative transport in spherical static spacetime - General relativistic tangent-ray method for the variable Eddington factors". In: ApJ 346, pp. 350–365.

Schwarz, G. J. et al. (Jan. 1997). "Non-LTE model atmosphere analysis of the early ultraviolet spectra of Nova OS Andromedae 1986". In: MNRAS 284, pp. 669–684.

Schweitzer, A. et al. (Dec. 1996). "Analysis of Keck high-resolution spectra of VB 10". In: MNRAS 283, pp. 821–829.

Seaton, M. J. (1968). "Atomic Collision Processes in Gaseous Nebulae". In: *Advances in Atomic and Molecular Physics* 4, pp. 331–380.

— (1976). "Electron Impact Excitation of Positive Ions". In: *Advances in Atomic and Molecular Physics* 11, pp. 83–142.

Sedra, Adel S. and Kenneth C. Smith (2009). *Microelectronic Circuits*. 6th ed. Oxford University Press.

Seitenzahl, I. R., G. Cescutti, et al. (Nov. 2013). "Solar abundance of manganese: a case for near Chandrasekhar-mass Type Ia supernova progenitors". In: A&A 559, L5, p. L5.

Seitenzahl, I. R., F. Ciaraldi-Schoolmann, and F. K. Röpke (July 2011). "Type Ia supernova diversity: white dwarf central density as a secondary parameter in three-dimensional delayed detonation models". In: MNRAS 414, pp. 2709–2715.

Shappee, B. J. et al. (Jan. 2013). "No Stripped Hydrogen in the Nebular Spectra of Nearby Type Ia Supernova 2011fe". In: ApJ 762, L5, p. L5.

Shaviv, G., R. Wehrse, and R. V. Wagoner (Feb. 1985). "Predicted continuum spectra of type II supernovae - LTE results". In: ApJ 289, pp. 198–202.

Shen, K. J. and L. Bildsten (Apr. 2014). "The Ignition of Carbon Detonations via Converging Shock Waves in White Dwarfs". In: ApJ 785, 61, p. 61.

Short, C. I., P. H. Hauschildt, and E. Baron (Nov. 1999). "Massive Multispecies, Multilevel Non-LTE Model Atmospheres for Novae in Outburst". In: ApJ 525, pp. 375–385.

Shu, F. H. (1982). *The Physical Universe*. Sausalito, CA: University Science Books.

Silverman, J. M., M. Ganeshalingam, and A. V. Filippenko (Apr. 2013). "Berkeley Supernova Ia Program - V. Late-time spectra of Type Ia Supernovae". In: MNRAS 430, pp. 1030–1041.

Smith, William R. and Ronald W. Missen (1982). *Chemical Reaction Equilibrium Analysis*. 1st ed. New York, NY: Wiley.

Soker, N. (Jan. 2013). "The Core-Degenerate Scenario for Type Ia Supernovae". In: *IAU Symposium*. Ed. by R. Di Stefano, M. Orio, and M. Moe. Vol. 281. IAU Symposium, pp. 72–75.

Spyromilio, J. et al. (Oct. 1992). "A large mass of iron in supernova 1991T". In: MNRAS 258, 53P–56P.

Stanishev, V. et al. (July 2007). "SN 2003du: 480 days in the life of a normal type Ia supernova". In: A&A 469, pp. 645–661.

Stoerzer, H., P. H. Hauschildt, and F. Allard (Dec. 1994). "Non-LTE effects on the strength of the Lyman edge in quasar accretion disks". In: ApJ 437, pp. L91–L94.

Stritzinger, M. et al. (Apr. 2006). "Constraints on the progenitor systems of type Ia supernovae". In: A&A 450, pp. 241–251.

Sumiyoshi, K. et al. (Jan. 2015). "Multi-dimensional Features of Neutrino Transfer in Core-collapse Supernovae". In: ApJS 216, 5, p. 5.

Sutherland, P. G. and J. C. Wheeler (May 1984). "Models for Type I supernovae - Partially incinerated white dwarfs". In: ApJ 280, pp. 282–297.

Swartz, D. A., P. G. Sutherland, and R. P. Harkness (June 1995). "Gamma-Ray Transfer and Energy Deposition in Supernovae". In: ApJ 446, p. 766.

Tanaka, M. et al. (Jan. 2011). "Abundance stratification in Type Ia supernovae - III. The normal SN 2003du". In: MNRAS 410, pp. 1725–1738.

Taubenberger, S. et al. (Mar. 2015). "Spectroscopy of the Type Ia supernova 2011fe past 1000 d". In: MNRAS 448, pp. L48–L52.

Telesco, C. M. et al. (Sept. 2014). "Mid-IR Spectra of Type Ia SN 2014J in M82 Spanning the First Four Months". In: *ArXiv e-prints*.

The Nobel Prize in Physics 2011 (2013). Nobel Media AB. URL: `http://www.nobelprize.org/nobel_prizes/physics/laureates/2011/` (visited on 05/20/2014).

Thielemann, F.-K., K. Nomoto, and K. Yokoi (Apr. 1986). "Explosive nucleosynthesis in carbon deflagration models of Type I supernovae". In: A&A 158, pp. 17–33.

Thomas, R. C., P. E. Nugent, and J. C. Meza (Feb. 2011). "SYNAPPS: Data-Driven Analysis for Supernova Spectroscopy". In: PASP 123, pp. 237–248.

Thornburg, J. (June 2007). "Event and Apparent Horizon Finders for 3+1 Numerical Relativity". In: *Living Reviews in Relativity* 10, p. 3.

Timmes, F. X., E. F. Brown, and J. W. Truran (June 2003). "On Variations in the Peak Luminosity of Type Ia Supernovae". In: ApJ 590, pp. L83–L86.

Timmes, F. X. and F. D. Swesty (Feb. 2000). "The Accuracy, Consistency, and Speed of an Electron-Positron Equation of State Based on Table Interpolation of the Helmholtz Free Energy". In: ApJS 126, pp. 501–516.

Travaglio, C. et al. (Oct. 2004). "Nucleosynthesis in multi-dimensional SN Ia explosions". In: A&A 425, pp. 1029–1040.

Truran, J. W., W. D. Arnett, and A. G. W. Cameron (1967). "Nucleosynthesis in supernova shock waves". In: *Canadian Journal of Physics* 45, p. 2315.

Unsöld, Albrecht (Nov. 1951). "Ein rasch konvergierendes Iterationsverfahren zur Lösung von Strahlungsgleichgewichts-Problemen". In: *Naturwissenschaften* 38, pp. 525–526.

— (1955). *Physik der Sternatmosphären*. 2nd ed. New York, Heidelberg: Springer-Verlag Berlin.

Vacca, W. D., M. C. Cushing, and J. T. Rayner (Mar. 2003). "A Method of Correcting Near-Infrared Spectra for Telluric Absorption". In: PASP 115, pp. 389–409.

van Kerkwijk, M. H., P. Chang, and S. Justham (Oct. 2010). "Sub-Chandrasekhar White Dwarf Mergers as the Progenitors of Type Ia Supernovae". In: ApJ 722, pp. L157–L161.

van Regemorter, H. (Nov. 1962). "Rate of Collisional Excitation in Stellar Atmospheres." In: ApJ 136, p. 906.

van Rossum, D. R. (Sept. 2012). "Radiation Energy Balance Method for Calculating the Time Evolution of Type Ia Supernovae during the Post-explosion Phase". In: ApJ 756, 31, p. 31.

Vincent, F. H., E. Gourgoulhon, and J. Novak (Dec. 2012). "3+1 geodesic equation and images in numerical spacetimes". In: *Classical and Quantum Gravity* 29.24, 245005, p. 245005.

Vinkó, J. et al. (Oct. 2012). "Testing supernovae Ia distance measurement methods with SN 2011fe". In: A&A 546, A12, A12.

Wang, X. et al. (July 2009). "Improved Distances to Type Ia Supernovae with Two Spectroscopic Subclasses". In: ApJ 699, pp. L139–L143.

Wang, Y. (2010). *Dark Energy*. Weinheim: Wiley-VCH.

Webbink, R. F. (Feb. 1984). "Double white dwarfs as progenitors of R Coronae Borealis stars and Type I supernovae". In: ApJ 277, pp. 355–360.

Weinberg, S. (June 1995). *The Quantum Theory of Fields*. Vol. 1. Cambridge, UK: Cambridge University Press.

Wheeler, J. C. (Oct. 2012). "White Dwarf/M Dwarf Binaries as Single Degenerate Progenitors of Type Ia Supernovae". In: ApJ 758, 123, p. 123.

Wheeler, J. C. et al. (Mar. 1998). "Explosion Diagnostics of Type IA Supernovae from Early Infrared Spectra". In: ApJ 496, pp. 908–914.

Whelan, J. and I. Iben Jr. (Dec. 1973). "Binaries and Supernovae of Type I". In: ApJ 186, pp. 1007–1014.

Wood-Vasey, W. M. et al. (Dec. 2008). "Type Ia Supernovae Are Good Standard Candles in the Near Infrared: Evidence from PAIRITEL". In: ApJ 689, pp. 377–390.

Woosley, S. E. and D. Kasen (June 2011). "Sub-Chandrasekhar Mass Models for Supernovae". In: ApJ 734, 38, p. 38.

Woosley, S. E., D. Kasen, et al. (June 2007). "Type Ia Supernova Light Curves". In: ApJ 662, pp. 487–503.

Woosley, S. E. and T. A. Weaver (Mar. 1994). "Sub-Chandrasekhar mass models for Type IA supernovae". In: ApJ 423, pp. 371–379.

Xu, Y. and R. McCray (July 1991). "Energy degradation of fast electrons in hydrogen gas". In: ApJ 375, pp. 190–201.

Yaron, O. and A. Gal-Yam (July 2012). "WISeREP - An Interactive Supernova Data Repository". In: PASP 124, pp. 668–681.

Young, T. R. (Jan. 1994). "Light curve studies of type 2 and type Ib/Ic supernovae". PhD thesis. Oklahoma University.

Young, T. R., E. Baron, and D. Branch (1993). "Supernova 1984L and its problematic progenitor". In: *Nuclear Physics in the Universe*. Ed. by M. W. Guidry and M. R. Strayer, pp. 399–409.

— (Aug. 1995). "Light Curve Studies of SN 1993J and SN 1994I". In: ApJ 449, p. L51.

Zheng, W. et al. (Mar. 2014). “Estimating the First-light Time of the Type Ia Supernova 2014J in M82”. In: ApJ 783, L24, p. L24.

Appendix A

$S(r)$ outside the core

In Section 2.4 we calculate sample spectra for lines forming outside the glowing core. Therefore, we calculate the source function in the region $r > r_c$. From Figure A.1:

$$Y = r\mu - \left(r^2\mu^2 + r_c^2 - r^2\right)^{1/2}.$$

Then

$$X = (X + Y) - Y = 2\left(r^2\mu^2 + r_c^2 - r^2\right)^{1/2}. \tag{A.1}$$

We plug the expression for X into Equation 2.5, noting that, because the shell emits no continuum, the maximum value of θ is not 1, as in the $r \leq r_c$ case, but rather

$$\theta_{\max} = \cos^{-1}\left(\frac{(r^2 - r_c^2)^{1/2}}{r}\right).$$

Thus,

$$J(r) = \frac{1}{2}\int_{\mu_0}^{1} 2\left(r^2\mu^2 + r_c^2 - r^2\right)^{1/2} d\mu,$$

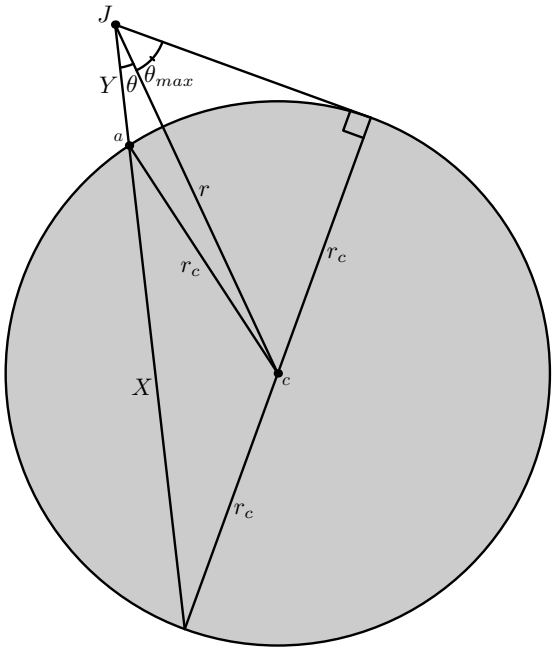

Figure A.1: Geometric configuration used to calculate $S(r > r_c)$ in the absence of lines in the core.

where μ_0 is the argument of the inverse cosine above. The result is

$$\begin{aligned} J(r) = & \quad \frac{1}{2r}\left\{ rr_c + (r^2 - r_c^2)\ln\left[\frac{\sqrt{r^2 - r_c^2}}{r + r_c}\right]\right\} \\ = & \quad \frac{1}{2r}\left\{ rr_c + \frac{(r^2 - r_c^2)}{2}\ln\left[\frac{r - r_c}{r + r_c}\right]\right\}. \end{aligned}$$

The mean intensities inside and outside the core are identical except for two sign differences: one in the factor multiplying the logarithm, and the other in the argument of the logarithm itself. We find that Equation (2.7) and Equation (2.8) are continuous at the edge of the core, as they must be, each yielding $J(r = r_c) = 0.5r_c$.

Appendix B

Two lines

We now turn to the two-line case. We denote these lines as R and B, for "red" and "blue." First, as stated previously, the source function for the blue line, S_B, is given by Equation (2.7). The source function for the red line, $S_R(r)$, is equal to the mean intensity $J_\lambda(r)$, where λ is the rest wavelength of the line λ_{0_R}. The calculation of J is complicated by the fact that photons emitted by the blue line may be scattered into resonance with the red line, while some continuum photons from the glowing core which would, in the absence of the blue line, redshift into resonance with the red line are actually scattered away by the blue line. In velocity space the region where the blue line interacts with the red line takes the form of a "scattering sphere" called the *common point velocity surface* (CPVS) (Jeffery and Branch 1990). The radius of the CPVS, denoted Y in Figure B.1, is given by the Doppler formula, Equation (2.14), where one replaces z in that equation with Y. In Section B.1 we study the interaction of two lines confined to the core, and in Section B.2 we explore two lines in the shell.

B.1 Two lines inside the core

When both lines are confined to the core, S_R contains three components:

1. the intensity of continuum photons which can redshift into resonance with

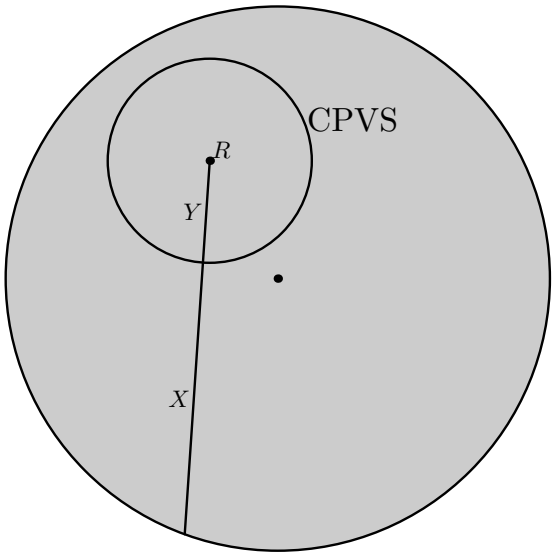

Figure B.1: The different components of an intensity ray incident on the red line in the two-line case.

R, but are scattered away when they reach the CPVS;

2. photons emitted by B along the CPVS which redshift into resonance with R;

3. continuum photons which form *inside* the CPVS and therefore redshift into resonance with R without interacting with B.

Segments 1 and 3 are labeled X and Y respectively in Figure B.1. Mathematically we write this as

$$S_R = \frac{1}{2}\int_{-1}^{1} X e^{-\tau_B} d\mu + \frac{1}{2}\int_{-1}^{1} S_B(1 - e^{-\tau_B}) d\mu + \frac{1}{2}\int_{-1}^{1} Y d\mu. \qquad \text{(B.1)}$$

To calculate $X = X(\mu)$ we refer to Figure B.2. Defining the triangle ABC in

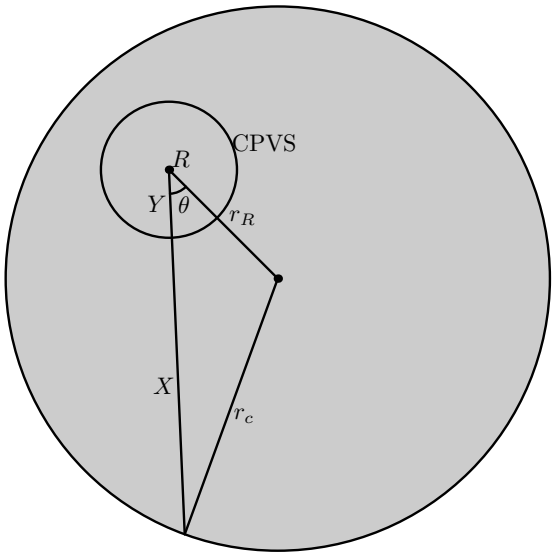

Figure B.2: Explicit geometric construction of two-line configuration used to calculate $X = X(\mu)$.

Figure B.2, we can use the law of cosines to find:

$$r_c^2 = (X+Y)^2 + r_R^2 - 2(X+Y)r_R\mu \tag{B.2}$$

where we have used the fact that X and Y are co-linear and $\mu = \cos\theta$. Solving for X,

$$X = (r_R\mu - Y) \pm \sqrt{(r_R\mu - Y)^2 + r_c^2 - r_R^2 + 2Yr_R\mu}. \tag{B.3}$$

Expanding the square root yields

$$\sqrt{(r_R\mu - Y)^2 + r_c^2 - r_R^2 + 2Yr_R\mu} = \sqrt{r_c^2 - r_R^2(1-\mu^2) + Y^2}. \tag{B.4}$$

When $-1 \leq \mu \leq Y/r_R$, we see that $(r_R\mu - Y) < 0$ and we must take the positive root in Equation (B.3). However, when $Y/r_R < \mu \leq 1$ we see from Equation (B.3)

that $\mu > 0$ and thus the term in the square root is larger than the expression $r_R\mu - Y$ and so the positive root is also correct. Hence,

$$X = (r_R\mu - Y) + \sqrt{r_c^2 - r_R^2(1-\mu^2) + Y^2}, \tag{B.5}$$

for $-1 \leq \mu \leq 1$. Before proceeding we note that if the CPVS extends past the edge of the core, that is, if $r_R + Y > r_c$, then there exists a critical angle $\theta_{\rm crit}$ for which X becomes undefined if $\theta > \theta_{\rm crit}$. Its value is

$$\mu_{\rm crit} = \frac{Y^2 + r_R^2 - 1}{2Y r_R}, \tag{B.6}$$

where $\mu_{\rm crit} \equiv \cos\theta_{\rm crit}$. When integrating to find the contribution of the CPVS to the source function of the red line, S_R, we must stop the integration at this angle. This limit is depicted in Figure B.3.

Next, we must calculate $r_{S_B} = r_{S_B}(\mu)$, the location of the CPVS, as shown in Figure B.4. Again through vector addition arguments we find

$$r_{S_B}(\mu) = (r_R^2 + Y^2 - 2r_R Y\mu)^{1/2}. \tag{B.7}$$

It is at this location r_{S_B} that both τ_B and S_B in Equation (B.1) are evaluated. Lastly we turn to the calculation of Y in Figure B.1. If the entire CPVS fits inside the core, we may use the Doppler formula, Equation (2.14), to calculate Y for all θ. However, if part of the CPVS extends past the edge of the core then Y takes a slightly more complicated form. This latter case is shown in Figure B.5,

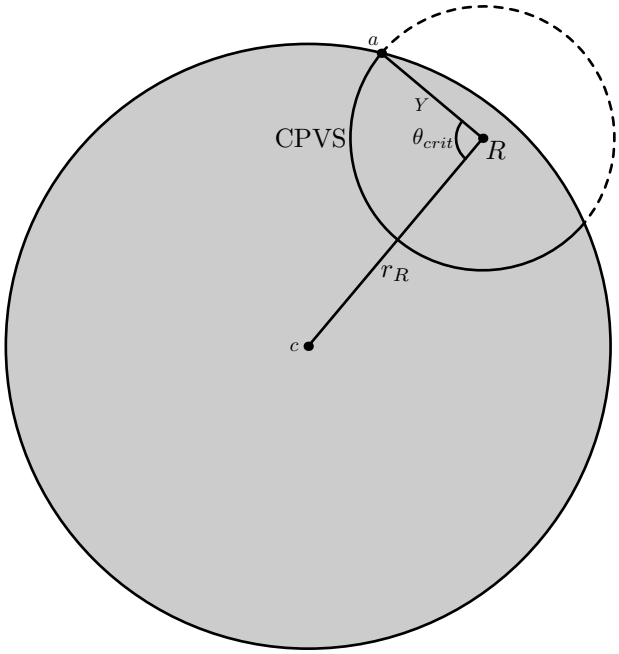

Figure B.3: Geometric construction of angle θ_{crit}. The value r_R is the magnitude of the vector $\overrightarrow{cR}$, and Y is that of $\overrightarrow{aR}$.

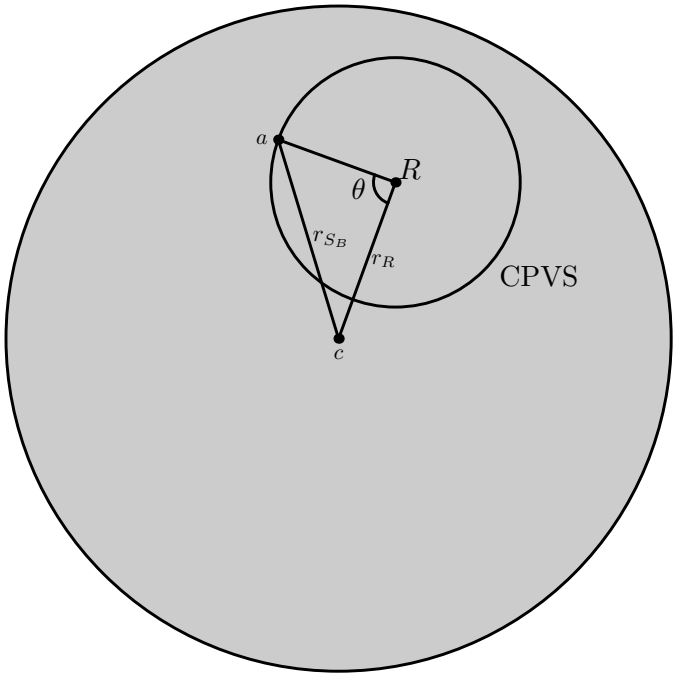

Figure B.4: Calculation of location of CPVS, labeled r_{S_B}, with respect to the center of the SN. The quantity r_R is the magnitude of the vector $\overrightarrow{cR}$, and r_{S_B} is that of $\overrightarrow{ac}$.

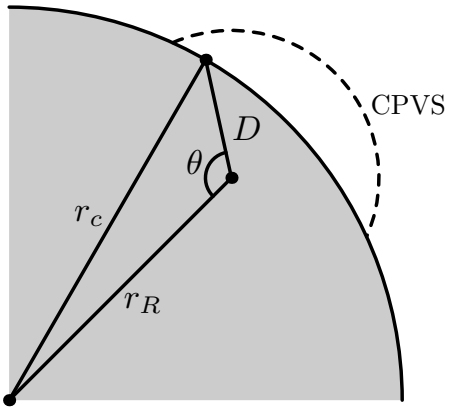

Figure B.5: Geometric configuration of truncated intensity ray $D = D(\mu)$.

where $\theta_1 > \theta_{\rm crit}$. We calculated this angle in Equation (B.6). If $\theta > \theta_{\rm crit}$ then, from Figure B.5,

$$D(\mu) = r_R\mu \pm (r_R^2\mu^2 + r_c^2 - r_R^2)^{1/2}. \tag{B.8}$$

Since D is a length and must always satisfy $D \geq 0$ we can rule out immediately the "minus" solution, since it is negative for all possible values of (r_R, Y, μ). Thus we take the positive root:

$$D(\mu) = r_R\mu + (r_R^2\mu^2 + r_c^2 - r_R^2)^{1/2} \qquad -1 \leq \mu \leq \mu_{\rm crit}. \tag{B.9}$$

B.2 Two lines outside the core

In the case that we have a resonance line that is strong under cold conditions, for example, certain lines of Ca II or Mg II, we may want to consider multiple lines forming outside the core. Figure B.6 illustrates the most complex case. If $\theta > \theta_{\rm crit}$, where $\mu_{\rm crit} = \cos(\theta_{\rm crit}) = 1 - (r_c/r_R)^2$, then the characteristic in that direction does not intersect the core and accumulates no intensity, but for

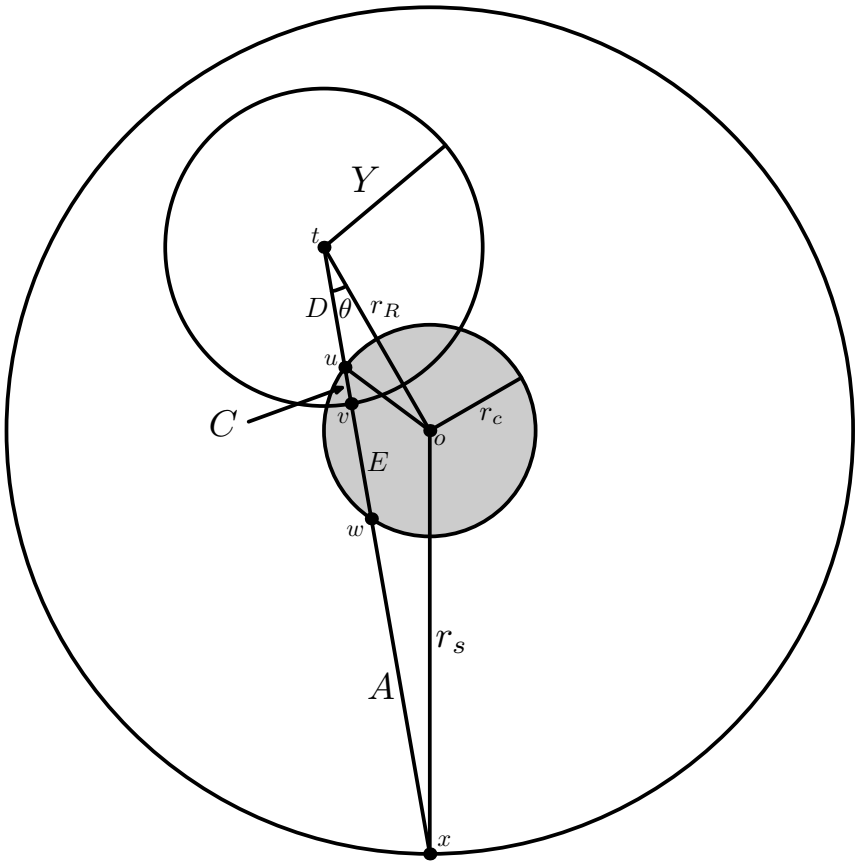

Figure B.6: Case I geometry. The value of A corresponds to the magnitude of the vector $\overrightarrow{xw}$, E to $\overrightarrow{wv}$, C to $\overrightarrow{vu}$, D to $\overrightarrow{ut}$, r_c to $\overrightarrow{ou}$, and r_s to $\overrightarrow{xo}$. Only E and C contribute to the intensity of the ray since A and D lie outside the emitting core.

the case that $\mu \geq \mu_{\text{crit}}$ then the characteristic is given as shown in Cases I–III, (Figure B.6–Figure B.8).

For Case I, Figure B.6, we find

$$D = r_R \cos\theta - \sqrt{r_c^2 - r_R^2 \sin^2\theta}, \tag{B.10}$$

$$C = Y - D = Y - r_R \cos\theta + \sqrt{r_c^2 - r_R^2 \sin^2\theta}, \tag{B.11}$$

$$E = 2(r_R \cos\theta - D) - C = \sqrt{r_c^2 - r_R^2 \sin^2\theta} - Y + r_R \cos\theta, \tag{B.12}$$

and

$$A = \sqrt{r_s^2 - r_R^2 \sin^2\theta} - \sqrt{r_c^2 - r_R^2 \sin^2\theta}. \tag{B.13}$$

For Case II, Figure B.7, we have

$$E = 2\sqrt{r_c^2 - r_R^2 \sin^2\theta} \tag{B.14}$$

$$C = r_R \cos\theta - Y - \sqrt{r_c^2 - r_R^2 \sin^2\theta} \tag{B.15}$$

$$A = \sqrt{r_s^2 - r_R^2 \sin^2\theta} - \sqrt{r_c^2 - r_R^2 \sin^2\theta} \tag{B.16}$$

and

$$D = Y. \tag{B.17}$$

For Case III, Figure B.8,

$$D = r_R \cos\theta - \sqrt{r_c^2 - r_R^2 \sin^2\theta} \tag{B.18}$$

$$C = 2\sqrt{r_c^2 - r_R^2 \sin^2\theta} \tag{B.19}$$

$$E = Y - D - C = Y - \sqrt{r_c^2 - r_R^2 \sin^2\theta} - r_R \cos\theta. \tag{B.20}$$

and

$$A = \sqrt{r_s^2 - r_R^2 \sin^2\theta} + r_R \cos\theta - Y. \tag{B.21}$$

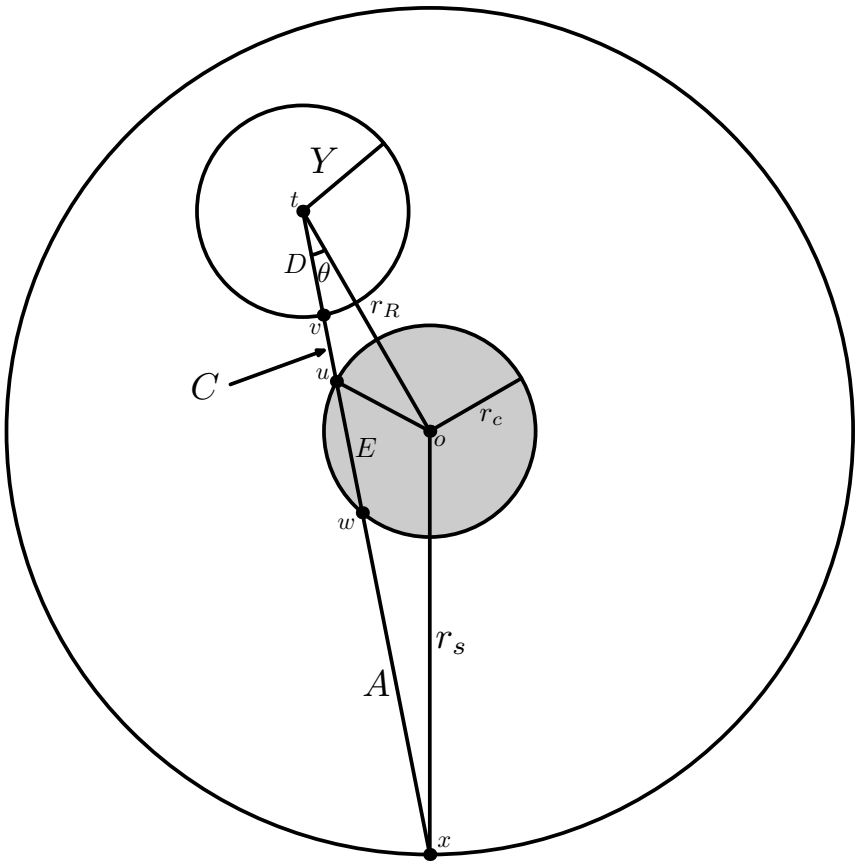

Figure B.7: Case II geometry. The value of A corresponds to the magnitude of the vector $\overrightarrow{xw}$, E to $\overrightarrow{wu}$, C to $\overrightarrow{uv}$, D to $\overrightarrow{ut}$, r_c to $\overrightarrow{ou}$, and r_s to $\overrightarrow{xo}$. Only E contributes to the intensity of the ray since A, C, and D lie outside the emitting core.

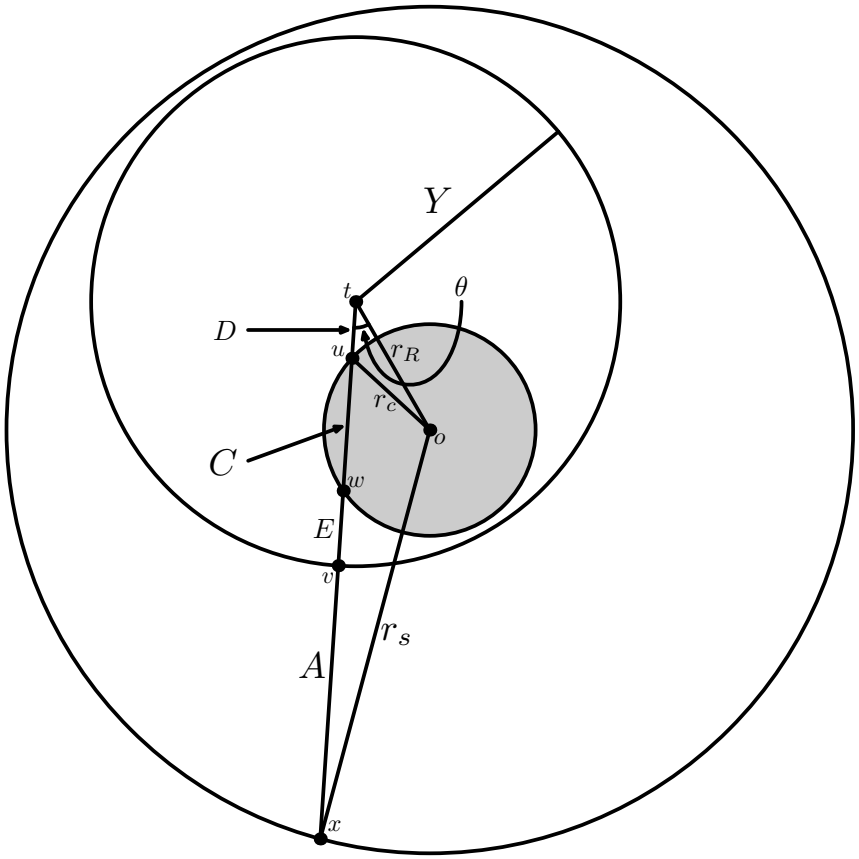

Figure B.8: Case III geometry. The value of A corresponds to the magnitude of the vector $\overrightarrow{xb}$, E to $\overrightarrow{vb}$, C to $\overrightarrow{wu}$, D to $\overrightarrow{ut}$, r_c to $\overrightarrow{ou}$, and r_s to $\overrightarrow{xo}$. Only C contributes to the intensity of the ray since A, E, and D lie outside the emitting core.

Then J for Case I is:

$$J = \frac{1}{2}\left\{\int_{-1}^{\mu_{\rm crit}} S_B(1-e^{-\tau_B})\,d\mu + \int_{\mu_{\rm crit}}^{1}\left[Ee^{-\tau_B} + S_B(1-e^{-\tau_B}) + C\right]\,d\mu\right\}. \tag{B.22}$$

For Case II, J is:

$$J = \frac{1}{2}\left\{\int_{-1}^{\mu_{\rm crit}} S_B(1-e^{-\tau_B})\,d\mu + \int_{\mu_{\rm crit}}^{1}\left[Ee^{-\tau_B} + S_B(1-e^{-\tau_B})\right]\,d\mu\right\}. \tag{B.23}$$

Finally, for Case III,

$$J = \frac{1}{2}\left\{\int_{-1}^{\mu_{\rm crit}} S_B(1-e^{-\tau_B})\,d\mu + \int_{\mu_{\rm crit}}^{1}\left[E + S_B(1-e^{-\tau_B})\right]\,d\mu\right\} \tag{B.24}$$

The extension of the two-line case to the N-line case is straightforward and is implemented most easily in a recursive fashion, moving along wavelength as the value of r_R increases.

B.2.1 Calculation of emergent intensity

Given that the flux integral in Equation (2.4) can be written as an integral over impact parameter p, we concern ourselves here with the calculation of the emergent intensity of rays with constant p, denoted $I_\lambda(p)$. We first calculate the domain $[z_{\rm min}, z_{\rm max}]$ over which a ray with given p exists:

$$\begin{aligned} z_{\rm min} &= -(r_c^2 - p^2)^{1/2} \\ z_{\rm max} &= +(r_c^2 - p^2)^{1/2} \end{aligned}$$

We then use the Doppler formula to establish the wavelength domain $[\lambda_{\min}, \lambda_{\max}]$ over which it is possible for a particular wavelength point λ to be in resonance in the core, given p:

$$\lambda_{\min} = \frac{\lambda}{1 + z_{\max}\left(\frac{v_{\text{core}}}{c}\right)} \tag{B.25}$$

$$\lambda_{\max} = \frac{\lambda}{1 + z_{\min}\left(\frac{v_{\text{core}}}{c}\right)}. \tag{B.26}$$

All lines with rest wavelength λ_0 which lie in this domain will be in resonance with the ray $I_\lambda(p)$ at some location in the core.

Now consider a ray with two lines which both fall in the domain $[\lambda_{\min}, \lambda_{\max}]$. The ray redshifts into resonance with the blue line "before" (at larger z, closer to the back of the core) redshifting into resonance with the red line; we denote these locations z_B and z_R, respectively, where $z_B > z_R$. The segment of the ray between the back edge of the core and z_B has intensity $(r_c^2 - p^2)^{1/2} - z_B$. However it will redshift into resonance with *both* lines before emerging from the core, so it acquires two attenuation terms, $e^{-\tau_B}$ and $e^{-\tau_R}$, where τ_B and τ_R are evaluated at z_B and z_R, respectively. The continuum segment between z_R and z_B has length $z_B - z_R$ and is attenuated only by the red line. The front-most continuum piece, between z_R and the front of the core, is unaffected by scattering and has intensity $(r_c^2 - p^2)^{1/2} + z_R$.

The source functions of the red and blue lines also contribute to the total emergent intensity. The contribution from each is $S_i(1 - e^{-\tau_i})$, where $i \in \{R, B\}$. However the blue line's contribution will be attenuated when it redshifts into

resonance with the red line, and so it is receives the usual $e^{-\tau_R}$ multiplicative factor. Therefore the total emergent intensity is

$$\begin{aligned} I_\lambda(p) = &((r_c^2 - p^2)^{1/2} - z_B)e^{-\tau_B}e^{-\tau_R} + S_B(1 - e^{-\tau_B})e^{-\tau_R} \\ &+ (z_B - z_R)e^{-\tau_R} + S_R(1 - e^{-\tau_R}) + (r_c^2 - p^2)^{1/2} + z_R. \end{aligned} \tag{B.27}$$

If for a particular ray one of the two lines is outside $[\lambda_{\min}, \lambda_{\max}]$, the result for $I_\lambda(p)$ reduces to the one-line form for $I_\lambda(p)$ of Equation (2.10) or Equation (2.15), Equation (2.17), and Equation (2.18) for lines outside the core. It is important to understand that if, for some impact parameter p, the blue line has wavelength outside $[\lambda_{\min}, \lambda_{\max}]$, such that $I_\lambda(p)$ is given by Equation (2.10), the source function $S = S_R$ evaluated in that equation may nevertheless contain scattering effects of the blue line, as long as at least some portion of the CPVS for the blue line lines within the core.

If both lines fall outside this domain the emergent intensity becomes the pure continuum result.

Appendix C

Details of root-finding methods for enforcing radiative equilibrium

Despite the success of the Unsöld-Lucy method in calculations of near-maximum light supernova spectra, we found that it often yields nonsensical temperature corrections in the post-maximum light regime, e.g., decreasing the temperature by 10 000 K in one zone but increasing it by 100 K in an adjacent zone, where the optical depth is nearly the same. The problem may be numerical in nature, but it may also reside within the physical assumptions the Unsöld-Lucy scheme makes. We consequently developed an alternative method which produced better results at this epoch in a primarily optically thin environment such as the ejecta of supernovae at later times. The algorithm consists of solving the $\mathcal{O}(v/c)$ energy equation, integrated over wavelength:

$$\frac{v}{c}\frac{\partial J}{\partial r} + \frac{1}{r^2}\frac{\partial (r^2 H)}{\partial r} + \frac{v}{c}\frac{1}{r}(3J - K) + \frac{\partial (v/c)}{\partial r}(J + K) = \int_0^\infty \kappa_\lambda (B_\lambda - J_\lambda) d\lambda - \frac{\dot{S}}{4\pi}. \tag{C.1}$$

Direct solutions of the energy equation to balance heating and cooling effects works well in diffuse planetary nebulae, where the probability of a photon (almost always from a forbidden emission line) being reabsorbed before escaping the gas

is nearly zero (Osterbrock and Ferland 2006). Although one-year-old SNe Ia are not as rarefied as planetary nebulae, and thus the coupling among different layers of the ejecta is likely considerable, the method may still show promise.

Equation (C.1) is non-linear in T and thus one must use a numerical root-finder to solve it. Nominally, one can calculate the global temperature structure of the ejecta with the following logical algorithm:

1. Choose an initial temperature guesses at each point.

2. Converge the solutions of the RTE, the NLTE rate equations, and the EOS.

3. Use a root finding algorithm to choose the next guess for the temperature at each point based on the information in Equation (C.1).

4. Repeat steps 2–3 until the temperature has converged.

However, a number of features of the RTE complicate this algorithm considerably. One such feature is the implicit non-locality of the temperature. Root-finders are iterative, and proceed by making educated guesses based on certain criteria. But because the value of T which satisfies Equation (C.1) depends implicitly on the values of T in every other computational zone, and because these iterative guesses for T proceed independently of one another, each iteration actually changes the problem being solved. In other words, for given J, H, K, χ, η, etc., in all zones $j \neq i$, there exists a value of T which satisfies Equation (C.1) in zone i; but because the correct temperatures in *all* zones are simultaneously unknown, each iteration changes the value of T which satisfies Equation (C.1) in every zone. We

can not be sure that the T which is "correct" in zone i after some iteration is the physically correct result until T is found in *all* zones such that Equation (C.1) is satisfied everywhere simultaneously. In effect, then, the root-finder is attempting to strike a moving target. This pathology, being physical in nature rather than numerical, is independent of the actual root-finding procedure which is used.

A second complicating factor is the notion that temperature is *never* the only independent variable which changes during a root-find. If a root-finding algorithm picks two temperatures which straddle an ionization front of an abundant ion such as Fe II, this sudden change in ionization will dramatically change the opacities, which in turn change the values of the radiation field moments which are used in Equation (C.1) to solve for T. As before, the only reliable way to avoid this is to guess values for T which are already close to the correct answer.

C.1 Bisection method

Given the complexity of the temperature problem, we tested a number of different root-finding algorithms. All of them require writing Equation (C.1) with all terms moved to one side,

$$f(T) \equiv \frac{v}{c}\frac{\partial J}{\partial r} + \frac{1}{r^2}\frac{\partial (r^2 H)}{\partial r} + \frac{v}{c}\frac{1}{r}(3J - K) + \frac{\partial (v/c)}{\partial r}(J + K) - \int_0^\infty \kappa_\lambda (B_\lambda - J_\lambda) d\lambda + \frac{\dot{S}}{4\pi}, \tag{C.2}$$

such that Equation (C.1) is satisfied when $f(T) = 0$. First, we tried one of the simplest: the bisection method. This requires lower and upper limits for T as

"boundary conditions", and then alternates between sampling the value of the midpoint of the bracket and halving the size of the bracket based on the sign of the function sampled at that midpoint (Press et al. 2007). However, this procedure frequently failed in our calculations, because the first steps of bracketing methods consist of evaluating the function under scrutiny at both the imposed low and high limits of T. But unless these brackets are already very close to the correct value of T (in every zone!), the large or small values of T will change the problem so much that the algorithm will become stuck at either end and will never know to search between them. Stated another way, if the "moving target" ever crosses either bracket, the bisection method will attempt to chase it, but it is by design unable to pass the bracketed value, and becomes stuck. Figure C.1 illustrates this effect, showing the "converged" temperature structure using two different upper limits for the temperature. The dots indicate zones in which the bisection algorithm remained "stuck" at the upper bracketed temperature, unable to evaluate lower temperatures in subsequent iterations. This bracketing pathology of the bisection method is to our knowledge unavoidable for this particular problem.

C.2 Secant method

The next approach we tested was the secant method. This is similar to Newton's method, which consists of repeated application of the formula

$$x_n = x_{n-1} - \frac{f(x_{n-1})}{f'(x_{n-1})} \tag{C.3}$$

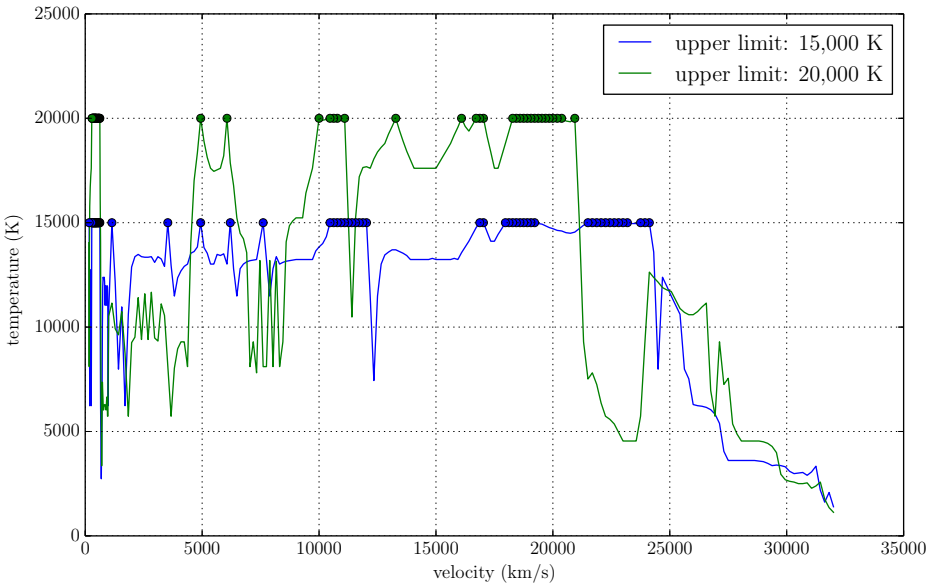

Figure C.1: Temperature structure of models with upper bisection brackets of 15 000 K and 20 000 K. The dots label grid points at which the temperature reaches the upper bracket of the bisection, indicating that the bisection likely does not contain the physical root.

where x_n is the predicted value of the root of $f(x)$ after the nth iteration, and $f'(x_n) \equiv \frac{df}{dx}|_{x=x_n}$. Newton's method is a viable option only when the derivative df/dx is analytic. If it is not, one can instead use the secant method, which is just Equation (C.3), but with a finite-difference approximation applied to the $f'(x)$ term:

$$x_n = x_{n-1} - f(x_{n-1}) \left[\frac{f(x_{n-1}) - f(x_{n-2})}{x_{n-1} - x_{n-2}} \right]^{-1} \tag{C.4}$$

The casualty of using numerical derivatives is that the secant method requires *two* initial guesses for x_n instead of one. In the context of temperature calculations, $f(T)$ as defined in Equation (C.2) contains terms which are obtained iteratively (the radiation moments, among others), and thus analytic derivatives such as

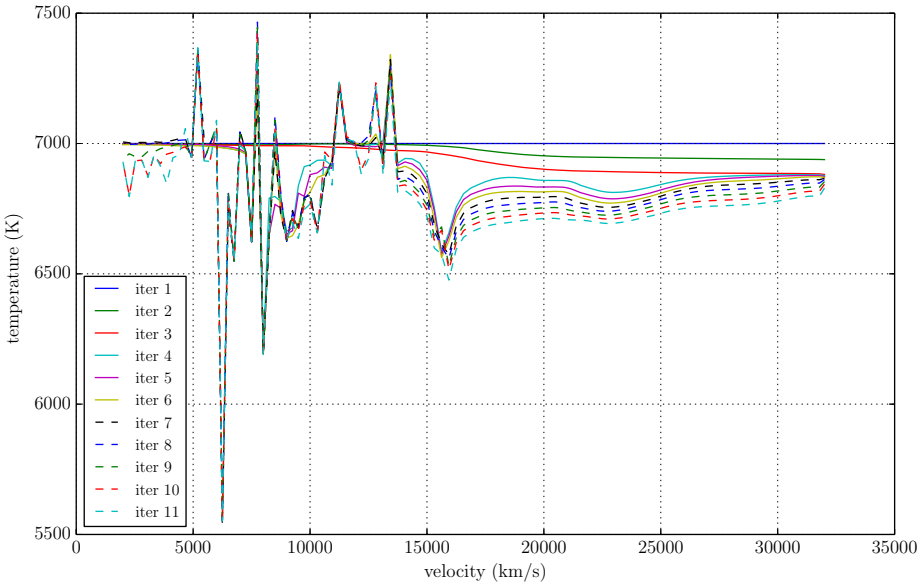

Figure C.2: Temperature structure as a function of iteration. using the secant method. All corrections are damped by 2^5.

$\partial J/\partial T$ are difficult to obtain (although see Hauschildt 1992b, for a clever way to determine this derivative using the ALI operators). As such, Newton's method is unavailable for solving for $f(T)$, and we were instead relegated to using the secant method. However, the secant method shares most of the advantages (superlinear convergence) and disadvantages (instability) of Newton's method, and we discovered in practice that in the context of solving Equation (C.2), this approach to finding the root of $f(T)$ is *extremely* unstable. For example, Figure C.2 shows the temperature evolution with iteration using the secant method with a damping factor of 2^5 applied to each temperature correction value. We believe this is due to the high sensitivity of $f(T)$ on T itself. Besides being highly non-linear, it also subject to abrupt changes in opacity which occur when the temperature crosses an "ionization front" of an important ion such as Fe. These

large opacity changes lead to large changes in the radiation field moments, which in turn lead to sudden changes in $f(T)$. Frequently this manifests as unexpected changes in the slope of $f(T)$, which the secant method (and Newton's method) uses to find the root, leading the algorithm in the wrong direction.

The instability of the secant method is unfortunate, but we discovered a somewhat *ad hoc* procedure which uses the slope-tracking property of the secant method, but avoids some of the instability described above. Specifically, rather than letting $\Delta T \equiv T_n - T_{n-1}$ be a variable quantity, we set it to a fixed value, but set the sign of that value to be the same as the sign that ΔT would otherwise have. We found through experimentation that a fixed value of $|\Delta T_{\rm fixed}| = 100$ K, which is a few percent of the characteristic gas temperature of 5000 K worked well. Then after each iteration the temperature correction in each zone would be

$$\Delta T_{\rm fixed} = 100 \text{ K} * \text{sgn}(\Delta T). \tag{C.5}$$

where ΔT is calculated using the traditional secant method. The disadvantage of using a fixed value for each temperature correction is that the procedure will never formally converge; if the algorithm does "find" the root, it will simply oscillate back and forth around it. Determining convergence with this procedure is therefore a quintessentially human endeavor: one must observe the history of iterations and note the point at which the oscillations begin.

An additional complication in our calculations is that this procedure is applied to each of 128 layers in the supernova ejecta model independently of one another.

We thus needed to be sure that each calculation performed enough iterations for the changes in, e.g., the innermost layer, had enough "time" (iterations) to "diffuse" through the model to the outermost layer. That is, it was not uncommon to observe one layer at one edge of the model oscillating back and forth around a certain value of T, seemingly indicating convergence, while another layer far away was still marching in one direction, indicating that it had *not* converged. Eventually, when the latter started to oscillate, we need to be sure that (nearly) all layers were oscillating as well. Only then could we be confident that global convergence of Equation (C.1) was achieved.

There were more complications as well. Equation (C.1) makes no guarantee that only a single global solution for $f(T)$ exists. However we found that the above described method for solving for $f(T)$ showed some sensitivity to the initial guesses for T at each point, i.e., the method appeared to converge to different values for different initial guesses. This could be because $f(T)$ in some number of zones had local but not global minima, a phenomenon to which derivative-based root-finders are susceptible. That the root-finder stabilized in these local extrema could have led to mathematically consistent but non-physical results in other zones. In fact the only reason we suspected that these results might not be correct was that the synthetic spectra they produced did not match observed spectra; indeed, we encountered so many mathematical and numerical problems with solving Equation (C.1) that the appearance of the spectrum became one of the only reliable gauges for the "correctness" of the solution.

Ultimately, even when this quasi-secant method appeared to converge, the

resulting temperature structures remain somewhat "noisy"(cf. Figure 3.6), likely more so than the actual temperature distribution in late-time SNe Ia. This problem became amplified when we attempted to perform time-dependent calculations in order to rectify the ion recombination problems described above. (De et al. (2010a,b) implemented the ability for the `PHOENIX` code to calculate ion populations with full time-dependence.) Since each new time step in a time-dependent calculation requires converged data from the previous time step, the noise becomes amplified as the calculation takes more time steps. For example, a pair of example calculations, one including time-dependence and the other neglecting it, is shown in Figure C.3. Both results are somewhat "noisy," but the time-dependent calculation is especially so, which may be responsible for the poor fits to the later optical spectra of SN 2011fe. The corresponding synthetic spectra comparing the time-dependent and time-independent rates are shown in Figure C.4.

C.3 The radiation energy balance method of van Rossum (2012)

Although we obtained fairly good results for our model spectra at late times with the root-finding method described in Chapter 3, there are several reasons to suspect that it may not be the best method for enforcing radiative equilibrium. For example, it is unlikely that the actual temperature structure in SN 2011fe is as "noisy" as that shown in Figure C.3, because although the velocity gradient of the

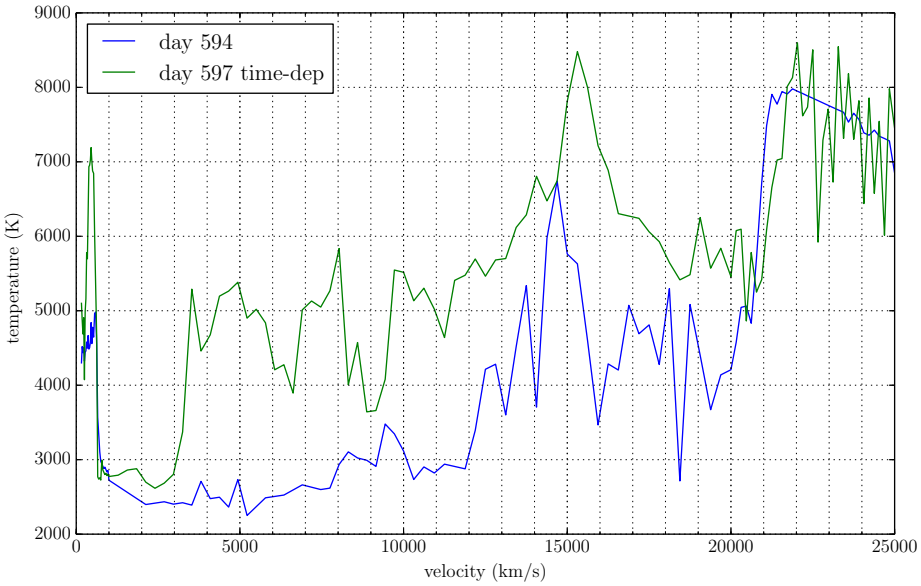

Figure C.3: Temperatures for time-independent day 594 vs. time-dependent day 597 calculation.

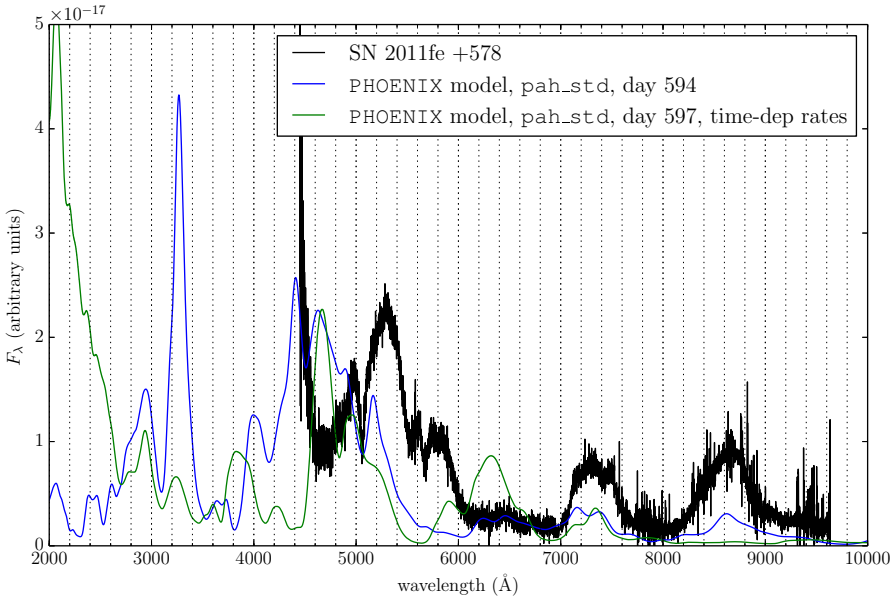

Figure C.4: Synthetic spectra at day 594 (time-independent) vs. day 597 (time-dependent rates) vs. SN 2011fe at day +578.

ejecta has flattened considerably since the ejecta has had so much time to expand. Furthermore, the optical depths throughout the ejecta will have decreased over time, causing the radiation field to equilibrate over long distances. Performing separate root-finds for the energy equation in every zone, as we did in the above calculations, neglects this implicit, long-distance coupling of the temperatures throughout the ejecta. Furthermore, the method characterizes the convergence based on the temperature changes in each zone falling below some prescribed value. Numerically, temperature changes can be a poor metric for measuring convergence, and one should instead measure the changes in the radiation moments (Mihalas 1978, § 7-2).

As a result, we have explored a variety of alternative temperature correction schemes, with varying degrees of success. Indeed, perturbative schemes which work in a wide variety of physical regimes are challenging to develop. This is in part because they assume that a hierarchy of coupling strengths among the various independent parameters can be discerned (Hauschildt and Baron 1999). However this is not always the case: in some physical regimes the coupling among all independent variables is significant, which is frequently the argument made for so-called *complete linearization* schemes, which solve all of the relevant equations of the stellar atmosphere problem simultaneously (Auer and Mihalas 1969; Mihalas 1978; Hillier 1990). On the other hand, linearization schemes ultimately reduce to multi-dimensional Newton-Raphson algorithms, which are unstable and have large memory footprints during computation. Perturbative scheme can avoid both of these problems and thus in principle can be applied to problems of arbitrary

complexity (Hauschildt and Baron 1999).

van Rossum (2012) emphasized the notion that in SNe Ia the amount of energy in the radiation field ($E_{\rm rad} \propto \rho T$) is orders of magnitude larger than the amount in the gas ($E_{\rm gas} \propto T^4$); as a result it is critical when enforcing radiative equilibrium to trace the radiation energy rather than the gas energy. The method he proposes is an Unsöld-Lucy method very similar to that described in (Hauschildt and Baron 1999). The only significant differences between the two methods are

1. van Rossum (2012) retains the $\mathcal{O}(v/c)$ terms in the radiation energy and momentum equations (which become negligible at late times), whereas Hauschildt and Baron (1999) ignore them.

2. When obtaining the "target" flux, van Rossum (2012) integrates the flux equation from the inside outward, imposing the nebular boundary condition $H(r = 0) = 0$. In contrast, Hauschildt and Baron (1999) integrate the flux from the outside inward, imposing as an outer boundary condition the observed flux of the SN.

At late times, the retention or neglect of $\mathcal{O}(v/c)$ terms will have no effect on the derived temperature structure since the optical depths at most wavelengths in the fastest moving parts of the ejecta is extremely small. In our calculations, we have found that the direction of integration of the flux equation, as well as the boundary conditions chosen for it, have a more profound influence on the resulting temperature structure. Because the flux equation is only a first-order differential equation, we are afforded only a single boundary condition, and thus are unable

to enforce both a prescribed emergent flux and the nebular boundary condition (even though both are desirable). However, it is possible to force $H(r \to 0) \to 0$ elsewhere besides the target flux equation: specifically, during the ALI step, `PHOENIX` already requires that, at the innermost layer of the model, each ray satisfies the condition

$$I_\lambda(\mu) = I_\lambda(-\mu) \tag{C.6}$$

such that $H \equiv \frac{1}{2}\int_{-1}^{1} d\mu I_\lambda \mu = 0$. It appears redundant, then, to specify $H(r = 0) = 0$ during the temperature correction step as van Rossum (2012) does, and that instead we should specify the outer boundary condition for $H(r = R)$ as Hauschildt and Baron (1999) do. However, we found in our calculations that doing so leads to a target flux profile $H(r)$ which increases monotonically with decreasing velocity, all the way to $r = 0$. This leads to unusually and likely non-physical temperature structures near the center of the ejecta, since the ALI step fights to drive $H(r = 0) = 0$ while the temperature correction step fights to make $H(r) = 0$ very large.

We implemented the method of van Rossum (2012) (neglecting his treatment of time-dependence), and attempted to calculate the temperature structure at day +594, when our synthetic spectrum poorly matches the observation. The result is shown in Figure C.5. The algorithm assigns almost no temperature change whatsoever at the inner zones, and instead only increases the temperature at the outermost zones after every iteration. The resulting synthetic spectrum is shown in Figure C.6. The high temperatures at the outer zones increases the opacity

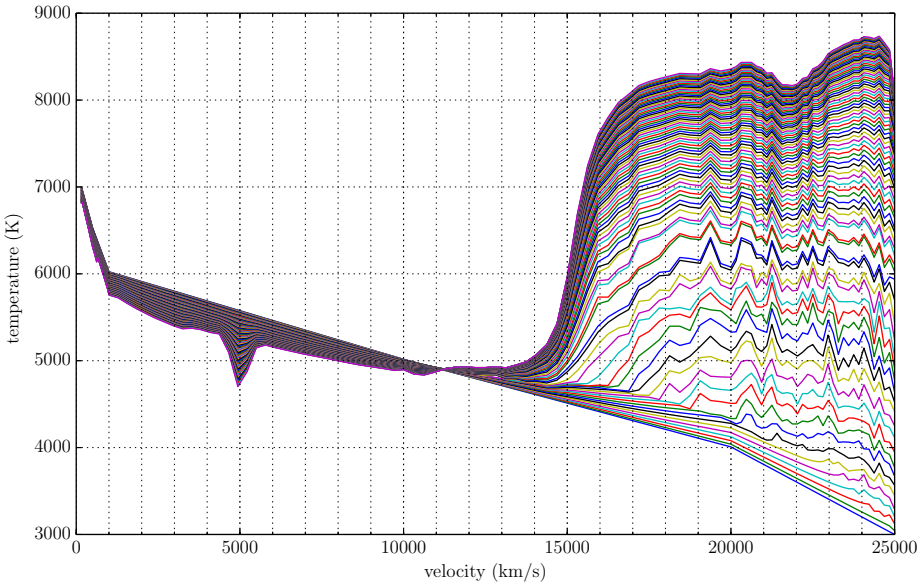

Figure C.5: Temperature evolution as a function of iteration using radiation energy balance scheme of van Rossum (ibid.), with the boundary condition $H(r = 0) = 0$. Each iteration increases the temperature in the outermost zones.

in the UV, leading to a large UV excess in the synthetic spectrum which is not observed.

We also modified this method to determine the target fluxes by integrating from the outside in, just as in Hauschildt and Baron (1999). This requires knowing the bolometric luminosity of the SN in the observer's frame, which is often poorly constrained at late times in SNe Ia. We thus assumed that the bolometric luminosity was roughly equal to the total energy deposition from radioactive ^{56}Ni and ^{56}Co, using the parameterized model of Stritzinger et al. (2006). An example calculation of the energy deposition as a function of time is shown in Figure C.7. The resulting evolution of the target and actual fluxes as a function of temperature iteration are shown in Figure C.8. This figure illustrates the "fight" between the

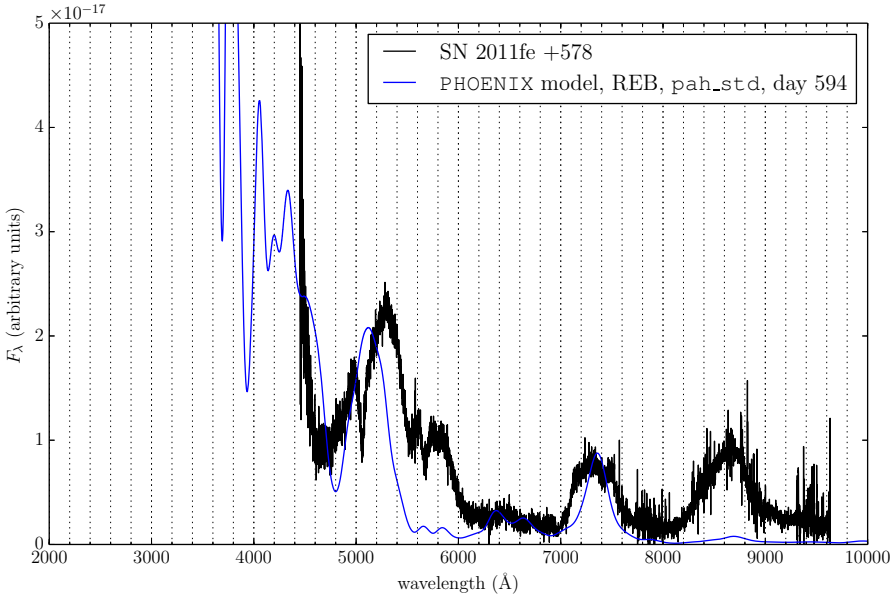

Figure C.6: Spectrum of `pah_std` at day 594 using radiation energy balance scheme vs. SN 2011fe at day +578.

ALI and the temperature correction steps for the value of H at the center of the ejecta, with the actual fluxes exhibiting a sudden downward turn as $v \to 0$.

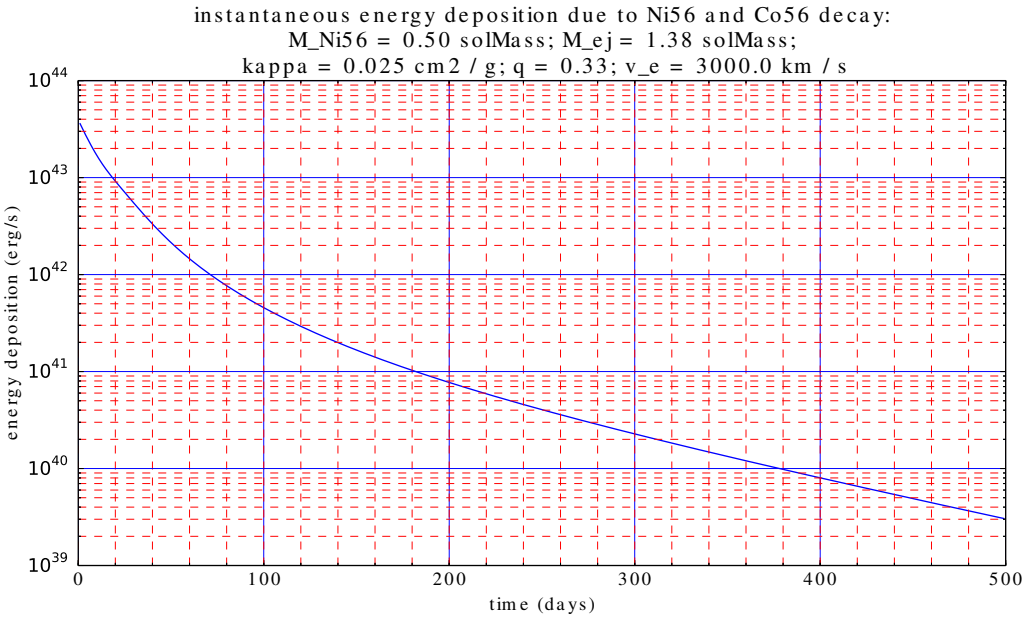

Figure C.7: Example energy deposition curve for a normal SN Ia, according to the model of Stritzinger et al. (ibid.).

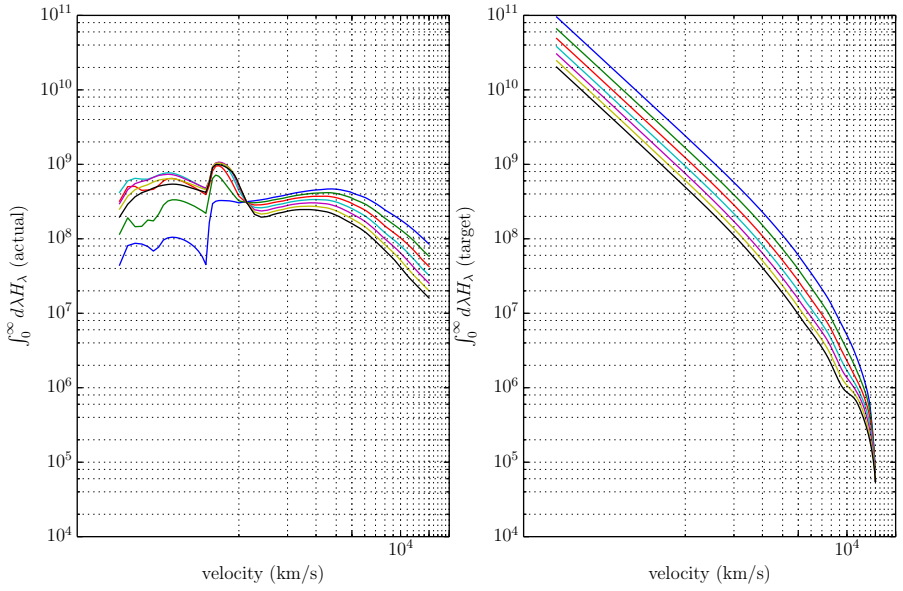

Figure C.8: Actual and target flux evolution using new REB/Unsöld-Lucy scheme.

Appendix D

Future applications of radiative transfer

Although numerical radiative transfer for astrophysical applications has been a mainstream craft for several decades (dating back at least to Mihalas 1965, 1970), there nevertheless remain many open questions and fertile opportunities to advance the field further still. In the following sections we outline a select few examples we have encountered during our work on this thesis. They are unrelated in their applications, but nevertheless trace their roots to same fundamental set of numerical tools.

D.1 Partial linearization/accelerated Λ-iteration for enforcing radiative equilibrium in 3-D late-time supernova simulations

In Chapter 3 and Chapter 4 we discussed the application of the Unsöld-Lucy temperature correction procedure to calculations of SNe Ia at post-maximum light epochs, in particular, that it gives spurious and unphysical results for ejecta temperature structures. We presented an alternative scheme which yields fairly good matches between synthetic spectra and observations core-normal SNe Ia at these epochs, but it too is not without some shortcomings, namely that it ignores

the implicit coupling among different parts of the ejecta by performing independent root-finds for the temperature in each zone. An ideal method would capture this implicit non-locality. All of these complicated interrelationships among variables at first glance render linearization methods quite appealing (e.g., Auer and Mihalas 1968, 1969; Auer 1973). After all, linearization provides an analytic coupling to many of these variables and thus avoids many of the problems described above. However, linearization has problems of its own, namely its (in)famous instability, as well as its huge memory requirements, which limit the resolution in wavelength, angle, and physical size of the problem being solved (Hauschildt and Baron 1999). Hauschildt (1992b) recognized the appeal of linearization methods for treating the global coupling of all zones in the model while trying to achieve radiative equilibrium, and introduced a partial linearization scheme which fits naturally within the accelerated Λ-iteration (ALI) framework of `PHOENIX`. This is a similar approach to that presented in Hubeny and Lanz (1995). It consists of first writing a "radiative equilibrium function" $F(T)$:

$$F(T) \equiv \begin{cases} \int_0^\infty d\lambda \kappa_\lambda (B_\lambda - J_\lambda) & \tau < \tau_s, \\ H^{(1)} - \int_0^\infty d\lambda H_\lambda & \tau \geq \tau_s, \end{cases} \tag{D.1}$$

where $\tau_s \sim 1$ is a parameter dividing the optically thick regions from the optically thin ones. In the nebular regimes of SNe Ia, most optical depths are small, so we

can write this as simply

$$F(T) = \int_0^\infty d\lambda \kappa_\lambda (B_\lambda - J_\lambda). \tag{D.2}$$

$F(T)$ is in fact a vector function $\vec{F}[T(\vec{r})]$, spanning the spatial grid. Therefore we can write the Jacobian matrix of this function as

$$A_{ij} \equiv \left.\frac{\partial F_i}{\partial T}\right|_{T_j} = \int_0^\infty d\lambda \kappa_\lambda \left[\left.\frac{\partial B_i}{\partial T}\right|_{T_j} \delta_{ij} - \left.\frac{\partial J_i}{\partial T}\right|_{T_j} \right] \tag{D.3}$$

Being the solution of an iterative procedure, J and its derivatives have no analytic functional form. However, its temperature derivative can be evaluated approximately by using the Λ operator, or rather a variation of it called the Ψ operator (Rybicki and Hummer 1991):

$$\Psi \equiv \Lambda \text{ diag} \left[\frac{1}{\chi} \right]. \tag{D.4}$$

By dividing the opacity out of the Λ operator, the Ψ operator acts on only the emissivities instead of on the complete source function:

$$J = \Lambda[S] = \Psi[\eta]. \tag{D.5}$$

If we neglect the temperature dependence of Ψ itself, we can write

$$\frac{\partial J}{\partial T} = \frac{\partial}{\partial T} \left[\Psi[\eta] \right] \simeq \Psi \left[\frac{\partial \eta}{\partial T} \right]. \tag{D.6}$$

The emissivity η has an analytic form:

$$\eta_\lambda(T) = \sum_k \frac{2hc^2}{\lambda^5} \left[\sum_{\ell<k} \frac{g_\ell}{g_k} \alpha_{k\ell}(\lambda) + \sum_{\ell>k} \alpha_{k\ell}(\lambda) \exp\left(-\frac{hc}{\lambda k_B T}\right) \frac{g_\ell}{g_k} \frac{2h^3 n_e}{(2\pi m)^{3/2}(k_B T)^{3/2}} \exp\left(-\frac{\chi_\ell - \chi_k}{k_B T}\right) \right] n_k + \sigma J_\lambda \quad \text{(D.7)}$$

or

$$\eta_\lambda(T) = \tilde{\eta}_\lambda(T) + \sigma J_\lambda \quad \text{(D.8)}$$

such that

$$J_\lambda = \Psi[\tilde{\eta}_\lambda + \sigma J_\lambda] \quad \text{(D.9)}$$

from which we can solve for J,

$$J_\lambda = (I - \Psi\sigma)^{-1}\Psi[\tilde{\eta_\lambda}] \quad \text{(D.10)}$$

and its derivative,

$$\frac{\partial J}{\partial T} \simeq (I - \Psi\sigma)^{-1}\Psi \left[\frac{\partial \tilde{\eta}_\lambda}{\partial T}\right]. \quad \text{(D.11)}$$

With this we now how an analytic form for the Jacobian matrix and can proceed with a Newton-Raphson-like algorithm (Hauschildt 1992b):

$$T_i^{(1)} = T_i^{(0)} - A_{ij}^{-1} F_j\left(T^{(0)}\right). \quad \text{(D.12)}$$

Although this method showed promise in the spherically symmetric calculations in Hauschildt (1992b), it was eventually abandoned in favor of the Unsöld-Lucy method in Hauschildt and Baron (1999). This was due in part to its unstable nature as a Newton-Raphson analogue, but also because in its original formulation the radiative equilibrium function $F(T)$ took two different forms depending on the value of τ relative to τ_s. At $\tau \sim 1$ the effects of both the constantly of the flux and the balancing of heating vs. cooling are of roughly equal importance, and imposing such an arbitrary and sudden transition in the functional form of $F(T)$ likely led to further instabilities, especially in the evaluation of the Jacobian matrix.

At late times in SNe Ia, however, this latter point may be less of a burden, as the ejecta at most (but not all) wavelengths is quite optically thin (cf. Chapter 4). Furthermore, this partial linearization method has the advantage of being agnostic to the geometry of the problem under consideration. Because it corrects the global temperature structure simultaneously, it in principle works in multiple dimension as well as the 1-D case considered in Hauschildt (1992b). Unsöld's method, in contrast, is quite stable, but relies on the scalar nature of the flux H in 1-D calculations. In 2- and 3-D calculations where $\vec{H}$ is a vector, the flux errors $\Delta\vec{H}$ are also vectors, and there no longer exists a meaningful connection between the flux errors and the scalar temperature corrections (van Rossum 2012).

There is certainly impetus to combine the recent implementation of 3-D NLTE radiative transfer in `PHOENIX` (Hauschildt and Baron 2006, 2014) with an algorithm to enforce radiative equilibrium. Fesen, Hoeflich, et al. (2014) recently presented

spatially resolved *HST* images of SN 1885 in M31 (also called S Andromedae) in which four plumes of Fe-rich material can be seen extending from the center of the SN remnant outward to roughly 10 000 $\mathrm{km\,s^{-1}}$. They argue that these may have been formed during the Rayleigh-Taylor instabilities which arise during the deflagration phase of a SN Ia explosion (e.g., Gamezo et al. 2003; Röpke, Hillebrandt, et al. 2006). If these plumes are common features of SNe Ia then their late-time spectra should be strongly influenced by this asymmetry. Three-dimensional radiative transfer calculations of SN Ia explosion models with a deflagration phase would provide strong constraints on the initial conditions of the WD explosion.

D.2 ALI in arbitrarily relativistic spacetimes

Relativistic radiative transfer is critical to simulating the explosions of core-collapse supernovae (CCSe). This is because the majority of the total energy in the explosion ($\sim 10^{53}$ erg) is contained in the neutrino field (Janka 2012). Obtaining successful explosions of CCSNe has been a challenge for many years, and it may be that the key (or at least one key) to achieving this is by capturing the complete interaction of neutrinos with the gas (Sumiyoshi et al. 2015). This may require a treatment of radiative transfer accounting fully for the effects of strong gravity via the Einstein field equations.

Although the application of radiative transfer to fully special relativistic systems is well understood (Mihalas, Kunasz, et al. 1975; Mihalas 1980; Hauschildt, Best, et al. 1991; Hauschildt and Wehrse 1991; Hauschildt 1992a), the extension

to general relativistic spacetimes is less well understood. Schinder (1988) and Schinder and Bludman (1989) adapted the "variable Eddington factor" (VEF) framework to "polar-sliced" spherically symmetric space times, for use in radiation hydrodynamics simulations of compact objects, e.g., core-collapse supernovae. However, as with all radiation moment-based formalisms, the VEF framework requires closure relations in order to relate higher-order moments to lower-order ones. Such relations generally arise from *a priori* knowledge of the behavior of the radiation field (its anisotropy, for example) in a particular geometry. In plane-parallel and spherically symmetric systems these are often possible to obtain, but in more complicated geometries they become much more complicated. As a result, so-called "variable Eddington tensors," the multi-dimensional generalization of VEFs, tend to take on cumbersome formulations, with only approximate or empirically motivated closure relations (e.g., Dykema et al. 1996; Hayes and Norman 2003; Cardall et al. 2013; Ramsey and Dullemond 2015).

ALI does not suffer from the closure relation problem because it accounts for the complete, angle-dependent behavior of the radiation by solving the transfer equation along a grid of rays spanning the complete phase space. One can apply the ALI framework to almost any radiating system as long as one can transform the transfer equation into the "standard form,"

$$\frac{dI}{d\tau} = -I + \hat{S} \tag{D.13}$$

where $\hat{S}$ is an "effective source function," generally a function of the true source

function $S \equiv \eta/\chi$ as well as other terms which describe the geometry or velocity field of the problem (e.g., Baron, Hauschildt, Chen, and Knop 2012, §2.2). Knop (2007) and Knop et al. (2007) applied the ALI framework to specific types of relativistic space times, but required analytic metrics and were restricted to a single spatial dimension.

Most multi-dimensional simulations of arbitrarily relativistic spacetimes use the so-called "3+1" decomposition of Einstein's field equations, in which the spacetime is foliated into a series of space-like hypersurfaces which with time-like normal vectors (Arnowitt et al. 2008; Baumgarte and Shapiro 2010). This approach allows one to write the field equations as a set of Cauchy initial value problems, in which case one generates a configuration of the spacetime which satisfies a set of constraint equations, and then evolves the space time according to another set of time-evolution equations, which by construction satisfy the constraint equations at any given time. This is exactly analogous to Maxwell's equations, in which one generates an electromagnetic field which satisfies Gauss's law and Gauss's law for magnetism, and then one evolves the field according to Faraday's and Ampère's laws, which guarantee the preservation of both of Gauss's laws at any time. Consequently one can use standard methods for solving time-dependent partial differential equations to evolve the field equations.

Methods for performing numerical ray-tracing calculations in highly symmetric relativistic spacetimes have existed for some time (e.g., Dexter and Agol 2009; Chen, Dai, and Baron 2013; Chen, Dai, Baron, and Kantowski 2013), and recently Vincent et al. (2012) extended the ray-tracing method to 3+1 numerical spactimes.

Ray-tracing itself does not account for scattering of particles into and out of individual null geodesics, which is an important process to account for if we wish to do radiative transfer calculations in, e.g., core-collapse supernovae or in neutron star atmospheres, where scattering opacities can be considerable. It may be possible, then, to adapt the formulation of Vincent et al. (2012) to ALI. After all, with this method one can calculate the path of a null geodesic with arbitrary initial conditions through a numerical space time, which in principle is exactly what one needs in order to cast the transfer equation into the standard form, Equation (D.13). Furthermore, much of the machinery needed to solve the differential equations for the geodesic paths in Vincent et al. (ibid.) is already present in many numerical relativity codes, such as the Einstein Toolkit (Löffler et al. 2012). This is because null geodesic tracing methods are often used to detect "apparent horizons" in numerical spacetimes, which must be avoided in order to preserve numerical stability during the simulation (Thornburg 2007). However, one must be mindful of curious complications when simulating relativistic systems, such as the notion that, in order to calculate quantities measured by a distant observer, one must calculate the geodesics *backward* in time, since one wishes to synchronize the arrival of information to the observer so that a measurement may be made at a single instant (Bohn et al. 2014).